In-medium effects in strangeness production in heavy-ion collisions at (sub)threshold energies

Taesoo Song [1,*] Laura Tolos [2,3,4,†] Joana Wirth [5,‡] Joerg Aichelin,[6,4,§] and Elena Bratkovskaya[1,7,‖]

[1]*GSI Helmholtzzentrum für Schwerionenforschung GmbH, Planckstrasse 1, 64291 Darmstadt, Germany*
[2]*Institute of Space Sciences (ICE, CSIC), Campus Universitat Autonoma de Barcelona, Carrer de Can Magrans, 08193 Bellaterra, Spain*
[3]*Institut d'Estudis Espacials de Catalunya (IEEC), 08034 Barcelona, Spain*
[4]*Frankfurt Institute for Advanced Studies, Ruth-Moufang-Strasse 1, 60438 Frankfurt am Main, Germany*
[5]*Excellence Cluster "Origin and Structure of the Universe" and Physik Department E62,*
Technische Universität München, 85748 Garching, Germany
[6]*SUBATECH UMR 6457 (IMT Atlantique, Université de Nantes, IN2P3/CNRS), 4 Rue Alfred Kastler, F-44307 Nantes, France*
[7]*Institute for Theoretical Physics, Johann Wolfgang Goethe Universität, Frankfurt am Main, Germany*

We study the in-medium effects in strangeness production in heavy-ion collisions at (sub)threshold energies of (1–2)A GeV based on the microscopic Parton-Hadron-String Dynamics (PHSD) transport approach. The in-medium modifications of the antikaon ($\bar{K} = K^-, \bar{K}^0$) properties are described via the self-consistent coupled-channel unitarized scheme based on a SU(3) chiral Lagrangian which incorporates explicitly the s and p waves of the kaon-nucleon interaction. This scheme provides the antikaon potential, spectral functions, and reaction cross sections as well as their dependence on baryon density, temperature, and antikaon momentum in the nuclear medium, which are incorporated in the off-shell dynamics of the PHSD. The in-medium modification of kaons ($K = K^+, K^0$) are accounted via the kaon-nuclear potential, which is assumed to be proportional to the local baryon density. The manifestation of the medium effects in observables is investigated for the K and $\bar{K}$ rapidity distributions, p_T spectra, the polar and azimuthal angular distributions, and directed (v_1) and elliptic (v_2) flows in C+C, Ni+Ni, and Au+Au collisions. We find—by comparison to experimental data from the KaoS, FOPI, and HADES Collaborations—that the modifications of (anti)kaon properties in nuclear matter are necessary to explain the data in a consistent manner. Moreover, we demonstrate the sensitivity of kaon observables to the equation of state of nuclear matter.

I. INTRODUCTION

The modification of hadron properties at finite temperatures and densities due to the onset of chiral symmetry restoration is an open problem in present strong interaction physics. This question is of primary importance for the field of heavy-ion collisions (HICs) and it has also implications for astrophysics, in particular for the evolution of the early universe and neutron stars. As suggested early by Kaplan and Nelson [1], the attractive kaon-nucleon interaction might lead to kaon condensation in the interior of neutron stars. Experimental data [2–9] and theoretical studies [10–25] on $K^{\pm}$ production from $A + A$ collisions at SIS (Schwerionensynchrotron, GSI) energies of (1–2)A GeV have shown that in-medium modifications of the properties of (anti)kaons have been seen in the collective flow pattern of K^+ mesons [26] as well as in the abundance and spectra of kaons and antikaons

---
*t.song@gsi.de
†tolos@ice.csic.es
‡joana.wirth@tum.de
§aichelin@subatech.in2p3.fr
‖e.bratkovskaya@gsi.de

[17,19,24,26]. Moreover, as advocated early in Ref. [10], the strangeness production at threshold energies is sensitive to the Equation of State (EoS) of nuclear matter and thus can provide comprehensive information about the compressibility of nuclear matter [22,24].

The theoretical study of in-medium properties of hadrons was launched in part by the early suggestion of Brown and Rho [27] that the modifications of hadron masses should scale with the scalar quark condensate $\langle \bar{q}q \rangle$ at finite baryon density and temperature. In this scenario the kaon masses "grow" with the density while antikaon masses "drop." The mass modification at normal nuclear matter density ρ_0 could be attributed to the (anti)kaon-nuclear potential. The first theoretical attempts on the extraction of the antikaon-nucleus potential from the analysis of kaonic-atom data were in favor of very strong attractive potentials of the order of -150 to -200 MeV at normal nuclear matter density ρ_0 [28–30]. However, later self-consistent calculations based on a chiral Lagrangian [31–37] or the coupled-channel unitarized scheme (or G-matrix approach) using meson-exchange potentials [38,39] predicted moderate attractive depths of -40 to -60 MeV at density ρ_0.

The complexity in the determination of the antikaon potential at finite baryon density is related to the fact that the antikaon-nucleon amplitude in the isospin channel $I = 0$ is

dominated by the $\Lambda(1405)$ resonant structure [40], which in free space is only $\simeq 27$ MeV below the $\bar{K}N$ threshold. In the vacuum the antikaon-nucleon interaction is repulsive at low energies; however, in the medium it becomes attractive. The onset of an attractive $\bar{K}N$ interaction at low densities is a consequence of an upshift of the $\Lambda(1405)$ resonance mass induced by Pauli blocking on the intermediate nucleon states [31–33,40]. Additional medium effects such as the self-energy of mesons in related coupled channels and the binding of hyperons in the nuclear environment bring a smoothed $\Lambda(1405)$ back to its vacuum position [36], while keeping the attractive character of the $\bar{K}N$ interaction in the medium. We refer the reader to Ref. [41] for a recent review on strangeness.

Another problem related to the complexity of the description of strangeness dynamics in relativistic heavy-ion reactions is that their in-medium complex self-energies and scattering amplitudes, partly far from the mass shell, have to be considered [19,39], because the antikaon couples strongly to the baryons and achieves a nontrivial spectral shape in the medium. The propagation of such broad states which change their properties dynamically depending on the local environment, i.e., a temperature T and a baryon density ρ_B (or baryon chemical potential μ_B), requires one to go beyond the standard on-shell Boltzmann-Uehling-Uhlenbeck (BUU) type of approaches and to employ a transport theory for strongly interacting systems. This became possible after significant progress in the understanding of the propagation of strongly interacting off-shell particles in phase-space configurations was obtained at the end of the last millennium: in Refs. [42,43] an off-shell transport approach was developed by Cassing and Juchem on the basis of the Kadanoff-Baym equations that include the propagation of particles with dynamical spectral functions (cf. also the review [44]). They derived relativistic off-shell generalized transport equations from the Wigner transformed Kadanoff-Baym equations in the limit of first-order gradients in phase space and realized them—within an extended test-particle representation—in the Hadron-String Dynamics (HSD) transport approach [18,45] extended later to the Parton-Hadron-String Dynamics (PHSD) approach [44,46–50]. The PHSD incorporates also partonic degrees of freedom in terms of strongly interacting dynamical quasiparticles, whose properties are evaluated within the Dynamical Quasi-Particle Model (DQPM) [51–53] in line with the lattice QCD EoS.

The formulation of off-shell transport found an immediate application for the description of the strangeness dynamics: whereas in the early calculations [13–18] the in-medium cross sections were simply extrapolated from on-shell cross sections in vacuum, in Ref. [19] the full off-shell dynamics—based on coupled channel G-matrix calculations [39]—was incorporated for the first time in the HSD transport approach for the description of strangeness production at SIS energies. It has been shown that the antikaon observables (multiplicities, rapidity and p_T spectra, angular distributions, flow harmonics v_1, v_2, etc.) are very sensitive to the in-medium interactions, i.e., to the details of the G-matrix approach. A summary of the research on strangeness dynamics at SIS energy can be found in the review [24].

The results obtained with the G-matrix approach in Ref. [19] are based on the Jülich meson-exchange model [38,39] as the effective $\bar{K}N$ interaction in matter. During the last decade the understanding of the $\bar{K}N$ interaction has been further improved: in Ref. [54] a chiral unitarity approach in coupled channels was developed by incorporating s and p waves of the kaon-nucleon interaction at finite density and zero temperature in a self-consistent manner. In Ref. [55] finite temperature effects were also implemented; however, a full self-consistent solution was achieved only for the s-wave effective $\bar{K}N$ interaction, while the p-wave contribution was treated by means of hyperon-nucleon insertions. Later on, the chiral effective scheme in dense (and hot) matter developed in Refs. [54,55] was substantially improved in Ref. [56]. There the full self-consistency in s and p waves at finite density and temperature was achieved. In this way, it became possible to generate in-medium antistrange meson-baryon cross sections (amplitudes) at finite density and temperature as well as to determine the single-particle properties of hyperons, such as the $\Lambda(1115)$, $\Sigma(1195)$, and $\Sigma^*(1385)$, at finite momentum with respect to the medium at rest, and finite density and temperature. The latter are important for calculations of the in-medium antikaon scattering cross sections.

While antikaons follow strongly attractive interactions in the medium, which broadens their spectral function substantially, the kaon spectral function stays narrow since there are no baryonic resonances that couple to kaons. Nevertheless, they are affected by the repulsive interaction with nucleons, which can be approximated by the kaon-nuclear potential proportional to the local baryon density. This scenario has been widely explored in different transport approaches [11–23] (although there are models which includes the (anti)kaon on-shell production via the coupling to heavy baryonic resonances with vacuum properties [57,58]). It has been found that the kaon repulsive potential of $+20$ to 30 MeV at normal nuclear density ρ_0 is mostly consistent with a variety of experimental data on $p + A$, $\pi + A$, and $A + A$ collisions. We refer the reader to the review [24] and references therein.

The goal of this work is to study the in-medium effects in the strangeness production in heavy-ion collisions at (sub)threshold energies employing the microscopic transport approach PHSD which incorporates the in-medium description of the antikaon-nucleon interactions based on "state of the art" many-body theory realized by the G-matrix formalism [56]. This chiral unitary approach in coupled channels incorporates the s and p waves of the kaon-nucleon interaction, its modification in the hot and dense medium to account for Pauli blocking effects, mean-field binding for baryons, as well as pion and kaon self-energies. Moreover, it implements unitarization and self-consistency for both the s- and p-wave interactions at finite temperature and density. This provides access to in-medium amplitudes in several elastic and inelastic coupled channels with strangeness content $S = -1$. For the in-medium scenario of the kaon-nucleon interaction we will adopt here a repulsive potential linear in the baryon density. As another novel development, we mention also the implementation of detailed balance on the level of $2 \leftrightarrow 3$ reactions for the main channels for strangeness production/absorption by baryons ($B = N, \Delta$) and pions: $B + B \leftrightarrow N + Y + K$ and

$B + \pi \leftrightarrow N + N + \bar{K}$, as well as for the non-resonant reactions $N + N \leftrightarrow N + N + \pi$ and $\pi + N \leftrightarrow N + \pi + \pi$. We will confront our theoretical results with available experimental data on (anti)kaon production at SIS energies and analyze the consequences of chiral symmetry restoration in strangeness observables.

The outline of the paper is as follows: In Sec. II we shall briefly recall the basic concepts of the chiral SU(3) model and G-matrix method used in the present investigation and describe the medium modifications of the $K(\bar{K})$ mesons in this effective many-body model. In Sec. III we recall the basic ideas of the PHSD approach. Sections IV and V are, respectively, dedicated to the production and absorption of K and $\bar{K}$ mesons and their modifications in the nuclear medium. In Sec. VI we investigate the properties of $K(\bar{K})$ mesons in heavy-ion collisions, and the results are compared to experimental data from different collaborations in Sec. VII. Section VIII summarizes the findings of the present investigation and discusses future extensions.

II. CHIRAL UNITARIZED MODEL FOR $\bar{K}N$ IN HOT NUCLEAR MATTER

Here we summarize the main features of the self-consistent unitarized coupled-channel model in dense and hot matter (or G-matrix approach) based on the SU(3) meson-baryon chiral Lagrangian, which incorporates the s and p waves of the antikaon-nucleon interaction, as developed in Ref. [56].

The lowest-order chiral Lagrangian which couples the octet of light pseudoscalar mesons to the octet of $1/2^+$ baryons is given by

$$L = \langle \bar{B}i\gamma^{\mu}\nabla_{\mu}B \rangle - M\langle \bar{B}B \rangle + \tfrac{1}{2}D\langle \bar{B}\gamma^{\mu}\gamma_5\{u_{\mu}, B\} \rangle + \tfrac{1}{2}F\langle \bar{B}\gamma^{\mu}\gamma_5[u_{\mu}, B] \rangle, \quad (1)$$

where $\langle \cdots \rangle$ denotes the trace over SU(3) flavor matrices, M is the baryon mass, D and F stand for the vector and axial-vector coupling constants, and ∇_{μ} is the covariant derivative that couples the baryon fields to the pseudoscalar meson axial vector current Γ_{μ},

$$\begin{aligned} \nabla_{\mu}B &= \partial_{\mu}B + [\Gamma_{\mu}, B], \\ \Gamma_{\mu} &= \tfrac{1}{2}(u^{\dagger}\partial_{\mu}u + u\,\partial_{\mu}u^{\dagger}), \\ U &= u^2 = \exp(i\sqrt{2}\Phi/f), \\ u_{\mu} &= iu^{\dagger}\partial_{\mu}Uu^{\dagger}, \end{aligned} \quad (2)$$

with f the meson weak decay constant, and Φ and B the standard SU(3) meson and baryon field matrices.

The s-wave meson-baryon interaction results from the covariant derivative term in Eq. (1). Keeping terms up to two meson fields, one gets

$$L \sim \frac{i}{4f^2}\langle \bar{B}\gamma^{\mu}[\Phi\partial_{\mu}\Phi - \partial_{\mu}\Phi\Phi, B]\rangle. \quad (3)$$

from which one derives the meson-baryon (tree-level) s amplitudes

$$V_{ij}^s = -C_{ij}\frac{1}{4f^2}\bar{u}(p')\gamma^{\mu}u(p)(k_{\mu} + k'_{\mu}), \quad (4)$$

where k, k' (p, p') are the initial and final meson (baryon) momenta, respectively, and the coefficients C_{ij}, with i, j indicating the particular meson-baryon channel, can be found explicitly in Ref. [59]. For low-energy scattering, the s-wave meson-baryon interaction can be written as

$$\begin{aligned} V_{ij}^s &= -C_{ij}\frac{1}{4f^2}\left(2\sqrt{s} - M_{B_i} - M_{B_j}\right) \\ &\quad \times \left(\frac{M_{B_i} + E_i}{2M_{B_i}}\right)^{1/2}\left(\frac{M_{B_j} + E_j}{2M_{B_j}}\right)^{1/2} \\ &\simeq -C_{ij}\frac{1}{4f^2}(k_i^0 + k_j^0), \end{aligned} \quad (5)$$

where $\sqrt{s}$ is the center-of-mass (c.m.) energy, $M_{B_{i(j)}}$ and $E_{i(j)}$ are the mass and energy of the baryon in the $i(j)$ channel, respectively. The second equation is satisfied to a good approximation for practical purposes. In this study, we consider the channels which couple to K^-p,

$$\begin{aligned} &K^-p, \ \bar{K}^0n, \ \pi^0\Lambda, \ \pi^0\Sigma^0, \ \eta\Lambda, \ \eta\Sigma^0, \\ &\pi^+\Sigma^-, \ \pi^-\Sigma^+, \ K^+\Xi^-, \ K^0\Xi^0, \end{aligned} \quad (6)$$

and the channels which couple to K^-n,

$$K^-n, \ \pi^0\Sigma^-, \ \pi^-\Sigma^0, \ \pi^-\Lambda, \ \eta\Sigma^-, \ K^0\Xi^-. \quad (7)$$

The main contribution to the p-wave meson-baryon interactions comes from the Λ and Σ pole terms, which result from the D and F terms of the lowest-order meson-baryon chiral Lagrangian of Eq. (1). The $\Sigma^*(1385)$ is also taken into account explicitly, as done in Ref. [60]. Moreover, the Lagrangian in Eq. (3) also provides a small part of the p wave.

Following Refs. [54,56], the p-wave meson-baryon interaction is given by

$$\tilde{V}_{ij}^p = 3[f_{ij}(\sqrt{s})\hat{q}' \cdot \hat{q} - ig_{ij}(\sqrt{s})(\hat{q}' \times \hat{q}) \cdot \vec{\sigma}], \quad (8)$$

where $\vec{q}(\vec{q}')$ are the on-shell c.m. three-momentum of incoming (outgoing) mesons, and $f_{ij}(\sqrt{s})$ and $g_{ij}(\sqrt{s})$ correspond to the spin-non-flip and spin-flip amplitudes, respectively, that read

$$\begin{aligned} f_{ij}(\sqrt{s}) &= \frac{1}{3}\left\{-C_{ij}\frac{1}{4f^2}a_ia_j\left(\frac{1}{b_i} + \frac{1}{b_j}\right)\right. \\ &\quad + \frac{D_i^{\Lambda}D_j^{\Lambda}\left(1 + \frac{q_i^0}{M_i}\right)\left(1 + \frac{q_j^0}{M_j}\right)}{\sqrt{s} - \tilde{M}_{\Lambda}} \\ &\quad + \frac{D_i^{\Sigma}D_j^{\Sigma}\left(1 + \frac{q_i^0}{M_i}\right)\left(1 + \frac{q_j^0}{M_j}\right)}{\sqrt{s} - \tilde{M}_{\Sigma}} \\ &\quad \left. + \frac{2}{3}\frac{D_i^{\Sigma^*}D_j^{\Sigma^*}}{\sqrt{s} - \tilde{M}_{\Sigma^*}}\right\}q_iq_j, \end{aligned} \quad (9)$$

$$\begin{aligned} g_{ij}(\sqrt{s}) &= \frac{1}{3}\left\{C_{ij}\frac{1}{4f^2}a_ia_j\left(\frac{1}{b_i} + \frac{1}{b_j}\right)\right. \\ &\quad - \frac{D_i^{\Lambda}D_j^{\Lambda}\left(1 + \frac{q_i^0}{M_i}\right)\left(1 + \frac{q_j^0}{M_j}\right)}{\sqrt{s} - \tilde{M}_{\Lambda}} \end{aligned}$$

$$-\frac{D_i^\Sigma D_j^\Sigma\left(1+\frac{q_i^0}{M_i}\right)\left(1+\frac{q_j^0}{M_j}\right)}{\sqrt{s}-\tilde{M}_\Sigma}$$

$$+\frac{1}{3}\frac{D_i^{\Sigma^*}D_j^{\Sigma^*}}{\sqrt{s}-\tilde{M}_\Sigma^*}\Bigg\}q_iq_j, \tag{10}$$

where $q_{i(j)}\equiv|\vec{q}_{i(j)}|$. The first term in both f_{ij} and g_{ij} comes from the small p-wave component in the meson-baryon amplitudes from the lowest order chiral Lagrangian in Eq. (1) [54,56], with

$$a_i=\sqrt{\frac{E_i+M_i}{2M_i}}, \quad b_i=E_i+M_i, \quad E_i=\sqrt{M_i^2+\vec{q}_i^{\,2}}, \tag{11}$$

given in the c.m. frame. Moreover, D_i^Y are the couplings of Λ, Σ. and Σ^* to a given meson-baryon pair:

$$D_i^\Lambda=c_i^{D,\Lambda}\sqrt{\frac{20}{3}}\frac{D}{2f}-c_i^{F,\Lambda}\sqrt{12}\frac{F}{2f},$$

$$D_i^\Sigma=c_i^{D,\Sigma}\sqrt{\frac{20}{3}}\frac{D}{2f}-c_i^{F,\Sigma}\sqrt{12}\frac{F}{2f},$$

$$D_i^{\Sigma^*}=c_i^{S,\Sigma^*}\frac{12}{5}\frac{D+F}{2f}. \tag{12}$$

The constants c^D, c^F, c^S are the SU(3) Clebsch-Gordan coefficients (see Table I of Ref. [61]), whereas the couplings D and F are chosen as $D=0.85$ and $F=0.52$. The masses $\tilde{M}_\Lambda$, $\tilde{M}_\Sigma$, $\tilde{M}_{\Sigma^*}$ are bare masses of the hyperons ($\tilde{M}_\Lambda=1030$ MeV, $\tilde{M}_\Sigma=1120$ MeV, $\tilde{M}_{\Sigma^*}=1371$ MeV), which will turn into physical masses upon the unitarization procedure described below.

Due to its spin structure, the p-wave contribution mixes different total angular momenta ($J=1/2,3/2$). For unitarization, it is convenient to rewrite the p-wave amplitudes according to the total angular momentum J, since these amplitudes can be unitarized independently. Thus, one can then define the p-wave tree-level amplitudes according to the total angular momentum, V_{ij-}^p ($L=1$, $J=1/2$) and V_{ij+}^p ($L=1$, $J=3/2$), as

$$V_{ij-}^p=f_{ij}-2g_{ij},$$

$$V_{ij+}^p=f_{ij}+g_{ij}. \tag{13}$$

Note that the Σ^* pole is contained in the V_+^p amplitude, whereas the V_-^p amplitude includes the Λ and Σ poles.

The transition amplitudes can be obtained by means of a unitarization coupled-channel procedure based on solving the Bethe-Salpeter equation by using the tree-level contributions to the s- and p-wave meson-baryon scattering as the kernel of the equation. Within the on-shell factorization [59,62], the Bethe-Salpeter equation is given in matrix notation as

$$T=V+VGT,$$

$$T=[1-VG]^{-1}V, \tag{14}$$

where V is the kernel (potential) and G is a diagonal matrix accounting for the loop function of a meson-baryon G_l prop-

agator,

$$G_l(\sqrt{s})=i\int\frac{d^4q}{(2\pi)^4}\frac{M_l}{E_l(\vec{P}-\vec{q})}\frac{1}{\sqrt{s}-q_0-E_l(\vec{P}-\vec{q})+i\varepsilon}$$

$$\times\frac{1}{q_0^2-\vec{q}^{\,2}-m_l^2+i\varepsilon}, \tag{15}$$

with $(P_0,\vec{P})$ being the total four-momentum of the meson-baryon pair and $s=P_0^2-\vec{P}^2$. The loop is divergent and needs to be regularized. This can be done by adopting either a cutoff method or dimensional regularization. We will adopt the cutoff method as it is easier and more transparent when dealing with particles in the medium. Within this method, and taking advantage of Lorentz invariance to calculate in the c.m. frame, the loop function reads

$$G_l(\sqrt{s})=\int_{|\vec{q}|<q_{\max}}\frac{d^3q}{(2\pi)^3}\frac{1}{2\omega_l(\vec{q})}\frac{M_l}{E_l(-\vec{q})}$$

$$\times\frac{1}{\sqrt{s}-\omega_l(\vec{q})-E_l(-\vec{q})+i\varepsilon}, \tag{16}$$

with ω_l (E_l) being the energy of the meson (baryon) in the intermediate state in the c.m. frame, and $q_{\max}=630$ MeV, which has been fixed in this scheme to reproduce the $\Lambda(1405)$ properties and several threshold branching ratios [59].

Whereas the s-wave amplitude of Eq. (5) can be used directly to solve Eq. (14) to obtain the transition amplitude in the s wave (T^s), for the p wave one proceeds as

$$T_+^p=[1-V_+^pG]^{-1}V_+^p,$$

$$T_-^p=[1-V_-^pG]^{-1}V_-^p. \tag{17}$$

Nuclear matter effects at finite temperature are introduced through the modification of the meson-baryon propagators, as described in Refs. [55,56]. On the one hand, one of the main sources of medium modifications comes from the Pauli principle. On the other hand, all mesons and baryons in the intermediate loops interact with the nucleons of the Fermi sea, and their properties are modified with respect to those in vacuum. All these changes are straightforwardly implemented within the imaginary time formalism, as shown in Refs. [55,56]. Here we summarize the most important findings.

As found in Ref. [56], the in-medium loop function of $\bar{K}N$ states reads

$$G_{\bar{K}N}(P_0,\vec{P};T)$$

$$=\int\frac{d^3q}{(2\pi)^3}\frac{M_N}{E_N(\vec{P}-\vec{q},T)}$$

$$\times\left[\int_0^\infty d\omega S_{\bar{K}}(\omega,\vec{q};T)\frac{1-n_N(\vec{P}-\vec{q},T)}{P_0+i\varepsilon-\omega-E_N(\vec{P}-\vec{q},T)}\right.$$

$$\left.+\int_0^\infty d\omega S_K(\omega,\vec{q};T)\frac{n_N(\vec{P}-\vec{q},T)}{P_0+i\varepsilon+\omega-E_N(\vec{P}-\vec{q},T)}\right]. \tag{18}$$

The Pauli blocking of nucleons is given by the $1-n_N(\vec{P}-\vec{q},T)$ term, where $n_N(\vec{P}-\vec{q},T)=[1+\exp(E_N(\vec{p},T)-$

$\mu_B)/T)]^{-1}$ is the nucleon Fermi-Dirac distribution. The medium modification on kaons and antikaons appears through the corresponding spectral functions, defined as

$$S_M(\omega, \vec{q}; T) = -\frac{1}{\pi} \frac{\text{Im} \, \Sigma_M(\omega, \vec{q}; T)}{|\, \omega^2 - \vec{q}^2 - m_M^2 - \Sigma_M(\omega, \vec{q}; T) \,|^2}, \quad (19)$$

where Σ_M is the meson self-energy that will be described in more detail below for the $\bar{K}$ case. The K spectral function, S_K, can be replaced by a free-space delta function, as the interaction of kaons with matter is rather weak [55]. Note also that the second term in the $\bar{K}N$ loop function typically provides a small, real contribution for the studied energy range in P_0.

In the case of $\pi Y (= \Lambda, \Sigma)$ one finds

$$G_{\pi Y}(P_0, \vec{P}; T)$$
$$= \int \frac{d^3 q}{(2\pi)^3} \frac{M_Y}{E_Y(\vec{P} - \vec{q}, T)}$$
$$\times \int_0^\infty d\omega S_\pi(\omega, \vec{q}, T) \left[\frac{1 + f(\omega, T)}{P_0 + i\varepsilon - \omega - E_Y(\vec{P} - \vec{q}, T)} \right.$$
$$\left. + \frac{f(\omega, T)}{P_0 + i\varepsilon + \omega - E_Y(\vec{P} - \vec{q}, T)} \right], \quad (20)$$

where the πY loop function incorporates the pion spectral function S_π. The first term is the dominant one for the studied energy range in P_0 and carries the $1 + f(\omega, T)$ enhancement factor, which accounts for the contribution from thermal pions at finite temperature. For hyperons, we neglect the fermion distribution given the low population for the studied densities and temperatures.

As for $r = \eta \Lambda, \eta \Sigma$, and $K \Xi$ intermediate states, we simply consider the meson propagator in vacuum and include only the effective baryon energies modified by the mean-field binding potential for Λ and Σ hyperons [56], i.e.,

$$G_r(P_0, \vec{P}; T) = \int \frac{d^3 q}{(2\pi)^3} \frac{1}{2\omega_r(\vec{q})} \frac{M_r}{E_r(\vec{P} - \vec{q}, T)}$$
$$\times \frac{1}{P_0 + i\varepsilon - \omega_r(\vec{q}) - E_r(\vec{P} - \vec{q}, T)}. \quad (21)$$

The in-medium s- and p-wave transition amplitudes for $\bar{K}N$ at finite density and temperature are obtained solving Eq. (14) in matter. The on-shell factorization of the amplitudes in the Bethe-Salpeter equation can be maintained in the case of the in-medium calculation for s-wave scattering [54]. The solution of the Bethe-Salpeter equation with on-shell amplitudes can be kept for the p waves with a simple modification of the meson-baryon loop function, as shown in Ref. [54]. If we denote by $G_l^L(P_0, \vec{P}; T)$ the in-medium meson-baryon propagator for s wave ($L = 0$) and p wave ($L = 1$), one has

$$G_l^s(P_0, \vec{P}; T) = G_l(P_0, \vec{P}; T),$$
$$G_l^p(P_0, \vec{P}; T) = G_l(s) + \frac{1}{\vec{q}_{\text{on}}^2}[\tilde{G}_l(P_0, \vec{P}; T) - \tilde{G}_l(s)], \quad (22)$$

where the $\tilde{G}$ functions carry an extra $\vec{q}^2$ factor in the integrand, corresponding to the off-shell p-wave vertex. Moreover, nu-
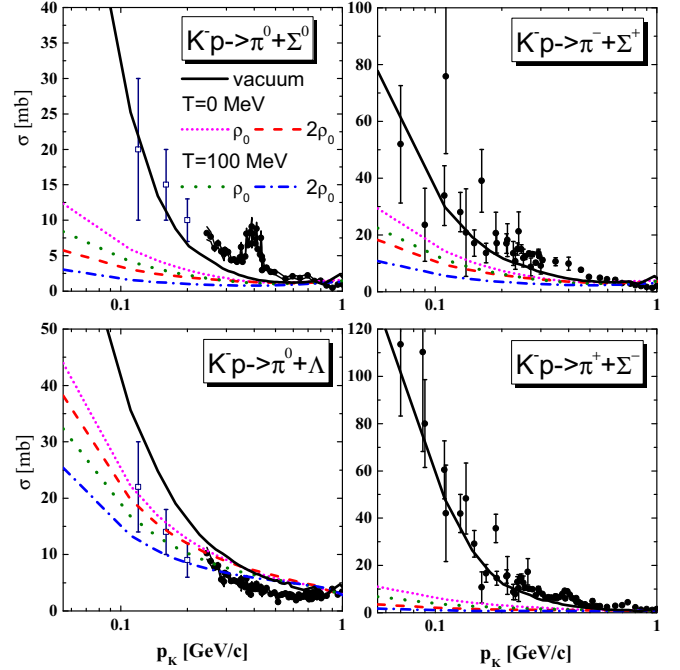

FIG. 1. The $K^- p$ cross sections to the final states $\pi^0 \Sigma^0$, $\pi^- \Sigma^+$, $\pi^+ \Sigma^-$, and $\pi^0 \Lambda$ according to the G-matrix calculations at $\rho = \rho_0$, $2\rho_0$ and $T = 0$, 100 MeV in comparison with the experimental data [63].

clear short-range correlations have to be taken into account, and the p-wave amplitudes need to be corrected to incorporate, in the external states, the proper off-shell momentum [54].

Once the transition amplitudes in free space and in matter are evaluated, the corresponding cross sections can be obtained by

$$\frac{d\sigma_{ij}}{d\Omega}(\sqrt{s}) = \frac{1}{16\pi^2} \frac{M_i M_j}{s} \frac{q_j}{q_i}$$
$$\times \left\{ \left| T_{ij}^s + (2T_{ij+}^p + T_{ij-}^p) \cos\theta \right|^2 \right.$$
$$\left. + \left| T_{ij+}^p - T_{ij-}^p \right|^2 \sin^2\theta \right\}, \quad (23)$$

where $q_i(q_j)$ is the modulus of the on-shell c.m. three-momentum of the incoming (outgoing) meson-baryon pair, and θ is the scattering angle in that frame.

Figure 1 shows the $K^- p$ cross sections to the final states $\pi^0 \Sigma^0$, $\pi^- \Sigma^+$, $\pi^+ \Sigma^-$, and $\pi^0 \Lambda$ at $T = 0$ and $T = 100$ MeV for several baryon densities. The total three-momentum of $K^- p$ is taken to be zero, while k_{K^-} is calculated in the proton rest frame. One can see that the cross section in each channel is close to the experimental data at low densities, while it decreases with increasing baryon density and temperature. As density and temperature increase, the rapid fall of the cross section close to threshold is softened and the strength is distributed over a wide range of energies, as the $\Lambda(1405)$ melts in matter.

Once the transition amplitudes are computed, the self-energy of the antikaon in either s or p wave is obtained by integrating over the nucleon Fermi distribution at a given
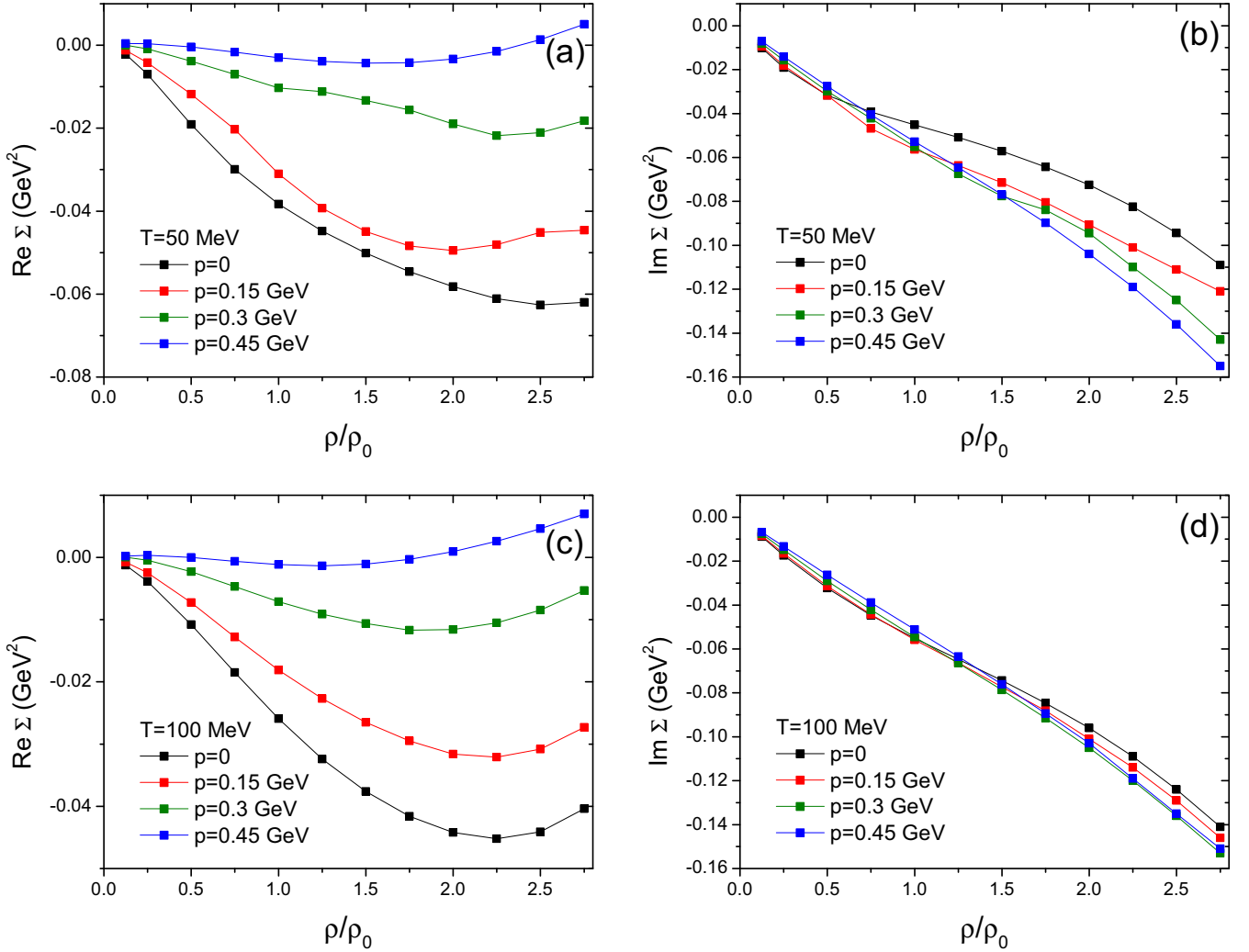
FIG. 2. The real part (left) and the imaginary part (right) of antikaon self-energy as a function of the baryon density for antikaon momenta of 0, 150, 300, and 450 MeV in the rest frame of nuclear matter at $T = 50$ MeV (upper) and 100 MeV (lower).

temperature,

$$\Sigma_{\bar{K}}^L(k_0, \vec{k}; T) = 4 \int \frac{d^3p}{(2\pi)^3} n_N(\vec{p}, T) \bar{T}_{\bar{K}N \to \bar{K}N}^L(P_0, \vec{P}; T), \quad (24)$$

where $P_0 = k_0 + E_N(\vec{p}, T)$ and $\vec{P} = \vec{k} + \vec{p}$ are the total energy and momentum of the $\bar{K}N$ pair in the nuclear medium rest frame, k stands for the momentum of the $\bar{K}$ meson also in this frame, and $\bar{T}^L$ indicates the spin and isospin averaged scattering amplitude for a given partial wave ($L = 0$ or $L = 1$). For example, for K^- we have

$$\Sigma_{K^-}^L(k_0, \vec{k}; T) = 2 \int \frac{d^3p}{(2\pi)^3} \left[n_p(\vec{p}, T) \bar{T}_{K^-p \to K^-p}^L(P_0, \vec{P}; T) \right.$$
$$\left. + n_n(\vec{p}, T) \bar{T}_{K^-n \to K^-n}^L(P_0, \vec{P}; T) \right], \quad (25)$$

where the $L = 1$ transition amplitude reads $T^p = 3 [T_-^p + 2T_+^p]$, with T_-^p and T_+^p given in Eqs. (17). The calculation of the antikaon self-energy is a self-consistent process, since the self-energy is obtained from the in-medium tran-

sition amplitude, $T_{\bar{K}N \to \bar{K}N}$, which requires the evaluation of the $\bar{K}N$ loop function, $G_{\bar{K}N}$, and the latter itself is a function of $\Sigma_{\bar{K}}(k_0, \vec{k}; T)$ through the antikaon spectral function $S_{\bar{K}}(k_0, \vec{k}; T)$,

$$S_{\bar{K}}(k_0, \vec{k}; T) = -\frac{1}{\pi} \frac{\text{Im} \Sigma_{\bar{K}}(k_0, \vec{k}; T)}{\left| k_0^2 - \vec{k}^2 - m_{\bar{K}}^2 - \Sigma_{\bar{K}}(k_0, \vec{k}; T) \right|^2}. \quad (26)$$

Figure 2 shows the real and imaginary parts of antikaon self-energy as a function of the baryon density for a couple of antikaon momenta in the rest frame of nuclear matter at $T = 50$ and 100 MeV. As the baryon density increases, the imaginary part of the self-energy decreases continuously due to the increase of phase space, whereas the real part decreases up to twice saturation density for momenta up to 0.3 GeV. With increasing antikaon momentum, the changes in the real part of the self-energy become smaller, while the imaginary part is much less sensitive to the momentum.
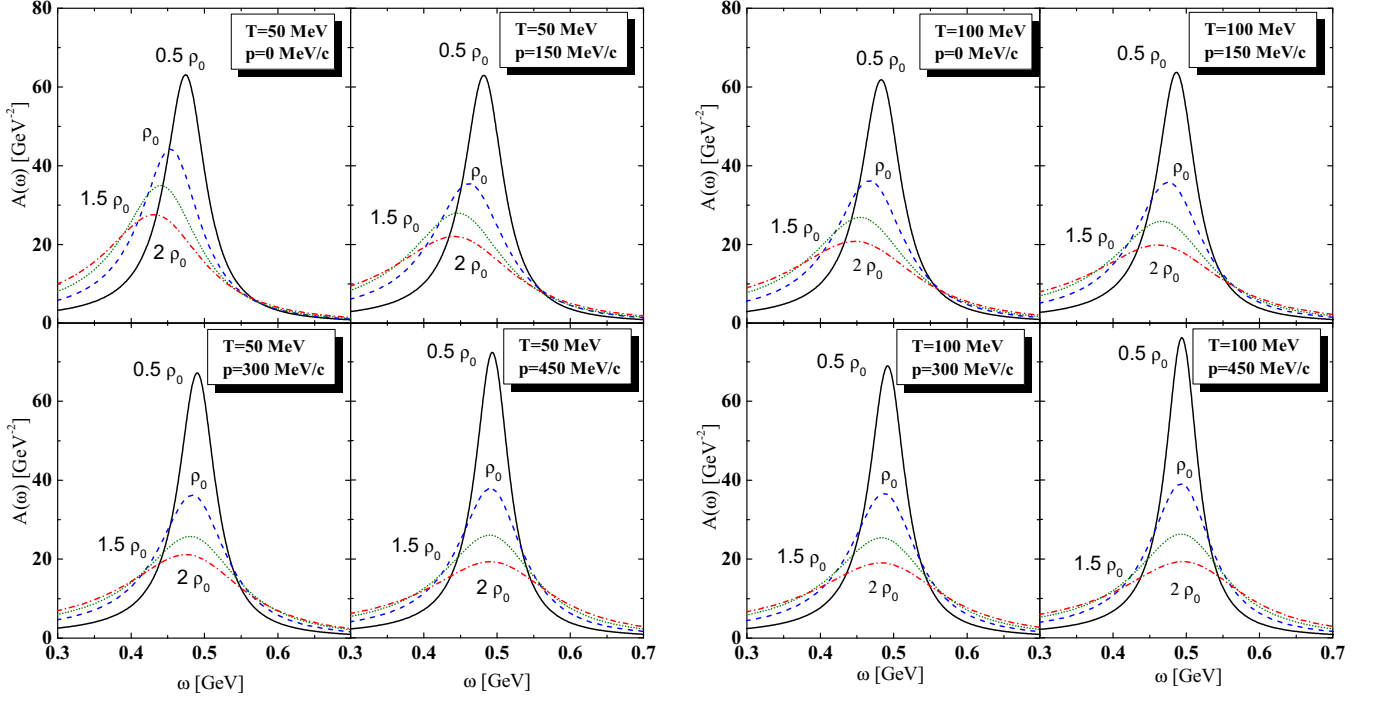
FIG. 3. Spectral function of $\bar{K}$ as a function of invariant mass at $\rho = 0.5\rho_0$, ρ_0, $1.5\rho_0$, and $2\rho_0$ with ρ_0 being saturation density for antikaon momentum $p = 0$, 150, 300, and 450 MeV in the rest frame of nuclear matter at $T = 50$ MeV (left) and 100 MeV (right).

The spectral function can be then reconstructed as

$$A_{\bar{K}}(\omega, \mathbf{k}) = \frac{-2 \operatorname{Im} \Sigma_{\bar{K}}}{\left(\omega^2 - \mathbf{k}^2 - m_{\bar{K}}^2 - \operatorname{Re} \Sigma_{\bar{K}}\right)^2 + (\operatorname{Im} \Sigma_{\bar{K}})^2}, \quad (27)$$

where $m_{\bar{K}}$ is the antikaon mass in vacuum and the spectral function is normalized as

$$\int_0^\infty \frac{d\omega}{2\pi} \omega A_{\bar{K}}(\omega, \mathbf{k}) = \frac{1}{2}. \quad (28)$$

From now on we denote $A_{\bar{K}}$ as the spectral function, as shown in the literature [19], which is related to $S_{\bar{K}}$ in Eq. (26) by $S_{\bar{K}} = A_{\bar{K}}/(2\pi)$.

One can change the integral variable from the energy ω to the invariant mass of the $\bar{K}$,

$$A_{\bar{K}}(m^2) = \frac{-2 \operatorname{Im} \Sigma_{\bar{K}}}{\left(m^2 - m_{\bar{K}}^2 - \operatorname{Re} \Sigma_{\bar{K}}\right)^2 + (\operatorname{Im} \Sigma_{\bar{K}})^2}, \quad (29)$$

where $m^2 = \omega^2 - k_{\bar{K}}^2$ and

$$\int_0^\infty \frac{dm^2}{2\pi} A_{\bar{K}}(m^2) = 1. \quad (30)$$

Figure 3 shows the spectral function of the $\bar{K}$ as a function of invariant mass at four baryon densities for antikaon momenta $p = 0$, 150, 300, and 450 MeV in the rest frame of nuclear matter at $T = 50$ MeV (left panels) and $T = 100$ MeV (right panels). The quasiparticle peak appears at $m^2 - m_{\bar{K}}^2 - \operatorname{Re} \Sigma_{\bar{K}} = 0$, its height being proportional to $-1/\operatorname{Im} \Sigma_{\bar{K}}$.

III. BASIC CONCEPTS OF THE PHSD

We start with a reminder of the basic ideas of the PHSD transport approach. The parton-hadron-string dynamics transport approach [44,46–49] is a microscopic off-shell transport approach for the description of strongly interacting hadronic and partonic matter in and out of equilibrium. It is based on the solution of Kadanoff-Baym equations in first-order gradient expansion in phase space [44]. The approach consistently describes the full evolution of a relativistic heavy-ion collision from the initial hard scatterings and string formation through the dynamical deconfinement phase transition to the strongly interacting Quark-Gluon Plasma (sQGP) as well as hadronization and the subsequent interactions in the expanding hadronic phase as in the Hadron-String Dynamics (HSD) transport approach [18,45]. The description of partonic degrees of freedom and their interactions in the PHSD is based on the Dynamical Quasiparticle Model (DQPM) [51–53] that is constructed to reproduce lattice QCD (lQCD) results for a quark-gluon plasma in thermodynamic equilibrium [44] at finite temperature T and baryon (or quark) chemical potential μ_q on the basis of effective propagators for quarks and gluons. Correspondingly, the EoS in the PHSD is the lQCD EoS of crossover type.

The dynamics of heavy-ion collisions within PHSD proceed as follows:

(i) Initially, the penetrating nuclei are initialized according to Wood-Saxon density distributions in coordinate space and by local Thomas-Fermi distributions in momentum space. The initial phase of nucleus-nucleus collisions starts with primary nucleon-nucleon scatterings from the impinging nuclei. The further

dynamics strongly depends on the collision energy. For low energy heavy-ion collisions the dynamics is driven by hadronic degrees of freedom with binary collisions, possible resonance excitations, and decays. However, with increasing bombarding energy the color-neutral strings are produced which decay to multiparticle states. In the PHSD the description of multiparticle production in elementary baryon-baryon (*BB*), meson-baryon (*mB*), and meson-meson (*mm*) reactions is realized within the Lund model [64] in terms of the event generators FRITIOF 7.02 [64] and PYTHIA 6.4 [65]. We note that in the PHSD the Lund event generators (FRITIOF 7.02 and PYTHIA 6.4) are "tuned," i.e., adjusted, to get a better agreement with experimental data on elementary $p + p$ collisions, especially at low energies (cf. Ref. [66]).

 (ii) If the local energy density is below the critical one for deconfinement ($\epsilon_c \simeq 0.5$ GeV/fm^3) the excited strings are dissolved into "prehadrons" (the string decay products) with a formation time of ≈ 0.8 fm/c in their rest frame, except for the "leading hadrons," i.e., the fastest residues of the string ends (quarks q or diquarks qq), which can reinteract (practically instantly) with hadrons with a reduced cross sections in line with the constituent quark contents.

We note that in Refs. [67,68] the chiral symmetry restoration effect was incorporated for the string decay in the dense hadronic medium that is created in the early stage of the reaction during the penetration of the colliding nuclei. The restoration of chiral symmetry is reflected in the dropping of the scalar quark condensate $\langle \bar{q}q \rangle$, which can be evaluated in the transport approach in each local cell within the nonlinear σ-ω model from the local scalar baryon and meson density according to the Hellman-Feynmann theorem. The dropping of the scalar quark condensate leads to a modification of the constituent quark masses for light and strange quarks bound in strings and thus affects the "chemistry" of decaying strings via the Schwinger mechanism [69]. This leads to an enhancement of strangeness production in the dense baryonic medium before the deconfined phase may set in [67,68].

 (iii) If the local energy density in the cell is above the critical value of $\epsilon_c \approx 0.5$ GeV/fm^3 [70], the "deconfinement" (i.e., a transition of hadronic to partonic degrees of freedom) is implemented by dissolving the "prehadrons" (in this cell) into the massive colored quarks/antiquarks and mean-field energy, keeping the "leading hadrons" out of dissolution (cf. Refs. [46,47] for details). This procedure allows one to keep the microscopic description of a changing degrees of freedom by conserving energy-momentum, charge, flavor, etc. The propagation of the off-shell partons in the hot and dense environment in the self-generated repulsive mean-field potential is realized by solving the Cassing-Juchem off-shell transport equations for test particles [44].

 (iv) The cross sections for the elastic and inelastic partonic interactions in the QGP phase are determined in the

DQPM model as well as the covariant transition rates for the hadronization to colorless off-shell hadrons when the local energy density decreases and become close to or lower than ϵ_c due to the expansion of the system. In PHSD 4.0 the partonic cross sections, evaluated from the widths in the quark/gluon propagators, depend only on T [71], while in the recent version PHSD 5.0 the cross sections are evaluated from the leading order scattering diagrams using the "resummed" propagators of the DQPM, and they have an explicit (T, μ_B) dependence [50]. However, for the present study we will use the PHSD 4.0 since we concentrate on low energies where the partonic phase is not relevant.

 (v) The final stage of a heavy-ion collision at relativistic energies is dominated by hadronic interactions. On the other hand, if the initial bombarding energy is too low for the formation of the QGP, as in the present study, the whole dynamics of the colliding system proceeds by interactions of hadronic degrees of freedom.

The hadronic degrees of freedom in the PHSD are the baryon octet and decuplet, the 0^- and 1^- meson nonets, and higher resonances. The hadronic interactions include elastic and inelastic collisions between baryons, mesons, and resonances (including the backward reactions through detailed balance) in line with the HSD approach [18,45]. We note that in the PHSD the multi-meson fusion reactions to baryon-antibaryon pairs and backward reactions (n mesons $\leftrightarrow$ $B + \bar{B}$) are included, too [72,73]. Following the formulation of the collision term for $n \leftrightarrow m$ reactions in [72,73], some other $3 \leftrightarrow 2$ reactions have been implemented recently in the PHSD as the nonresonant reactions $N + N \leftrightarrow N + N + \pi$ and $\pi + N \leftrightarrow N + \pi + \pi$ and for the dominant channel in strangeness production/absorption at the threshold by baryons ($B = N, \Delta$) and pions: $B + B \leftrightarrow N + Y + K$ and $\pi + B \leftrightarrow K + \bar{K} + N$ (as will be discussed in the next section).

We mention that at low energies a density-dependent Skyrme nucleon-nucleon potential is used for the mean-field propagation of nucleons, which corresponds to a "middle"-soft EoS (default in the PHSD) with the compression modulus $K \simeq 300$ MeV (cf. Sec. VII E). The nonstrange baryon resonances (such as Δ's) are propagated in the same manner as nucleons with the same NN potential while strange baryon resonances (such as Λ's, Σ's) feel only 2/3 of the nucleon-nucleon potential.

The PHSD incorporates also in-medium effects related to the changes of hadronic properties in the dense and hot environment during the time evolution of the system, such as a collisional broadening of the spectral functions of the light vector mesons (ρ, ω, ϕ, a_1) [74] and strange vector mesons $K^*, \bar{K}^*$ [75].

As mentioned in the Introduction, in Ref. [19] the in-medium modification of the strange mesons $K, \bar{K}$ has been implemented in HSD 1.5 using an early G-matrix approach. The propagation of broad states—described by the complex self-energies and medium-dependent cross sections—is only

possible in a consistent way by using the off-shell transport theory as reviewed in [44]. This provides a solid ground for the implementation of the novel G matrix described in Sec. II in the PHSD approach. The PHSD version, which incorporates the novel G matrix [56], we will denote by PHSD 4.5.

IV. ON-SHELL KAON, ANTIKAON PRODUCTION/ABSORPTION

We start with the description of the on-shell strangeness production channels in elementary baryon-baryon (BB), meson-baryon (mB), and meson-meson (mm) reactions (where $B = p, n, \Delta, \ldots$ and $m = \pi, \rho, \omega, \ldots$) as realized in the PHSD 4.5. Due to the strangeness conservation $s, \bar{s}$ quarks can be produced only in pairs, which implies the production of kaon-antikaon $K\bar{K}$ or kaon-hyperon pairs KY, where $Y = (\Lambda, \Sigma)$. We mention that the production mechanism strongly depends on the bombarding energy of the heavy-ion collision. At low energies only one or two hadrons are associated to the production of the strange pair, while with increasing energy multihadron states are energetically possible. The latter are realized within string excitation and decay.

A. Baryon+baryon scattering

There are only two channels for strangeness production in baryon+baryon scattering at low energy:

(i) The channel with the lowest threshold energy is $N + N \rightarrow N + Y + K$ with nucleon N, hyperon Y, and kaon K in the final state ($\sqrt{s_0} = m_N + m_\Lambda + m_K = 2.546$ GeV). We take into account the inverse reaction $N + Y + K \rightarrow N + N$ as well, which is relevant in dense baryonic matter and required by detailed balance. The implementation of the $N + Y + K \rightarrow N + N$ channel is realized by a calculation of the transition rate following Refs. [72,73]. The details of the numerical realization of $3 \rightarrow 2$ reactions in the PHSD are presented in Appendix B.

(ii) With increasing energy the strange pair can be produced in the channel $N + N \rightarrow N + N + K + \bar{K}$ [$\sqrt{s_0} = 2(m_N + m_K) = 2.862$ GeV].

The interactions of nucleons with Δ's (as well as $\Delta + \Delta$ interactions) are treated in the same way as $N + N$ interactions. We mention that the contribution of ΔN reactions (especially $\Delta + N \rightarrow N + Y + K$) is very important for strangeness production at (sub)threshold energies since the ΔN channel has a larger $\sqrt{s}$ compared to the scattering of two nucleons with the same kinetic energy as Δ and N. Moreover, since the density of Δ at SIS energies is high, the ΔN channels dominate NN channels. The quantitative results on this issue will be presented in Sec. VI.

The cross sections for both channels and the inverse reactions of the first channel $N + Y + K \rightarrow N + N$ are, respectively, described in Appendices A and B.

With further increasing collision energy the string formation and fragmentation becomes the main source of strangeness production. The threshold for the formation of

baryon-baryon strings is taken in the PHSD as $\sqrt{s_{th}}(BB$ str$) = 2.65$ GeV.

B. Meson+baryon scattering

Dominant channels for kaon production in meson+baryon scattering are $\pi + N \rightarrow K + Y$ and $\pi + N \rightarrow K + \bar{K} + N$ with cross sections given in Appendix A. We also account for the inverse process $N + K + \bar{K} \rightarrow N + \pi$ by detailed balance (see Appendix B).

As found first in Ref. [76] and supported by other transport calculations [16,24], the most important channel for antikaon production in nucleus-nucleus collisions is $\pi + Y \rightarrow N + \bar{K}$, which involves two secondary particles since the hyperons and pions have to be first produced by initial NN collisions. The $\pi + Y \rightarrow N + \bar{K}$ cross section is related to the inverse reaction $N + \bar{K} \rightarrow \pi + Y$ by detailed balance:

$$
\begin{aligned}
\sigma_{\pi Y \rightarrow \bar{K} N}(s) &= \frac{D_{\bar{K}} D_N}{D_\pi D_Y} \left(\frac{p_{\bar{K}}}{p_\pi}\right)^2 \sigma_{\bar{K} N \rightarrow \pi Y}(s) \\
&= \frac{D_{\bar{K}} D_N}{D_\pi D_Y} \frac{\{s - (m_{\bar{K}} + m_N)^2\}\{s - (m_{\bar{K}} - m_N)^2\}}{\{s - (m_\pi + m_Y)^2\}\{s - (m_\pi - m_Y)^2\}} \\
&\quad \times \sigma_{\bar{K} N \rightarrow \pi Y}(s),
\end{aligned}
\tag{31}
$$

where D_i is the degeneracy factor of particle i, and p_π and $p_{\bar{K}}$ are, respectively, the momenta of pion and antikaon in the c.m. frame. The cross section for $N + \bar{K} \rightarrow \pi + Y$ is provided by the G-matrix approach described in Sec. II, if the initial and final states are included in Eqs. (6) and (7).

The reactions of mesons with Δ's are taken into account, too. For example, for the interactions with Δ's such as $\Delta + \bar{K} \rightarrow \pi + Y$, the cross sections are given in Appendix A.

At energies above the threshold for the string formation in baryon+meson collisions, which is taken to be $\sqrt{s_{th}}(mB$ str$) = 2.4$ GeV in the PHSD, strangeness can be produced in an associated multihadron environment.

C. Meson+meson scattering

The most dominant channel for kaon and antikaon production from meson scattering is $\pi + \pi \rightarrow K + \bar{K}$ which is given by $\simeq 3$ mb [77]. If the total electric charge is $+1$ or -1, there is only one channel: $\pi^+ + \pi^0 \rightarrow K^+ + \bar{K}^0$ or $\pi^0 + \pi^- \rightarrow K^0 + K^-$. On the other hand, $\pi^+ + \pi^-$ and $\pi^0 + \pi^0$ can produce either $K^+ + K^-$ or $K^0 + \bar{K}^0$. We assume that

$$
\begin{aligned}
\sigma_{\pi^+ \pi^- \rightarrow K^+ K^-} &= \sigma_{\pi^+ \pi^- \rightarrow K^0 \bar{K}^0} \\
&= \sigma_{\pi^0 \pi^0 \rightarrow K^+ K^-} = \sigma_{\pi^0 \pi^0 \rightarrow K^0 \bar{K}^0} = 1.5 \text{ [mb]}, \\
\sigma_{\pi^+ \pi^0 \rightarrow K^+ \bar{K}^0} &= \sigma_{\pi^- \pi^0 \rightarrow K^- K^0} = 3 \text{ [mb]}.
\end{aligned}
\tag{32}
$$

The annihilation of K and $\bar{K}$ is taken into account by the detailed balance consistently.

Again, at relativistic energies the strangeness can be produced by the excitation and decay of meson-meson strings above the threshold, which is taken to be $\sqrt{s_{th}}(mm$ str$) = 1.3$ GeV.

D. Resonance decays

The decay of $K^*(\bar{K}^*)$ and ϕ mesons produces an (anti)kaon and antikaon-kaon pairs, respectively. $K^*(\bar{K}^*)$ decays into $K(\bar{K})\pi$ with almost 100% probability, while the ϕ meson decays into K^+K^- with 49.2% and $K^0_L K^0_S$ with 34% [78]. The total decay widths of $K^*(\bar{K}^*)$ and ϕ are respectively about 50 and 4 MeV in vacuum [78] (and getting broader in the medium).

V. OFF-SHELL KAON, ANTIKAON PRODUCTION/ABSORPTION

The properties of (anti)kaons are modified in nuclear matter with respect to the vacuum. The energy or the rest mass of the kaon increases in nuclear matter while that of the antikaon decreases. This effectively shifts the threshold energy for kaon production up and that of antikaon production down.

The modification of the reaction thresholds in the nuclear medium has important consequences for the strangeness production: the reduction of the antikaon threshold leads to an enhancement of antikaon production in the medium. Moreover, it opens subthreshold, i.e., below the vacuum threshold, production of antikaons. This subthreshold antistrangeness production in $A + A$ reactions—with respect to the elementary $N + N$ reactions—is an exciting experimental discovery and has been extensively studied by transport models in the past (cf. the review for details [24]). In contrast to antikaons, the kaon threshold in the nuclear medium is shifted to larger energies, i.e., above the vacuum threshold for corresponding elementary BB and mB ($B = N, \Delta$) reactions for kaon production, which suppresses the production of kaons in $A + A$ collisions when accounting for the in-medium effects compared to the calculations without medium effects.

In this section we present our modeling of the in-medium strangeness production and propagation which accounts for the modification of the (anti)kaon properties in the nuclear environment. We stress that the antikaon scattering in the medium is evaluated following the coupled-channel G-matrix approach as described in Sec. II.

A. Antikaon production in the nuclear medium

The antikaon production cross section in the medium is evaluated by folding the corresponding vacuum production cross section with the in-medium spectral function in Eq. (29):

$$\sigma^*_{\bar{K}}(\sqrt{s}) = \int_0^{(\sqrt{s}-m_4)^2} \frac{dm^2}{2\pi} A(m^2)\, \sigma_{\bar{K}}(\sqrt{s} - \Delta m_{\bar{K}}), \quad (33)$$

where m_4 is the invariant mass of the final particles different from antikaons (i.e., for $\bar{K}$ production via $1 + 2 \to \bar{K} + X$, m_4 is the mass of all particles X), m is the off-shell mass of the $\bar{K}$ meson in the medium defined by the spectral function $A(m^2)$ according to Eq. (29), $m_{\bar{K}}$ is the vacuum mass of the antikaon in the final state, and $\Delta m_{\bar{K}} = m - m_{\bar{K}}$ describes the deviation from the vacuum mass. In Eq. (33) we have assumed that the mass shift of the antikaon is realized in the scattering cross section by a shift of the incoming invariant energy $\sqrt{s}$. An explicit derivation is given in Appendix C. The mass of a produced antikaon is determined by a Monte Carlo procedure

on the basis of the probability distribution function

$$\frac{dP(m^2)}{dm^2} = \frac{A(m^2)\, \sigma_{\bar{K}}(\sqrt{s} - \Delta m_{\bar{K}})}{2\pi \sigma^*_{\bar{K}}(\sqrt{s})}. \quad (34)$$

The self-energy of the antikaon, which fully determines the spectral function, explicitly depends on the antikaon three-momentum in the rest frame of the nuclear medium. In the present study we take the velocity of the c.m. frame of the scattering particles in the medium as the antikaon velocity assuming that the kinetic energy of the antikaon is small in the c.m. frame. In other words, the three-momentum of the antikaon in the nuclear medium—on which self-energy depends—is given by $m_K \gamma \vec{\beta}$ with m_K and $\vec{\beta}$ being the antikaon mass in vacuum and the velocity of the c.m. frame in the medium (with $\gamma = 1/\sqrt{1 - \beta^2}$). Considering that the collision energy of heavy ions in the present study is close to the threshold energy for antikaon production, this should be a reasonable approximation.

B. Antikaon propagation in the nuclear medium

The equations of motion for off-shell particles are given by the Cassing-Juchem off-shell transport equations for test particles [42] used also for the propagation of antikaons in the early HSD study [19]:

$$\frac{dr_i}{dt} = \frac{1}{1-C} \frac{1}{2E} \left[2p_i + \nabla_p \operatorname{Re}\Sigma + \frac{M^2 - M_0^2}{\operatorname{Im}\Sigma} \nabla_p \operatorname{Im}\Sigma \right], \quad (35)$$

$$\frac{dp_i}{dt} = \frac{-1}{1-C} \frac{1}{2E} \left[\nabla_r \operatorname{Re}\Sigma + \frac{M^2 - M_0^2}{\operatorname{Im}\Sigma} \nabla_r \operatorname{Im}\Sigma \right], \quad (36)$$

$$\frac{dE}{dt} = \frac{1}{1-C} \frac{1}{2E} \left[\partial_t \operatorname{Re}\Sigma + \frac{M^2 - M_0^2}{\operatorname{Im}\Sigma} \partial_t \operatorname{Im}\Sigma \right], \quad (37)$$

where M_0 is the pole mass in vacuum, $M^2 = E^2 - p_i^2 - \operatorname{Re}\Sigma$, and

$$C = \frac{1}{2E} \left[\frac{\partial}{\partial E} \operatorname{Re}\Sigma + \frac{M^2 - M_0^2}{\operatorname{Im}\Sigma} \frac{\partial}{\partial E} \operatorname{Im}\Sigma \right]. \quad (38)$$

However, as shown in Appendix D, the time evolution of the off-shell particle mass is more practical for actual calculations than the time evolution of the energy, and Eq. (37) is substituted by

$$\frac{dM^2}{dt} = \frac{M^2 - M_0^2}{\operatorname{Im}\Sigma} \frac{d\operatorname{Im}\Sigma}{dt}, \quad (39)$$

which manifests directly that the off-shell mass M approaches M_0 as the imaginary part of the self-energy converges to zero when propagating in the vacuum where the antikaon is on shell, i.e., stable with respect to strong interaction.

C. Kaons in nuclear matter

In this study we assume that the kaon-nuclear potential increases linearly with baryon density ρ as

$$V_K = 25\,\text{MeV} \times (\rho/\rho_0), \quad (40)$$

where ρ_0 is the nuclear saturation density (taken to be $0.16/\text{fm}^3$). Since the single-particle energy of the kaon, $\mathcal{E}$, in nuclear matter is approximated in the nonrelativistic limit by

$$\mathcal{E} = \sqrt{m_K^2 + p^2 + \text{Re}\,\Sigma} \simeq E_K + \frac{\text{Re}\,\Sigma}{2E_K} = E_K + V_K, \quad (41)$$

where m_K is the kaon mass in vacuum, $\text{Re}\,\Sigma$ is the real part of the kaon self-energy and $E_K = \sqrt{m_K^2 + p^2}$. The in-medium kaon mass m_K^* is expressed in terms of V_K as follows:

$$m_K^* = \sqrt{m_K^2 + \text{Re}\,\Sigma} = \sqrt{m_K^2 + 2E_K V_K}$$
$$\simeq m_K\left(1 + \frac{E_K V_K}{m_K^2}\right) \simeq m_K\left(1 + \frac{25\,\text{MeV}}{m_K}\frac{\rho}{\rho_0}\right). \quad (42)$$

As in the case of antikaon production, the cross section is shifted by the mass difference:

$$\sigma_{NN\to NYK}(\sqrt{s}) \to \sigma_{NN\to NYK^*}(\sqrt{s} - \Delta m_K), \quad (43)$$

where $\Delta m_K = m_K^* - m_K$. Since Δm_K is positive, the mass shift suppresses K production in heavy-ion collisions.

In some scattering channels such as $N + N \to N + N + K + \bar{K}$ and $\pi + N \to N + K + \bar{K}$, the kaon and antikaon are simultaneously produced. In this case the cross section is expressed as the combination of Eqs. (33) and (43):

$$\sigma_{K\bar{K}}^*(\sqrt{s}) = \int_0^{(\sqrt{s}-m_4)^2} \frac{dm^2}{2\pi} A(m^2) \sigma_{K\bar{K}}(\sqrt{s} - \Delta m_K - \Delta m_{\bar{K}}). \quad (44)$$

The production of kaon and antikaon through the decay of K^* and ϕ is also modified in nuclear matter. Assuming that the transition amplitude does not depend on the mass of the daughter particle, as shown in Appendix C, the mass distribution of the antikaon—produced from the decay—follows

$$\frac{dP(m^2)}{dm^2} = \frac{A(m^2) p^{\text{c.m.}}(m^2)}{8\pi^2 M^2 \Gamma} = A(m^2)$$
$$\times \frac{\sqrt{\{M^2 - (m+m_2)^2\}\{M^2 - (m-m_2)^3\}}}{(4\pi)^2 M^3 \Gamma}, \quad (45)$$

where $p^{\text{c.m.}}$ is the three-momentum of the antikaon in the c.m. frame and M and m_2 are, respectively, the masses of the mother particle and the other daughter particle different from the antikaon.

The position and momentum of the kaon are updated in nuclear matter according to the equations of motion given by

$$\frac{dr_i}{dt} = \frac{\partial H}{\partial p_i} = \frac{p_i}{E},$$
$$\frac{dp_i}{dt} = -\frac{\partial H}{\partial r_i} = -\nabla V_K(r), \quad (46)$$

where $i = 1, 2, 3$. The kaon energy is defined by Eq. (41).

VI. $K/\bar{K}$ PRODUCTION IN HEAVY-ION COLLISIONS

We step now to the investigation of strangeness dynamics in heavy-ion collisions within the PHSD 4.5 which incorporates the strangeness cross sections and their modifications in

the medium (defined in Sec. V) and the off-shell propagation of antikaons according to Eqs. (35)–(39). The kaon cross sections and potential depend on the baryon density while the antikaon properties, defined by self-energies of the G matrix, depend on the baryon density, the temperature, and the three-momentum of the antikaon in the rest frame of the medium.

Figure 4 shows the distributions of baryon density, temperature, and momentum in the matter rest frame of K^+ and K^- at their production points for individual production channels and for their sum (solid black lines) in central Au+Au collisions at $1.5A$ GeV. The PHSD calculations include the in-medium effects, i.e., a repulsive potential for K^+ and the self-energy from the G-matrix approach for K^-. The channel decomposition involves nonstrange baryons B, hyperons $Y = (\Lambda, \Sigma)$, and nonstrange mesons m. From the upper row of Fig. 4 one can see that the density at K^+ production is larger than at K^- production. That is due to the fact that the main production channel of K^+'s is $B + B \to B + Y + K$, which occurs promptly in heavy-ion collisions, while K^-'s are produced not directly but in two steps, first $B + B \to B + Y + K$ and then $Y + m \to B + \bar{K}$. We note that we consider here central Au+Au collisions at $b = 0$ fm, where the pion density is larger than for the minimal bias selection. This enhances the contribution from $B + \pi \to Y + K$ compared to that from $B + B \to B + Y + K$ for the K^+ production. There are many production channels which are not explicitly shown in the figure. For example, $\pi + \pi \to K + \bar{K}$ and $B + m \to B + K + \bar{K}$ are only shown for K^- production, though they contribute to both K^+ and K^- production, because their relative contribution to K^+ production is small. The lines indicated as "other" channels in Fig. 4 for K^+ and K^- production include ϕ decay, $B + B \to B + B + K + \bar{K}$, and string decay of $B + B$, $B + m$ and $m + m$ (if the final state is different from the channels listed in the figure explicitly). The channels $Y + m \to \Xi + K$, $\Xi^0 + K^0 \to \Xi^- K^+$ contribute only to K^+ production and $\Xi + K \to B + \bar{K}$ and $\Xi + m \to Y + \bar{K}$ only to K^- production are also included in "the others."

The strangeness production in heavy-ion collisions at threshold energies is dominated by secondary reactions in the hadronic medium, i.e., through multistep processes. For example, the primary nucleon+nucleon scattering excites either one or both nucleons into a Δ, a process which is more favorable than NN to produce strangeness via $\Delta + N \to N + Y + K$, because the Δ is heavier than the nucleon. Or the Δ decays into a nucleon and a pion which produces strangeness via $B + \pi \to Y + K$.

In order to quantify the importance of secondary processes involving Δ's and pions, we present in Table I the number of produced K^+'s per event in subchannels of the channels $B + m \to Y + K$, $B + B \to B + Y + K$, and $B + m \to B + K + \bar{K}$, depending on whether the Δ baryon is involved in strangeness production or not. In the case of $B + m \to Y + K$ about 20% of K^+ production is induced by a Δ baryon. On the other hand, $\Delta + N \to B + Y + K$ is about 80% more frequent than $N + N \to B + Y + K$. However, $\Delta + \Delta \to B + Y + K$ is kinematically more favorable for K^+ production, but it is less frequent since the possibility that two Δ's scatter is lower. In the case of $B + m \to B + K + \bar{K}$ the contribution from $N + m$ and that from $\Delta + m$ are similar. We note that
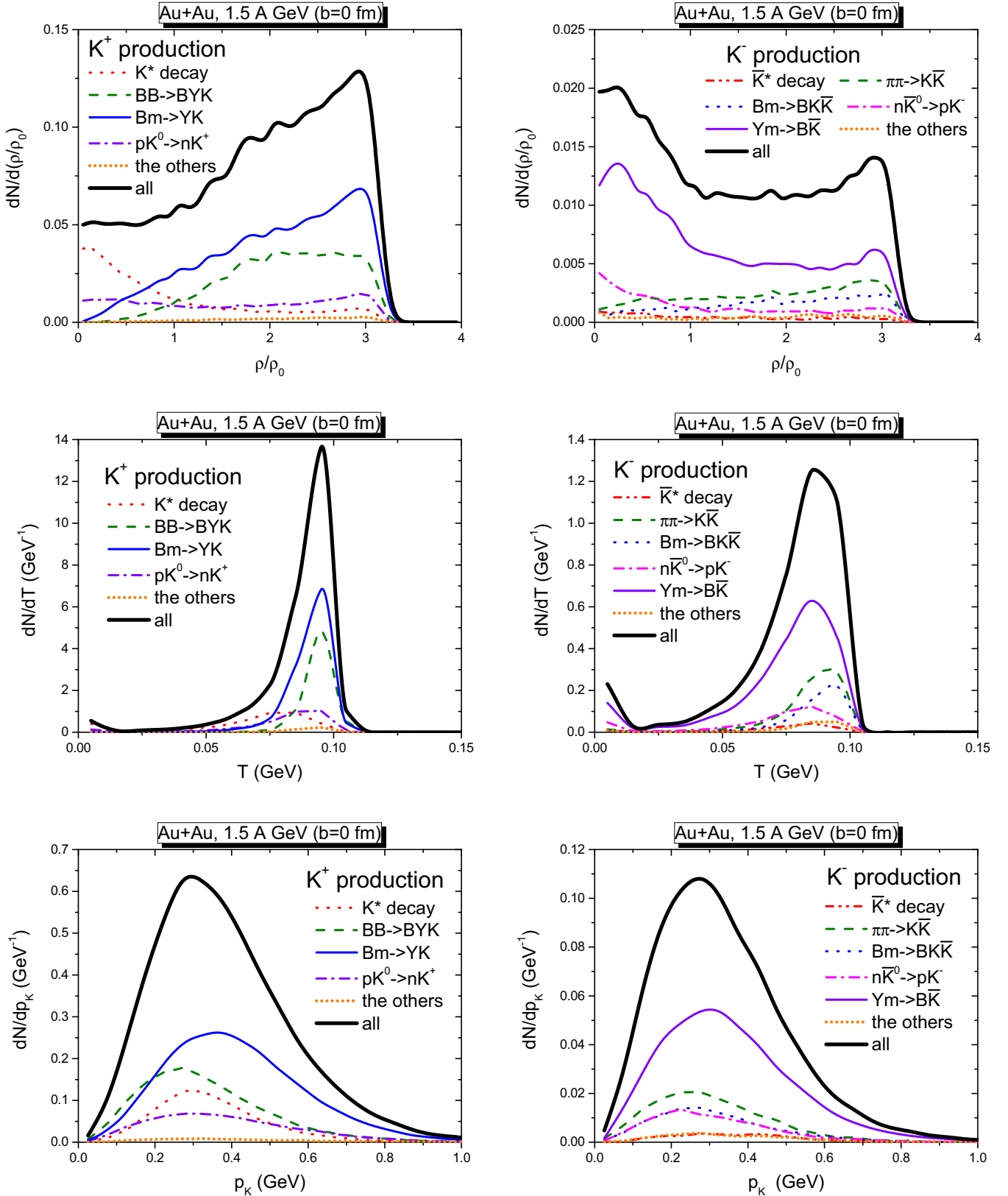
FIG. 4. The distributions in baryon density ρ/ρ_0 (upper), temperature T (middle), and momentum p_K in the matter-rest frame (lower) for K^+'s (left) and K^-'s (right) at their production points in central Au+Au collisions ($b = 0$ fm) at $1.5A$ GeV. The lines show the individual production channels involving nonstrange baryons B, hyperons $Y = (\Lambda, \Sigma)$, and nonstrange mesons m. The PHSD calculations include the in-medium effects, i.e., a repulsive potential for K^+ and the self-energy from the G-matrix approach for K^-.

TABLE I. The number of produced K^+'s (with in-medium effects) per event from several channels in central Au+Au collisions ($b = 0$ fm) at 1.5A GeV.

Channel	Produced K^+ per event
$N + m \rightarrow Y + K$	8.79×10^{-2}
$\Delta + m \rightarrow Y + K$	2.30×10^{-2}
$N + N \rightarrow B + Y + K$	1.87×10^{-2}
$N + \Delta \rightarrow B + Y + K$	3.39×10^{-2}
$\Delta + \Delta \rightarrow B + Y + K$	1.22×10^{-2}
$N + m \rightarrow B + K + \bar{K}$	8.79×10^{-4}
$\Delta + m \rightarrow B + K + \bar{K}$	8.79×10^{-4}

the contribution of each subchannel depends on the collision system and energy as well as on centrality. It is worth noting that the contribution from $K^*(\bar{K}^*)$ decay is not negligible for $K^+(K^-)$ production. Thus up to 15% for K^+ and 3.7% for K^- come from their decays. Since the decay width of the $K^*(\bar{K}^*)$ is about 50 MeV, their decays ($K^* \rightarrow K + \pi$ or $\bar{K}^* \rightarrow \bar{K} + \pi$) happen on average 4 fm/c after $K^*(\bar{K}^*)$ production. Therefore the baryon density at $K(\bar{K})$ production through $K^*(\bar{K}^*)$ decays is quite low as follows from Fig. 4. On the other hand, the ϕ decay barely contributes to (anti)kaon production: 0.07% for K^+ and 0.67% for K^-.

The middle panels in Fig. 4 show the temperature distributions at the K^+ and K^- production points. The temperature is extracted from the local energy density and baryon density by using the Hadron Resonance Gas model (HRG) which includes all mesons up to 1.5 GeV of mass and all (anti)baryons up to 2 GeV, i.e., in line with the hadronic degrees of freedom of the PHSD. A similar HRG model has been used in the past to study the thermal equilibration in infinite hadron-string matter as well as in HICs within the Boltzmann-Uehling-Uhlenbeck model (BUU) [79]; however, here we consider all hadrons "on-shell," i.e., we neglect their spectral functions (as realized in most of the statistical models, cf. [80]), which might slightly influence the final temperature [79]. Although the produced nuclear matter is not in complete thermal equilibrium, we calculate local energy density and baryon density in the rest frame of the local cell and map them into those from the HRG model to obtain a corresponding temperature, which is a commonly used method in coarse graining. Indeed, such mapping of nonequilibrium distributions to its equilibrium values can be considered only as a leading order approximation. However, we note that the temperature dependence of the antikaon spectral function is relatively weak compared to its density dependence which washes out the uncertainties related to the extraction of local temperatures within our HRG model.

One can see that the temperature distribution is highly peaked around $T = 90$–100 MeV for K^+ while in the case of K^- it is less sharply peaked around $T = 80$–90 MeV. Considering that K^+ is produced earlier than K^-, this is expected. In addition, the temperature distribution of $K^*(\bar{K}^*)$ decay is lower than for the other channels, since it happens later when the matter is cooling due to the expansion.
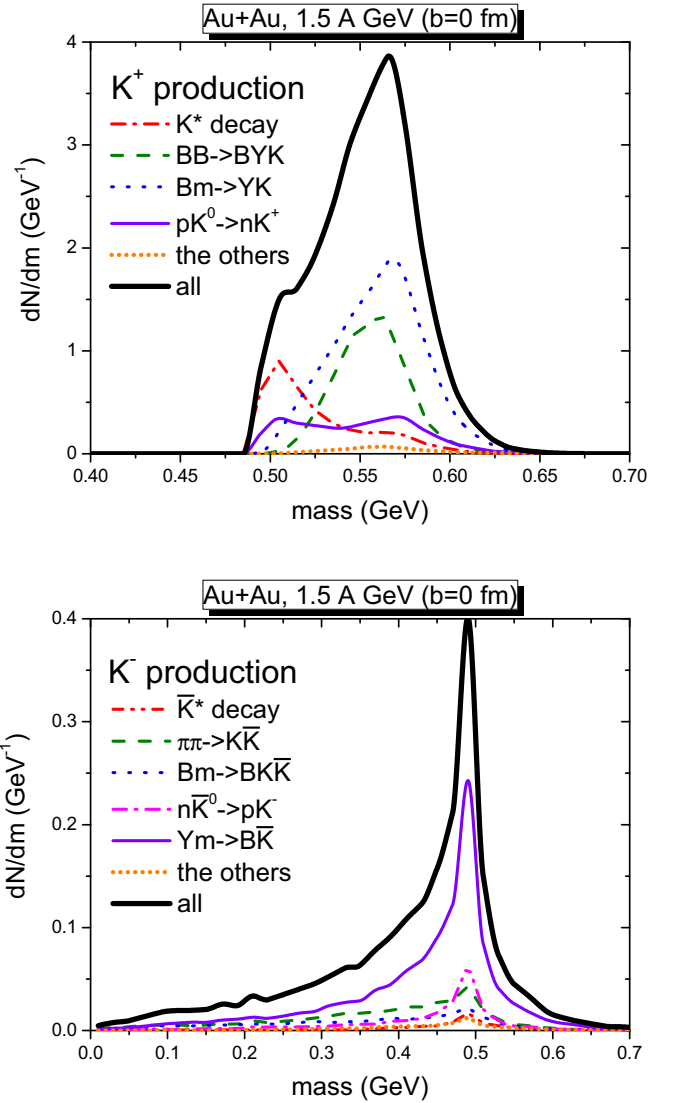

FIG. 5. The mass distribution of K^+'s (upper) and K^-'s (lower) at their production points in central Au+Au collisions ($b = 0$ fm) at 1.5A GeV. The lines show the individual production channels. The PHSD calculations include the in-medium effects for K^+ and K^-.

The distributions in three-momentum of the (anti)kaon at its production time in the local rest frame of the baryon matter are displayed in the lower panels of Fig. 4. The figure shows that the three-momentum of K^+ is peaked around 300 MeV/c, while for K^- it is a bit lower. In general the three-momentum of K^+ is slightly larger than that of K^-, though the distributions are quite similar. One can also find that the momentum of K^+ from $B + m \rightarrow Y + K$ is larger than that from other channels and K^- from $Y + m \rightarrow B + \bar{K}$ has a larger momentum than that from $\pi + \pi \rightarrow K + \bar{K}$.

Figure 5 shows the mass distributions of K^+'s (upper plot) and K^-'s (lower plot) at their production points in central Au+Au collisions ($b = 0$ fm) at 1.5A GeV by summing up all production contributions discussed above with respect to Fig. 4. The K^+ mass in the medium mainly depends on the baryon density as follows from Eq. (42). Considering that
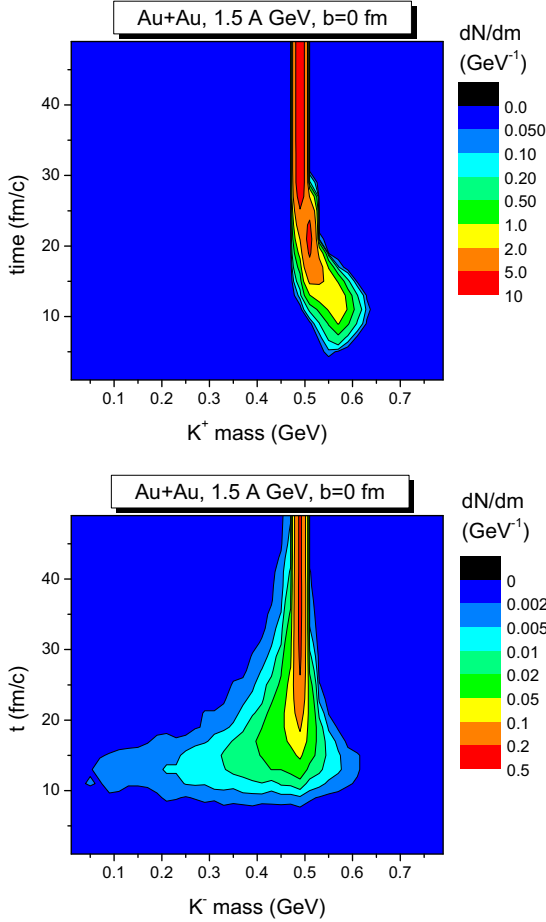
FIG. 6. The contour plot for the mass distributions of K^+'s (upper) and K^-'s (lower) as a function of time in central Au+Au collisions ($b = 0$ fm) at $1.5A$ GeV. The PHSD calculations include the in-medium effects for K^+ and K^-.
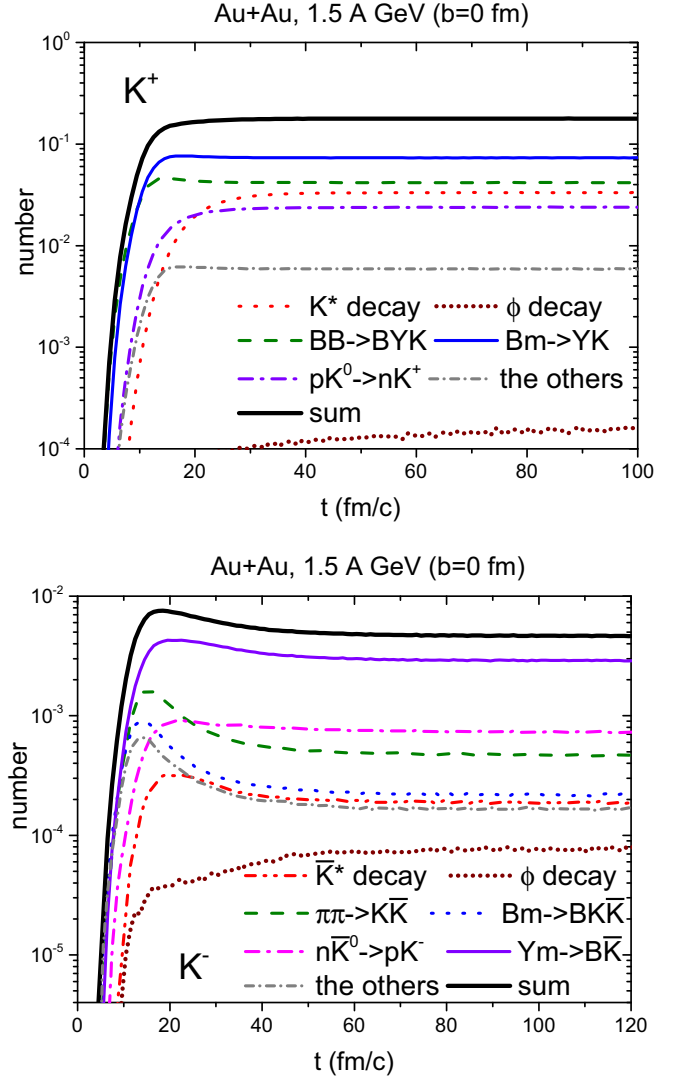

FIG. 7. The channel decomposition for K^+ (upper) and K^- (lower) production as a function of time in central Au+Au collisions ($b = 0$ fm) at $1.5A$ GeV. The PHSD calculations include the in-medium effects for K^+ and K^-.

the baryon density at K^+ production is peaked around $3\rho_0$ (as follows from Fig. 4), it is consistent that the K^+ mass is distributed around 560–570 MeV in Fig. 5. We note that the K^+ mass from the K^* decay is relatively low because this decay happens later at low baryon densities.

On the other hand, the K^- mass depends on baryon density, temperature, and the three-momentum of the antikaon in the rest frame of the baryonic medium through the self-energy of the antikaon. Figure 4 shows that the K^- is produced in a wide range of baryon densities from 0 to $3\rho_0$ and at temperatures between 50 and 100 MeV with the three-momentum peaking at 200–400 MeV/c. As follows from Fig. 2, the absolute value of the real part of the K^- self-energy rapidly decreases with increasing antikaon momentum and is less than 20 MeV for $p = 300$ MeV/c, while the imaginary part is not much affected by the change of momentum. Therefore, the pole mass of the K^- spectral function changes only slightly and the spectral width broadens as shown in Fig. 5.

Figure 6 shows the contour plot for the mass distributions of K^+'s (upper plot) and K^-'s (lower plot) as a function of time for central Au+Au collisions ($b = 0$ fm) at $1.5A$ GeV. While at the production times the masses of K^+ and K^- are

highly off-shell they approach dynamically (according to the off-shell propagation) to the on-shell masses following the decrease of the baryon density and temperature with time according to Eqs. (39) and (42), respectively. As displayed in Fig. 5, the K^+ mass is initially larger than the vacuum mass while the pole position of the K^- mass is close to the vacuum mass with a large spreading in spectral width towards lower masses. The decrease of the baryon density with time leads to a reduction of the off-shell K^+ mass to the vacuum mass and shrinks the K^- spectral function such that the width vanishes in vacuum.

We show in Fig. 7 the channel decomposition of the K^+ and K^- production as a function of time in central Au+Au collisions ($b = 0$ fm) at $1.5A$ GeV where the color lines indicate the dominant production channels. One can see that the K^+ production via the $B + B \rightarrow B + Y + K$ reaction takes place early, dominantly due to initial $N + N$ scatter-

TABLE II. The numbers of produced and survived K^+ and K^- mesons per event from several channels in central Au+Au collisions ($b = 0$ fm) at 1.5A GeV. The PHSD calculations are done including the in-medium effects for K^+ and K^-.

Channel	Produced	Survived
total K^+	2.57×10^{-1}	1.68×10^{-1}
$B + B \to B + Y + K$	6.48×10^{-2}	3.92×10^{-2}
$B + m \to Y + K$	1.13×10^{-1}	6.90×10^{-2}
$p + K^0 \to n + K^+$	3.15×10^{-2}	2.25×10^{-2}
$K^* \to \pi + K$ decay	3.89×10^{-2}	3.14×10^{-2}
total K^-	4.10×10^{-2}	4.13×10^{-3}
$B + m \to B + K + \bar{K}$	4.57×10^{-3}	1.85×10^{-4}
$n + \bar{K}^0 \to p + K^-$	4.65×10^{-3}	6.19×10^{-4}
$Y + m \to B + \bar{K}$	2.16×10^{-2}	2.61×10^{-3}
$\pi + \pi \to K + \bar{K}$	7.42×10^{-3}	3.69×10^{-4}
$\bar{K}^* \to \pi + \bar{K}$ decay	1.41×10^{-3}	2.0×10^{-4}

ing. The channels involving secondary particles—mesons or baryons—come with some delay, since their production also needs some time. The $B + m \to Y + K$ channel involves produced mesons; the isospin exchange reactions ($p + K^0 \to n + K^+$) can happen only after kaons (K^0) are produced; the K^* decays come even with a larger delay due to their later production.

In the case of K^-'s, the reactions $Y + m \to B + \bar{K}$, $\pi + \pi \to K + \bar{K}$, and $B + m \to B + K + \bar{K}$ take place at a similar time after meson production, dominantly pions from Δ decays. After that the isospin exchanges ($n + \bar{K}^0 \to p + K^-$) and then K^* decays are involved. As follows from Fig. 7, the dominant channel for K^- production is a meson-hyperon reaction which is in line with previous findings [16,24,76]. We note that many antikaons are absorbed after production because the absorbtion cross section of antikaons by nucleons is very large (cf. Fig. 1). That is why the K^- masses in Fig. 6 bent down after initial strong rise.

Table II lists the number of produced and surviving K^+'s and K^-'s for each production channel per event in central Au+Au collisions at 1.5A GeV. One can see that about 65% of produced K^+ mesons survive, while only 10% of K^- remain and the other K^- are absorbed by nucleons or switched to $\bar{K}^0$ by isospin exchange. The survival probability of K^+ from K^* decay is relatively large and amounts to 81%, because the K^* decays happen later (at low baryon density) than for other production channels.

We note that (anti)kaon production in Table II as well as in Figs. 4 and 5 does not only include primary production but also secondary and third productions, e.g., a K^+ turns to a K^0 by isospin exchange and then returns to K^+ by another isospin exchange. In this case K^+ production is counted twice.

Figure 8 shows the rapidity distribution and p_T spectra within the rapidity window $|y| < 0.5$ of K^+ and K^- mesons at freeze-out in central Au+Au collisions at 1.5A GeV. The integrated yields correspond to the numbers in the right column ("survived") of Table II. The black dashed lines show the rapidity distribution of K^+ and K^- at the production point normalized to the total number of surviving (anti)kaons (solid black lines). The colored lines indicate the different production channels of the surviving K^+, K^- mesons. One can see that the rapidity distribution of surviving K^+ mesons is broader than that of produced K^+ while the rapidity distribution of surviving K^- has practically the same shape as at production.

The lower panels of Fig. 8 show the m_T spectra of K^+ and of K^-. Again the colored lines indicate the different production channels of surviving K^+, K^- mesons. One can see that the production channels have slightly different shapes; however, the final shape is related to the dominant channels: $B + m \to YK$ for K^+ mesons and $Y + m \to B + \bar{K}$ for K^- mesons. The final m_T spectrum (black solid line) of K^+ mesons is harder than that at the production point (black dashed line), while the final K^- spectrum becomes slightly softer.

We note (without showing the results explicitly) that the channel decomposition depends on the system size: the lighter the colliding system is, the larger is the role of primary baryon-baryon collisions for K^+ production. For a light system as C+C, the production of K^+ by the $BB \to BYK$ reactions exceeds that by the $Bm \to YK$ reactions which is dominant channel for Au+Au collisions at the same energy of 1.5A GeV; cf. Fig. 8. The K^- mesons are dominantly produced by secondary reactions involving mesons and hyperons. Such the $Ym \to B\bar{K}$ channel is dominant for the C+C collisions similar to the Au+Au collisions. The total yield is, however, substantially reduced due to the low abundances of produced hyperons and mesons in C+C collisions as compared to more heavy systems.

The modification of the final rapidity and m_T-distributions of the K^+ and K^- mesons has two origins [24]: the rescattering in the hadronic medium and the in-medium effects in terms of a repulsive potential for K^+ and self-energies within the G-matrix approach for K^-. The influence of each effect is quantified in Fig. 9: The upper plot displays the p_T distributions of produced (initial) (i) and surviving (final) K^+ and K^- mesons without in-medium effects in central Au+Au collisions at 1.5A GeV at midrapidity (which corresponds to the angular cut $|\theta - 90°| < 10°$). Since the number of produced (anti)kaons is different than that of surviving (anti)kaons, the initial distribution is normalized to the number of surviving (anti)kaons for easy comparison. One can see that both p_T distributions of the produced K^+ and K^- are shifted to larger transverse momenta due to scattering/absorption in the medium with baryons and mesons. We note that the K^- absorption is stronger for slow K^-. (ii) The lower panel of Fig. 9 shows the PHSD results including the kaon potential and the self-energy within the G-matrix approach for K^-. One sees that the p_T distribution of the surviving K^+ is further shifted to larger p_T due to the repulsive forces. On the other hand, the p_T distribution of surviving K^- is shifted back to small p_T because of the attractive potential related to the real part of antikaon self-energy and partially due to the broadening of the spectral function related to the imaginary part of the self-energy (as will be also discussed in Sec. VII A). As a result, the final p_T distribution turns out to be not far from the p_T distribution of the produced K^-, as]already seen in the m_T spectra of K^- in Fig. 8 (lower, right). We note also that—as demonstrated in Fig. 8—the shape of the K^- m_T (or
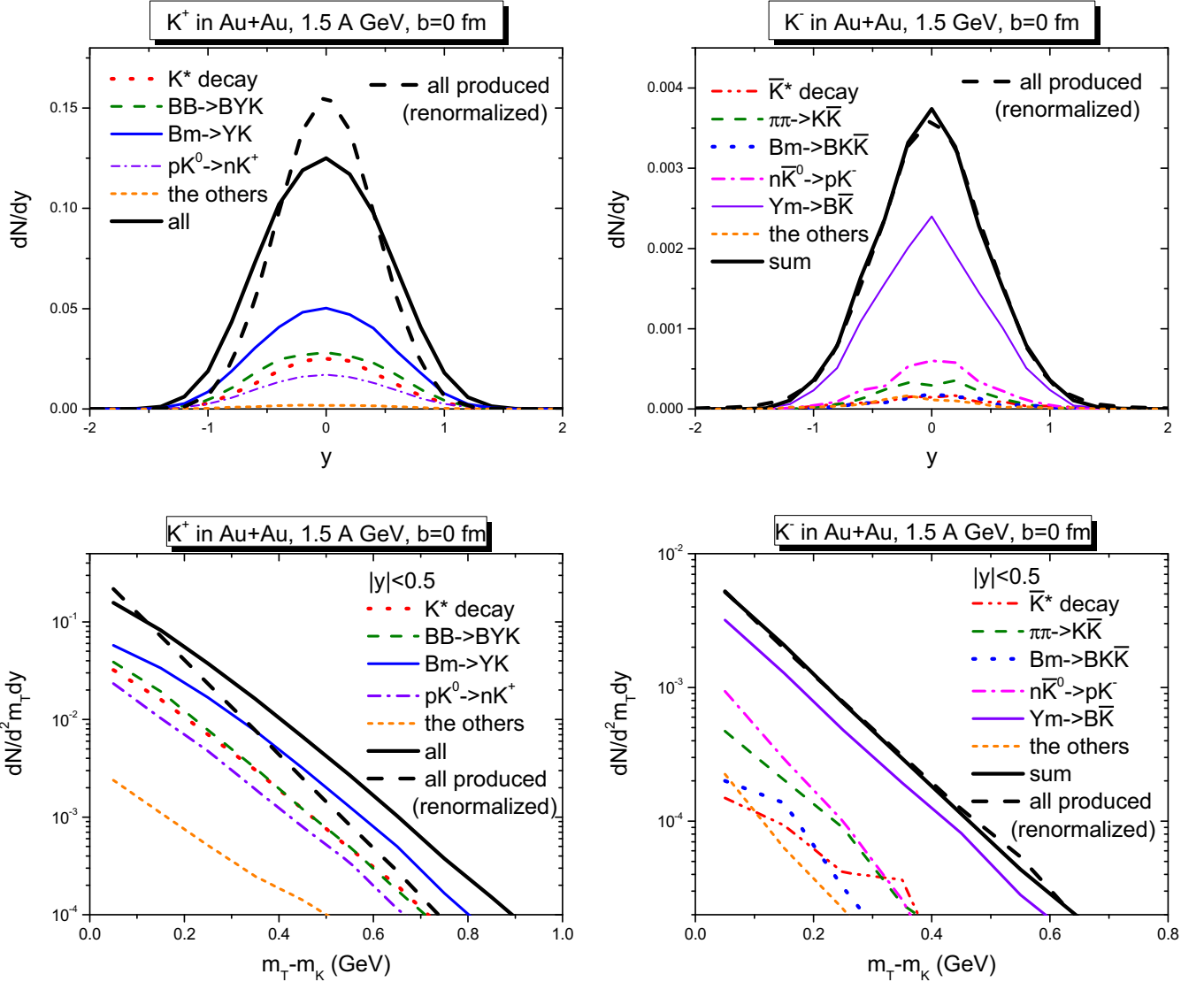
FIG. 8. The rapidity distributions (upper) and m_T spectra (lower) of K^+ (left) and K^- (right) mesons at freeze-out (i.e. survived) in central Au+Au collisions ($b = 0$ fm) at 1.5A GeV. The colored lines show the different production channels. The black dashed lines show the rapidity distribution of K^+ and K^- at the production point normalized to the total number of survived (anti)kaons (solid black lines). The PHSD calculations include the in-medium effects for K^+ and K^-.

p_T) distribution follows the shape of the dominant production channel $Y + m \rightarrow B + \bar{K}$ (cf. also Fig. 7) which involves the secondary particles, i.e., such processes happen with a time delay when the density of the system is decreasing due to the expansion. Consequently, the K^- mesons feel a relatively lower density by propagation in the medium; cf. Fig. 4. Then, one should expect larger medium effects for K^- for heavy systems where the baryon density and the size of the fireball are larger. This will be demonstrated in the next section.

VII. COMPARISON WITH EXPERIMENTAL DATA

In this section we compare our results on strangeness production with experimental data from the KaoS, FOPI, and HADES Collaborations at SIS energies and demonstrate the influence of different effects on the observables such as the in-

medium modifications of (anti)kaon properties in terms of the kaon-nuclear potential for kaons and the self-energy within the G-matrix approach for antikaons, as well as scattering effects and the influence of the equation of state.

We compare here two scenarios, with and without medium effects in the following sense.

With medium effects:

(i) For kaons (K^+, K^0) we include a repulsive density-dependent potential which leads to a shift of the kaon mass to a larger value and thus to a shift of the production threshold, which leads to a modification of kaon production and its interaction cross sections; cf. Sec. V C.

(ii) For antikaons (K^-, $\bar{K}^0$) the off-shell dynamics includes the full density and temperature-dependent
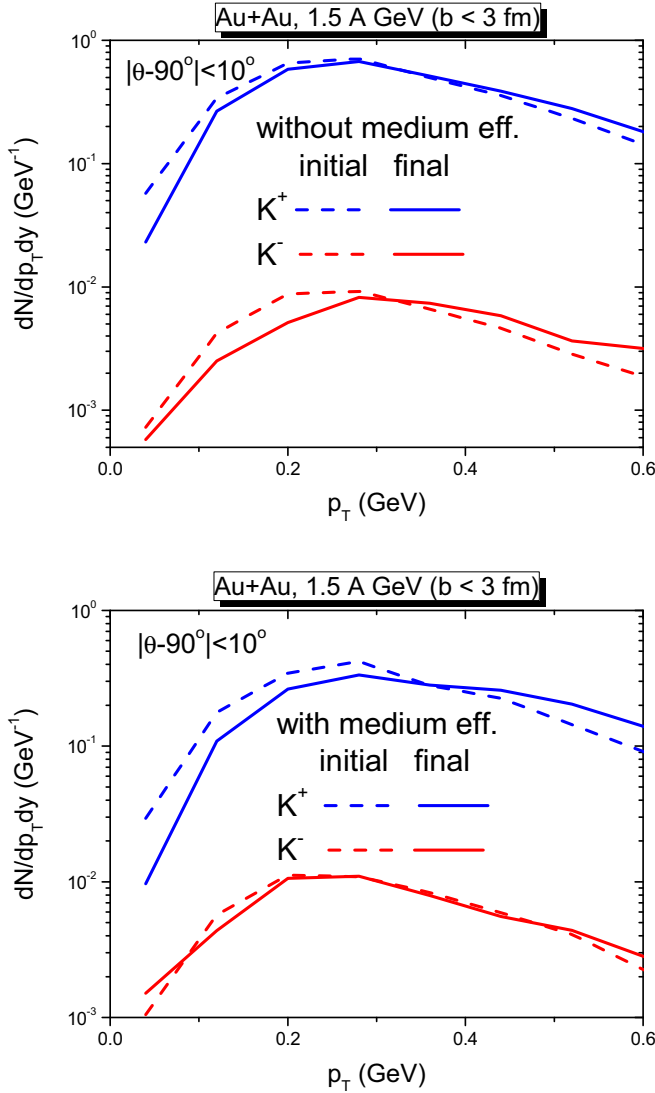
FIG. 9. Comparison of initial (dashed lines) and final (solid lines) p_T spectra of K^+ (upper blue lines) and K^- (lower red lines) mesons without (upper plot) and with (lower plot) in-medium effects (repulsive potential for K^+ and the self-energy within the G-matrix approach for K^-) in central Au+Au collisions ($b < 3$ fm) at 1.5A GeV including the angular cut $|\theta - 90°| < 10°$. Here the number of produced (anti)kaons is normalized to the number of surviving (anti)kaons in each plot.

self-energy within the G-matrix approach: the modification of the antikaon masses in line with the in-medium spectral function, off-shell dispersion relations including complex self-energies, in-medium cross sections for the production and interactions, as well as $\bar{K}$ off-shell propagation; cf. Secs. II, V A, and V B.

Without medium effects:

(i) For kaons (K^+, K^0) we employ on-shell dynamics without a kaon potential and use free cross sections; cf. Sec. IV.

(ii) For antikaons (K^-, $\bar{K}^0$) we employ on-shell dynamics using the free production cross sections in the coupled channels; cf. Secs. II and IV.

Since strangeness is produced always in pairs of $(s, \bar{s})$, the kaon and antikaon (and hyperon) dynamics is coupled. The in-medium effects are applied for kaons and antikaons simultaneously.

A. *y* distributions

Figure 10 shows the rapidity distributions of K^+, K^0, $K^0_s = (K^0 + \bar{K}^0)/2$, and K^- in central Ar+KCl collisions at 1.76A GeV, Ni+Ni collisions at 1.93A GeV, and Au+Au collisions at 1.23A GeV. The dashed lines indicate the results without medium effects for (anti)kaons, while the solid lines denote the results with the medium effects: a repulsive potential for kaons and the self-energy within the G-matrix approach for antikaons. One can see that the kaon potential suppresses K^+, K^0 (or K^0_s) production since it increases the kaon mass in the dense medium and thus increases the threshold for their production. Oppositely, the inclusion of in-medium effects within the G-matrix approach for K^- leads to an enhancement of their production due to a reduction of the threshold in the medium. The latter is caused dominantly by a broadening of the K^- spectral function in the hadronic medium rather than by a shift of the pole mass of the spectral function as discussed in the previous section. As seen from Fig. 10, the rapidity distributions of K^+ and K^0 with potential are broader than those without potential due to the repulsive forces. On the other hand, the rapidity distribution of K^- becomes slightly narrower with the medium effects although the broadening of the antikaon spectral function in the medium leads to the increase in mass for some fraction of antikaons; cf. Fig. 5. The narrowing of the final rapidity distributions occurs due to the following reasons: (i) Due to the attractive nature of the antikaon potential, related to the real part of the antikaon self-energy Re Σ as seen in Fig. 2. (ii) In addition to Re Σ, the imaginary part of the antikaon self-energy Im Σ plays an important role in the off-shell propagation since it enters the equations of motion (35), (36), and (37) and influences the forces. The effect of Im Σ can be illustrated in the following example: let us assume Re $\Sigma \approx 0$, i.e. that the pole mass does not change; then Eq. (36) is approximated by

$$\frac{dp_i}{dt} \approx -\frac{1}{2E} \frac{M^2 - M_0^2}{\mathrm{Im}\, \Sigma} \nabla_r \,\mathrm{Im}\, \Sigma, \qquad (47)$$

where M_0 is the K^- mass in vacuum. Since Im Σ is negative in dense nuclear matter, ∇_r Im Σ is directed outward in heavy-ion collisions. Therefore K^- mesons lighter than M_0 feel an attractive force while heavier K^- mesons feel a repulsive force. As shown in Fig. 5, many more K^- mesons are lighter than M_0 and thus are attracted inwards or to low rapidity.

One can see from Fig. 10 that in-medium effects are necessary to explain the experimental data on the rapidity distributions of K^+, K^0, and K^- mesons in Ni+Ni collisions at 1.93A GeV from the KaoS and FOPI Collaborations as well as K^+, K^0_s, and K^- mesons in Ar+KCl collisions at 1.76A GeV from the HADES Collaboration. However, there is a
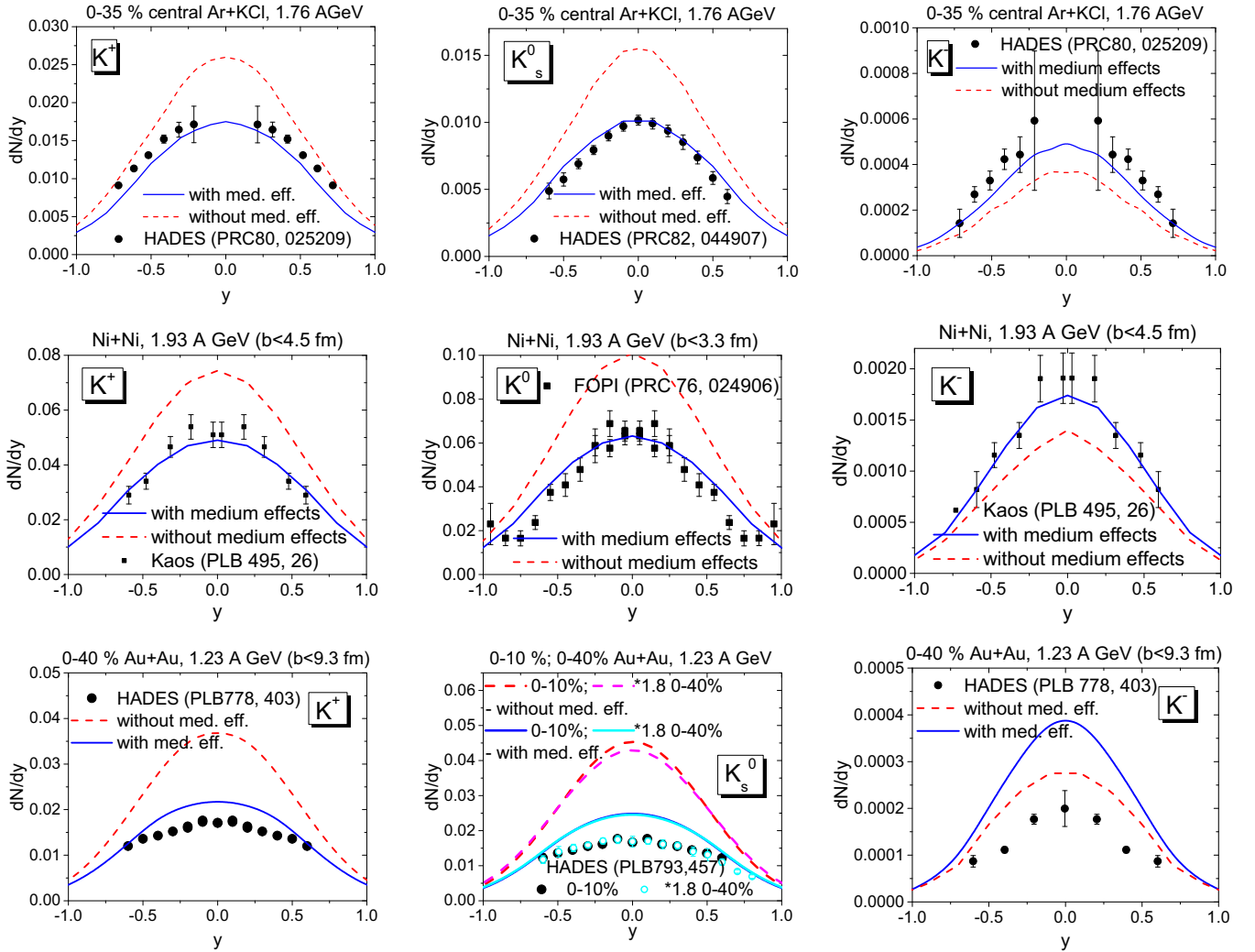
FIG. 10. Upper row: the PHSD results for the rapidity distributions of K^+ (left), K_s^0 (middle), and K^- (right) mesons in 35% central Ar+KCl collisions at 1.76A GeV in comparison to the experimental data of the HADES Collaboration [83,84]. Middle row: the PHSD results for the rapidity distributions of K^+ (left), K^0 (middle), and K^- (right) mesons in central Ni+Ni collisions at 1.93A GeV in comparison to the experimental data of the KaoS Collaboration [4] for K^+, K^- and the FOPI Collaboration [81] for K_s^0. Lower row: the PHSD results for the rapidity distributions of K^+ (left) and K^- (right) mesons in 40% central Au+Au collisions at 1.23A GeV in comparison to experimental data of the HADES Collaboration [82] and of K_s^0 mesons (where $K_s^0 = (K^0 + \bar{K}^0)/2$) (middle) in 10% central and 40% central (scaled by a factor of 1.8) Au+Au collisions at 1.23A GeV in comparison to experimental data of the HADES Collaboration [9]. The dashed lines indicate the PHSD results without medium effects for (anti)kaons, while the solid lines display the results with the medium effects: a repulsive potential for kaons and the self-energy within the G-matrix approach for antikaons.

tension between the PHSD results on K^+, K_s^0, and K^- meson rapidity distributions in Au+Au Collisions at 1.23A GeV and the HADES data (which are slightly lower in energy), without as well as with medium effects. The overestimation for K^+ and K_s^0 (including in-medium effects) is about 20%, while it is about of factor 2 for K^- with medium effects. Thus, within the same model we do not find a consistent description of all three experiments. The origin for this contradictory message from the comparison of our results to the experimental data of the HADES Collaboration and to data of the FOPI and the Kaos Collaborations requires further investigation.

Since strangeness is not present in the initial nuclei, strangeness conservation holds strictly, i.e., the number of strange hadrons is always equal to that of antistrange hadrons.

Therefore the number of produced kaons is the same as that of hyperons and antikaons (the production of multistrange states at low energies is negligible in the total strangeness balance). Thus, the dynamics of hyperons and antikaons is closely linked since the $\pi + Y \to \bar{K} + N$ reaction is the dominant channel for antikaon production. Since the PHSD results for kaon and antikaon rapidity and the p_T spectra for Ni+Ni are in a good agreement with experimental data, we confront our results for the hyperon distribution with the experimental data, too. We recall that in the PHSD the strangeness is strictly conserved.

In the upper part of Fig. 11 we show the rapidity distribution of neutral hyperons $\Lambda + \Sigma^0$ in central Ni+Ni collisions at 1.93A GeV in comparison to the experimental data from
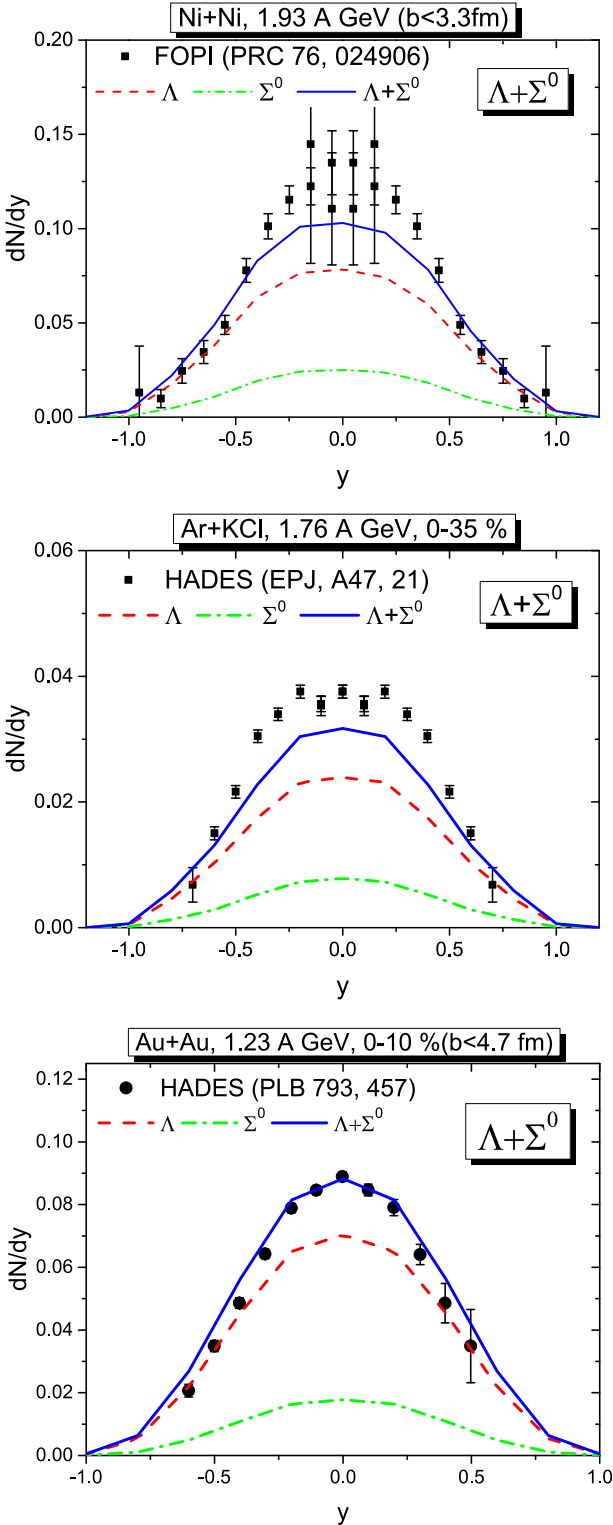
FIG. 11. The PHSD results for the rapidity distributions of neutral hyperons $\Lambda + \Sigma^0$ (blue solid lines) in central (upper) Ni+Ni collisions at 1.93A GeV in comparison to the experimental data from the FOPI Collaboration [81], (middle) in central Ar+KCl collisions at 1.76 GeV and (lower) in central Au+Au collisions at 1.5 GeV in comparison to the experimental data from the HADES Collaboration [8,9]. The red dashed lines show the contribution from Λ and the green dot-dashed lines represent the contribution from Σ hyperons.

the FOPI Collaboration [81]. A small deviation is seen at midrapidity where our results underestimate the FOPI data, and the theoretical distribution is slightly broader than the data. A similar disagreement is found in the middle part of Fig. 11 which shows the comparison with the experimental data from the HADES Collaboration [8] in central Ar+KCl collisions at 1.76A GeV. However, the PHSD result for the y distribution of $\Lambda + \Sigma^0$ agrees very well with the HADES data for Au+Au collisions at 1.23A GeV as seen from the lower part of Fig. 11.

B. p_T distributions

We note that the rapidity distributions are not measured directly in the experiments. They are extrapolated from the measured p_T spectra assuming a thermal distribution. In this respect it is very important to compare the model results with directly measured quantities such as p_T distributions, which we present in this subsection.

Figure 12 shows the PHSD results for the m_T spectra versus the transverse kinetic energy $m_T - m_K$ of K^+ and K^- at midrapidity in central Ni+Ni collisions at 1.93A GeV in comparison to the experimental data of the KaoS Collaboration [4]. We note that here the invariant p_T spectra are divided by transverse mass m_T to extract the effective temperature, which will be discussed later in this section; therefore the spectra are not Lorentz invariant. As for the rapidity distribution the kaon-nuclear potential suppresses the K^+ yield and pushes the K^+ spectrum to larger transverse momenta. On the other hand, the antikaon potential enhances the K^- yield and pulls the p_T spectrum toward smaller transverse momenta. Again the kaon potential is necessary to reproduce the experimental data on the p_T spectra of K^+; the data for K^- are also in favor of the inclusion of the self-energy within the G-matrix approach, similar to their yields and rapidity distributions, but, as discussed in the last section, scattering of antikaons in the medium and the in-medium effect within the G-matrix for antikaons partially compensate each other.

In Fig. 13 we show the PHSD results (including in-medium effects) for the m_T spectra of K^+ (upper), K_S^0 (middle), and K^- (lower) as a function of the transverse kinetic energy $m_T - m_K$ for different rapidity bins in 35% central Ar+KCl collisions at 1.76A GeV in comparison to the experimental data of the HADES Collaboration [83,84]. One can see that the PHSD agrees with HADES data for Ar+KCl very well for all rapidity bins.

Now we advance to a heavy system and show in Fig. 14 the PHSD results for the midrapidity m_T spectra of K^+ (blue line) and K^- (green line) as a function of the transverse kinetic energy $m_T - m_K$ in 40% central Au+Au collisions at 1.23A GeV in comparison to the HADES data [82]. The HADES data for K^+ are overestimated by about 20–30% at large m_T and agree with the data at small m_T for the in-medium scenario (solid blue line). Without medium effects (dashed blue line) we overpredict the data by a factor of 2. The discrepancies for the K^- with medium effects are about factor of 2 at low m_T (solid green line) and about 30% (within statistical fluctuations) at larger m_T for the free scenario (dashed green line).
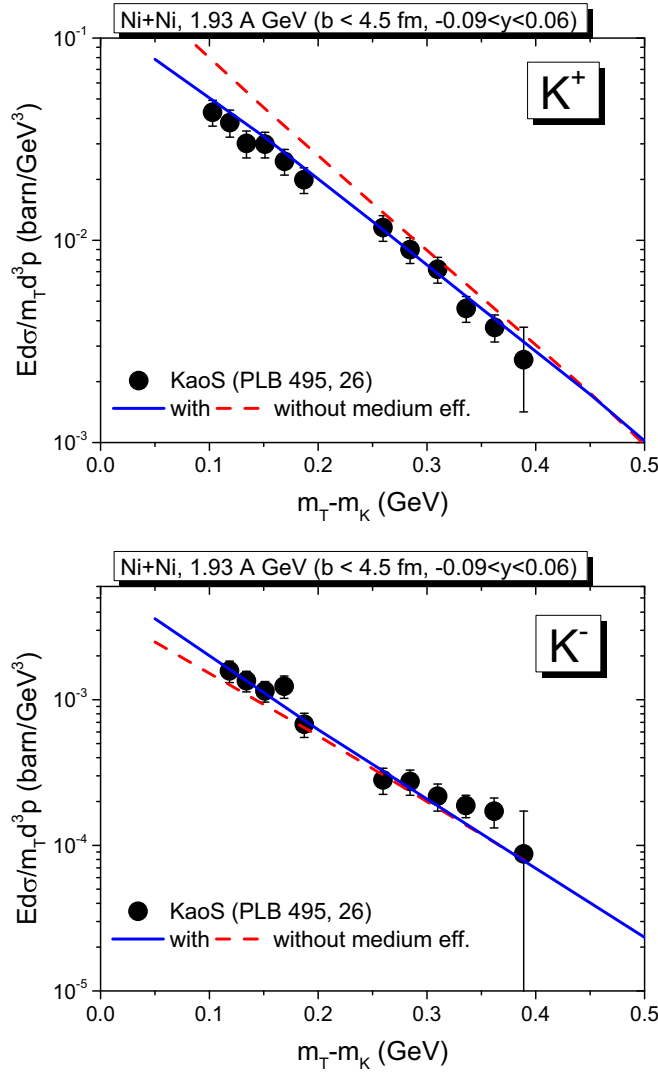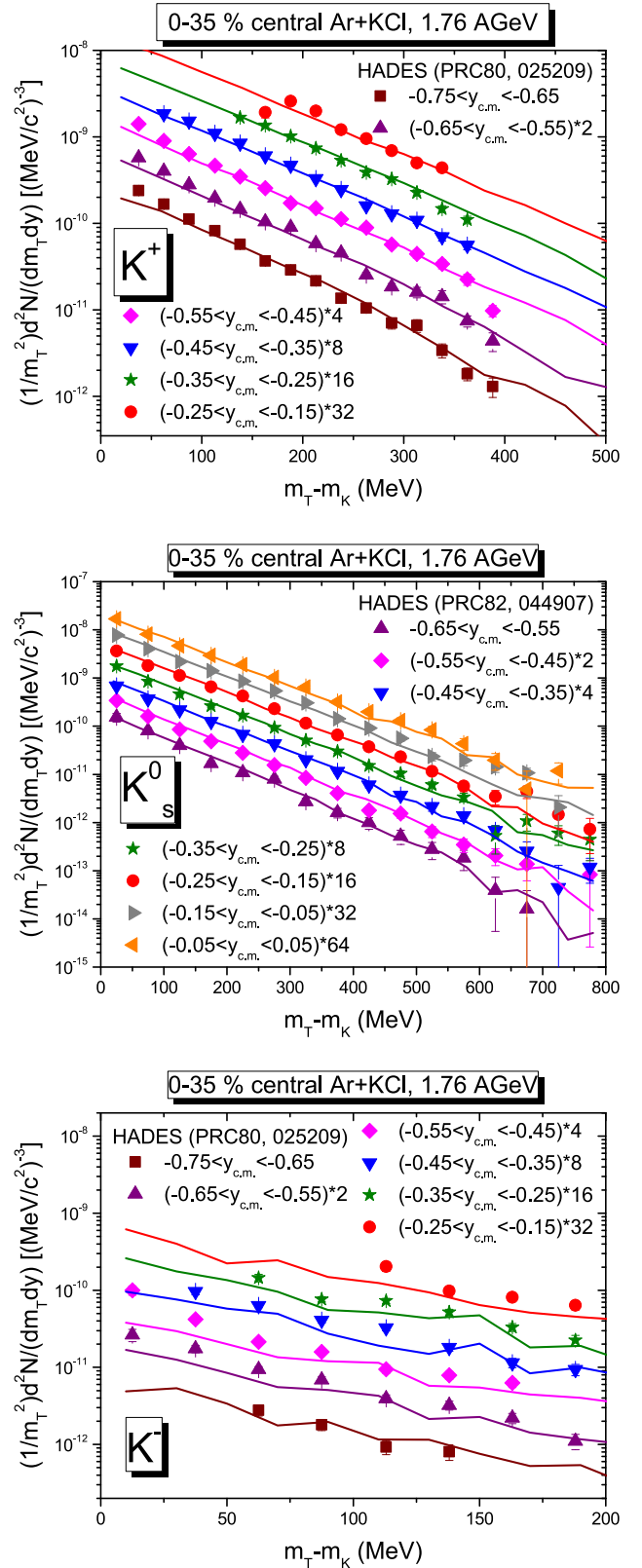
FIG. 12. The PHSD results for the m_T spectra of K^+ (upper) and K^- (lower) as a function of the transverse kinetic energy $m_T - m_K$ in central Ni+Ni collisions at 1.93A GeV in comparison to the experimental data of the KaoS Collaboration [4]. The dashed lines indicate the results without medium effects for (anti)kaons, while the solid lines display the results with the medium effects: a repulsive potential for kaons and the self-energy within the G-matrix approach for antikaons.

It is interesting to compare our results for the m_T distributions not only to the midrapidity data as shown in Fig. 14, but also to the noncentral rapidity bins which have been used for the extrapolation of the HADES results for dN/dy shown in Fig. 10. In Fig. 15 we display the PHSD m_T spectra of K^+ (upper) and K^- (lower) (including in-medium effects) for different rapidity bins in 40% central Au+Au collisions at 1.23A GeV in comparison to the experimental data of the HADES Collaboration [82]. As one can see, the slope of the m_T spectra of K^+ is getting harder when coming to midrapidity. The m_T spectra of K^+ for rapidity bins $|y| > 0.45$ are very well described; however, the agreement is getting worse (up to 30% overestimation for large m_T) when coming to the midrapidity

FIG. 13. The PHSD results (including in-medium effects) for the m_T spectra of K^+ (upper), K_S^0 (middle), and K^- (lower) as a function of the transverse kinetic energy $m_T - m_K$ for different rapidity bins in 35% central Ar+KCl collisions at 1.76A GeV in comparison to the experimental data of the HADES Collaboration [83,84].
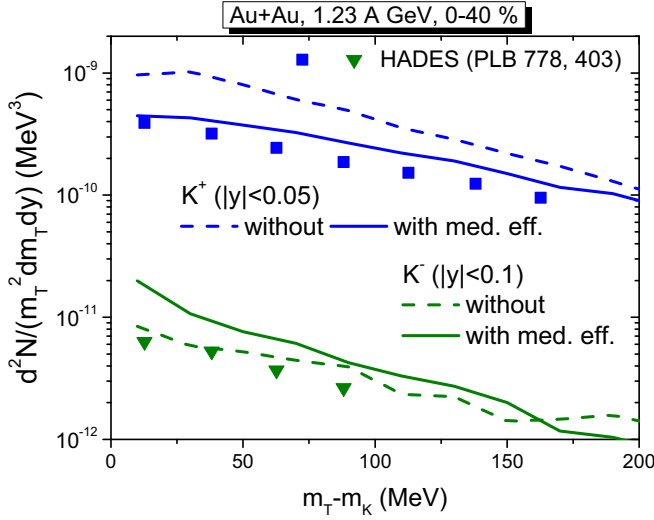
FIG. 14. The PHSD results for the midrapidity m_T spectra of K^+ (blue line) and K^- (green line) as a function of the transverse kinetic energy $m_T - m_K$ in 40% central Au+Au collisions at 1.23A GeV in comparison to the experimental data of the HADES Collaboration [82]. The dashed lines indicate the results without medium effects for (anti)kaons, while the solid lines display the results with the medium effects: a repulsive potential for kaons and the self-energy within the G-matrix approach for antikaons.

bin, as discussed above for Fig. 14. For K^- mesons the slopes of the m_T spectra for each y bin are approximately in line with the HADES data; however, the absolute yield for each y bin is overestimated by about of a factor of 2. This is reflected in the y distribution of K^+ and K^- of Fig. 10, too.

Figure 16 shows the inclusive invariant cross sections at midrapidity as a function of the kinetic energy $E_{\text{c.m.}} - m_K$ for K^+ and K^- mesons in minimum-bias Au+Au collisions at 1.5A GeV, Ni+Ni collisions at 1.93A GeV, and C+C collisions at 1.8A GeV with and without medium effects, which are compared to the experimental data from the KaoS Collaboration [85]. In contrast to the kaon p_T spectra in central Ni+Ni collisions (shown in Fig. 12), the yields of K^+ mesons in minimum bias are slightly underestimated as compared to the experimental data, which implies that our K^+ production in noncentral collisions is smaller than in the experimental data. However, the slopes of the K^+ spectra are close to the experimental data with the kaon potential switched on. As seen from Fig. 12, the repulsive force from the kaon potential hardens the spectra relative to those without kaon potential. The effects of the kaon potential are stronger in Au+Au collisions than in C+C collisions, since the baryon density achieved in Au+Au collisions is higher than in C+C collisions.

The same applies for the K^- mesons (right panel of Fig. 16): the maximal softening of the p_T spectrum of K^- occurs in Au+Au collisions. The softening of the p_T spectrum is also very visible in minimum-bias Ni+Ni collisions,;however, the effect is smaller than in central Ni+Ni collisions in Fig. 12, since the baryon density is larger for central collisions than in minimum-bias Ni+Ni collisions. For C+C collisions the softening is invisible (with the statistics achieved in the
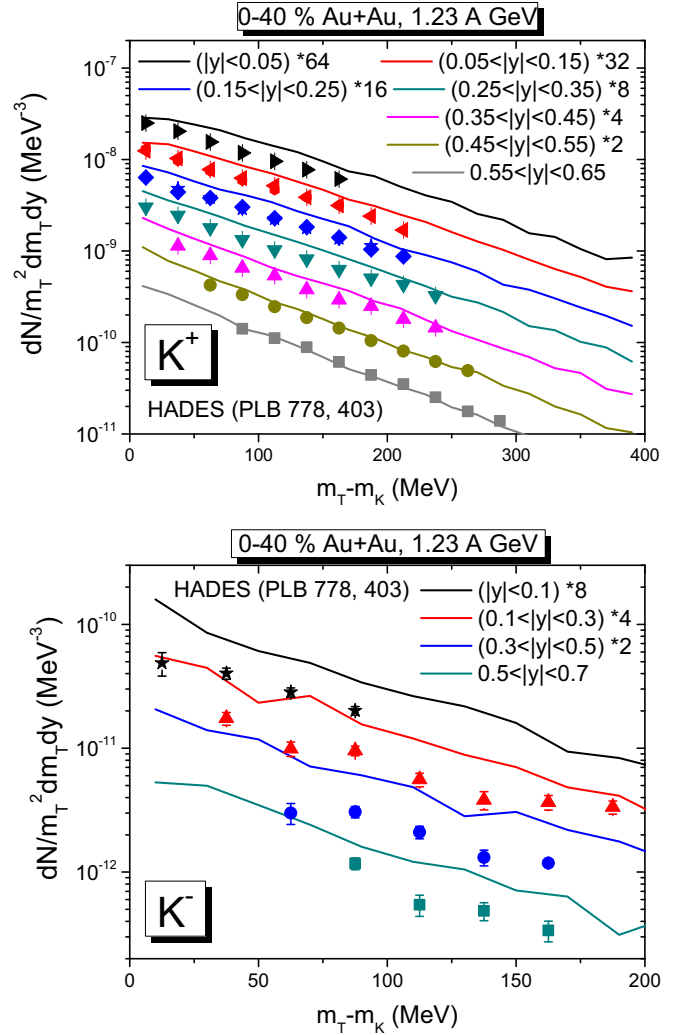

FIG. 15. The PHSD results (including in-medium effects) for the m_T spectra of K^+ (upper) and K^- (lower) as a function of the transverse kinetic energy $m_T - m_K$ for different rapidity bins in 40% central Au+Au collisions at 1.23A GeV in comparison to the experimental data of the HADES Collaboration [82].

calculations); moreover, the absolute yield is underestimated for C+C even with the inclusion of in-medium effects.

Additionally, in Fig. 17 we show the inclusive invariant cross section at midrapidity as a function of the kinetic energy $E_{\text{c.m.}} - m_K$ for the K^+ mesons in minimum-bias Au+Au collisions at strongly subthreshold energy of 1.0A GeV without (red dashed line) and with (blue solid line) medium effects compared to the experimental data from the KaoS Collaboration [85]. One can see that the PHSD describes the K^+ spectra very well with in-medium effects and substantially overestimates the data without the repulsive potential.

The transverse momentum spectra can be characterized by an effective temperature T_{eff} which can be obtained from a fit of the (anti)kaon spectra with a thermal distribution function:

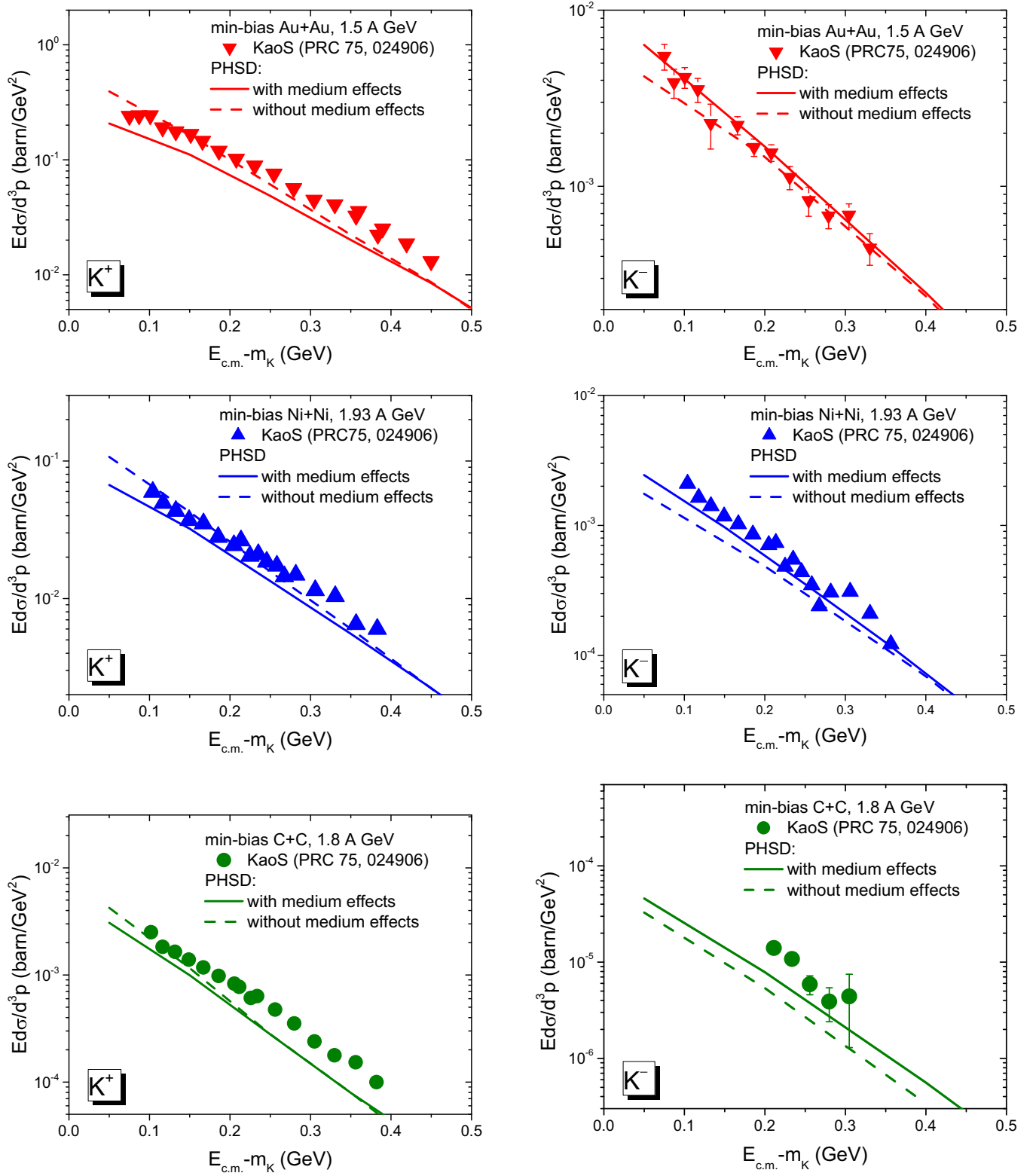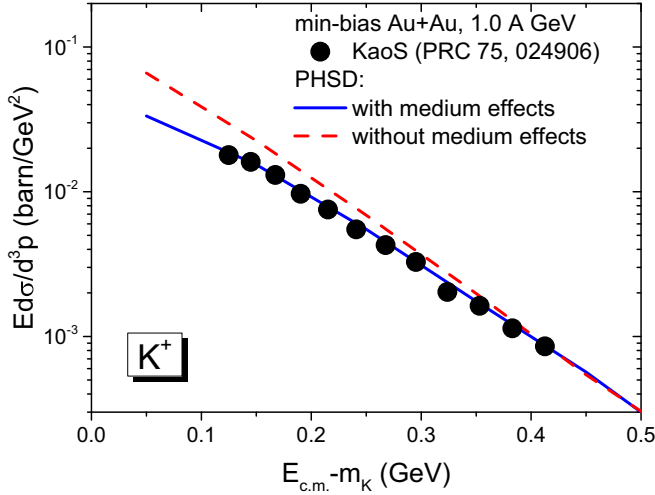$$E \frac{d\sigma}{d^3 p} \sim E \exp\left(-\frac{E}{T} \right). \qquad (48)$$

FIG. 16. The PHSD results for the inclusive invariant cross sections at midrapidity as a function of the kinetic energy $E_{\text{c.m.}} - m_K$ for K^+ (left) and K^- (right) mesons in minimum-bias Au+Au collisions at 1.5A GeV (upper), Ni+Ni collisions at 1.93A GeV, (middle) and C+C collisions at 1.8A GeV (lower) with (solid lines) and without (dashed lines) medium effects, compared to the experimental data from the KaoS Collaboration [85]. The midrapidity condition is a selection of $\theta_{\text{c.m.}} = 90° \pm 10°$.

FIG. 17. The PHSD results for the inclusive invariant cross section at midrapidity as a function of the kinetic energy $E_{\text{c.m.}} - m_K$ for K^+ mesons in minimum-bias Au+Au collisions at $1.0A$ GeV without (red dashed line) and with (blue solid line) medium effects compared to the experimental data from the KaoS Collaboration [85]. The midrapidity condition is a selection of $\theta_{\text{c.m.}} = 90° \pm 10°$.

Since radial flow, which hardens the spectrum, contributes to the slope, T is called an effective temperature T_{eff}. Figure 18 shows the effective temperatures for K^+ and K^- mesons in minimum-bias C+C at energies of $1.5A$ and $1.8A$ GeV, and in Ni+Ni and Au+Au collisions, respectively, at energies of $1.93A$ and $1.5A$ GeV as a function of the mass number of target and projectile nuclei. The effective temperature depends on the range of transverse momenta considered and our
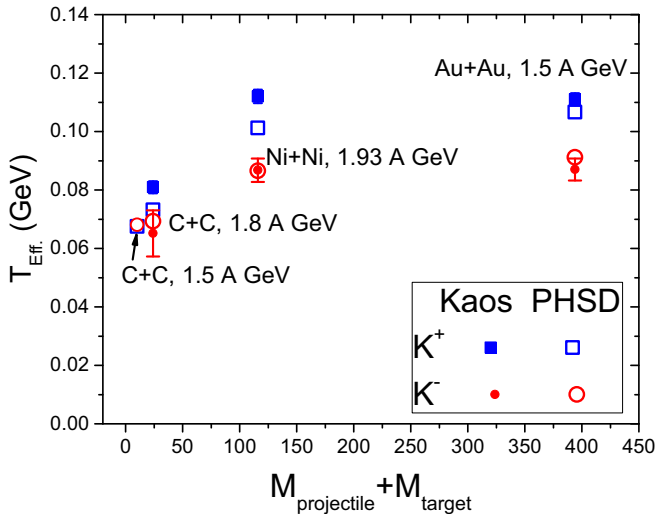
FIG. 18. The PHSD results for the effective temperatures (or the inverse slopes) of K^+ and K^- mesons as a function of the mass number of projectile and target nuclei in minimum-bias collisions of C+C at $1.5A$ and $1.8A$ GeV, Ni+Ni at $1.93A$ GeV, and Au+Au at $1.5A$ GeV in comparison to the experimental data from the KaoS Collaboration [85]. We shift the PHSD results for C+C at $1.5A$ GeV to a lower mass number for better visibility.

results are fitted to the spectra in the range $0 < E - m_K < 0.5$ GeV. Because of collective flow the effective temperature in Au+Au collisions is higher than that in C+C collisions, although the collision energy is higher in the latter case.

One can see that the effective temperature for K^+ mesons is higher than for K^- mesons, because the kaon potential—which generates a repulsive force—hardens the K^+ spectra, while the inclusion of the self-energy within the G-matrix approach softens the K^- spectra. This effect is stronger for the heavy systems: the splitting of the effective temperatures for K^+ and K^- is small in C+C collisions, where the size and density of nuclear matter is small, and the splitting is larger for Au+Au collisions which produce a much larger and denser fireball. Moreover, the larger density achieved in Au+Au collisions compared to C+C collisions leads to the relative increase of the T_{eff} of K^+ and K^- with system size. Our results are close to the experimental data of the KaoS Collaboration [85] and are qualitatively consistent.

The difference of the effective temperatures of (anti)kaons for C+C and Au+Au at $1.5A$ GeV is mostly attributed to in-medium effects. As demonstrated in Fig. 9 (upper plot), the elastic scattering increases the effective temperature for both kaons and antikaons considerably [since the (anti)kaons are produced near the thresholds, they are not energetic due to phase space limitation]. The interaction with the medium is repulsive for kaons and mostly attractive for antikaons, and this leads to the separation of their effective temperatures in the Au+Au reaction. Such separation is not visible for the light C+C system due to the small volume of the medium and lower baryon densities.

We note that the different slopes of the K^+ and K^- m_T spectra for Au+Au collisions at $1.23A$ GeV have been interpreted by HADES Collaboration [82,83] by the feed-down from ϕ-meson decay, which substantially softens the spectra of K^- mesons compared to the "thermal" hard component; cf. Fig. 2 in Ref. [82]. However, according to the present PHSD calculations, the contribution to the K^- abundances for Au+Au collisions at 1.5 GeV from the ϕ decay plays a subleading role (cf. Fig. 7) and the different slopes of K^+ and K^- are attributed to the in-medium effects (as discussed above). This result is in line with the experimental data of the KaoS Collaboration which show that the splitting T_{eff} of K^+ and K^- spectra increases with the system size. One can emphasize that if the antikaons are dominantly produced by ϕ decay one would expect a different behavior: since the ϕ-nucleon interaction cross section is small (cf. Ref. [86]) and the ϕ-meson lifetime is long, i.e., most of the ϕ mesons decay to $K\bar{K}$ outside of the fireball at almost zero baryon density, one would expect that the slopes of the spectra of antikaons do not show the prominent dependence on the system size. Thus, we stress that by a measurement of the effective temperature of K^- for different system sizes for the same beam energy one can shed more light on the origin of the antikaon production and the role of the in-medium effects.

We note that our results for the rapidity and p_T spectra are consistent with previous findings within the HSD [16–19] and other groups [24,25] about the necessity to include medium effects for the proper description of the experimental data on strangeness production at low energies.
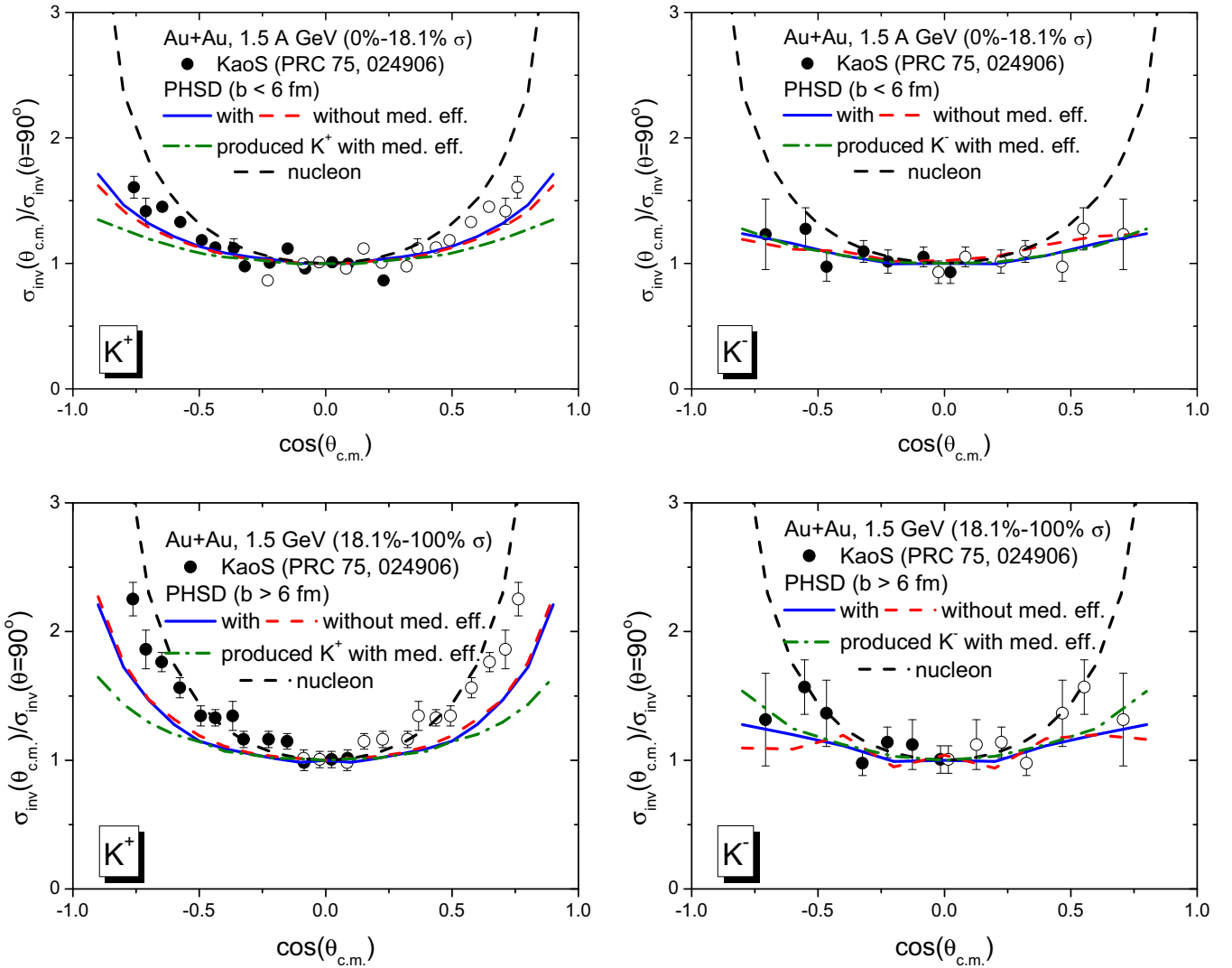
FIG. 19. The polar angular distributions of K^+ (left) and K^- (right) mesons in central (upper) and noncentral (lower) Au+Au collisions at 1.5A GeV compared to the experimental data from the KaoS Collaboration [85]. The distributions are normalized to unity at $\cos(\theta_{\text{c.m.}}) = 0$, i.e., presented as the ratios $\sigma_{\text{inv}}(\theta_{\text{c.m.}})/\sigma_{\text{inv}}(\theta_{\text{c.m.}} = 90°)$. The solid blue and dashed red lines show the (anti)kaon angular distributions with and without the medium effects, respectively. The dot-dashed green lines show their distribution at the production point (with medium effects). The black dashed lines indicate the nucleon angular distributions.

We stress again that the comparison to the HADES data on m_T spectra for Au+Au collisions at 1.23A GeV falls out of this systematics, although the PHSD results with in-medium effects (as well as the results of other transport models [24,25]) agree well with the KaoS and FOPI data even for Au+Au collisions at 1.0A and 1.5A GeV. Moreover, the PHSD reproduces well the KaoS and FOPI data for a lighter system such as Ni+Ni at 1.93A GeV and the HADES data for Ar+KCl at 1.76A GeV. This tension is presently unsolved and requires further investigations from theoretical and experimental sides.

In this respect, we note that in the present calculation the *s* wave and *p* wave of the antikaon-nucleon interaction have been obtained from the leading-order contribution together with the Λ, Σ, and Σ^* pole terms. In order to improve the agreement with data for large momenta, future work should include the analysis of the effect of next-to-leading-order

corrections to the antikaon-nucleon interaction as well as the inclusion of strange baryonic resonances located at energies between 1.89 and 2.35 GeV, well above the antikaon-nucleon threshold, as recently discussed in Ref. [87].

C. Polar distributions

Figure 19 shows the polar angle distributions of K^+ and K^- in central [upper row: (0–18.1)% of total reaction cross section σ] and in noncentral [lower row: (18.1–100)% $\times \sigma$] Au+Au collisions at 1.5A GeV in comparison to the experimental data from the KaoS Collaboration [85]. The polar angle is defined as the angle between the beam axis and the particle, i.e., $\cos(\theta_{\text{c.m.}}) = \pm 1$ corresponds to the beam direction and $\cos(\theta_{\text{c.m.}}) = 0$ to midrapidity. The distributions are normalized to unity at $\cos(\theta_{\text{c.m.}}) = 0$, i.e., presented as the ratios $\sigma_{\text{inv}}(\theta_{\text{c.m.}})/\sigma_{\text{inv}}(\theta_{\text{c.m.}} = 90°)$, where $\sigma_{\text{inv}}(\theta_{\text{c.m.}})$ is the
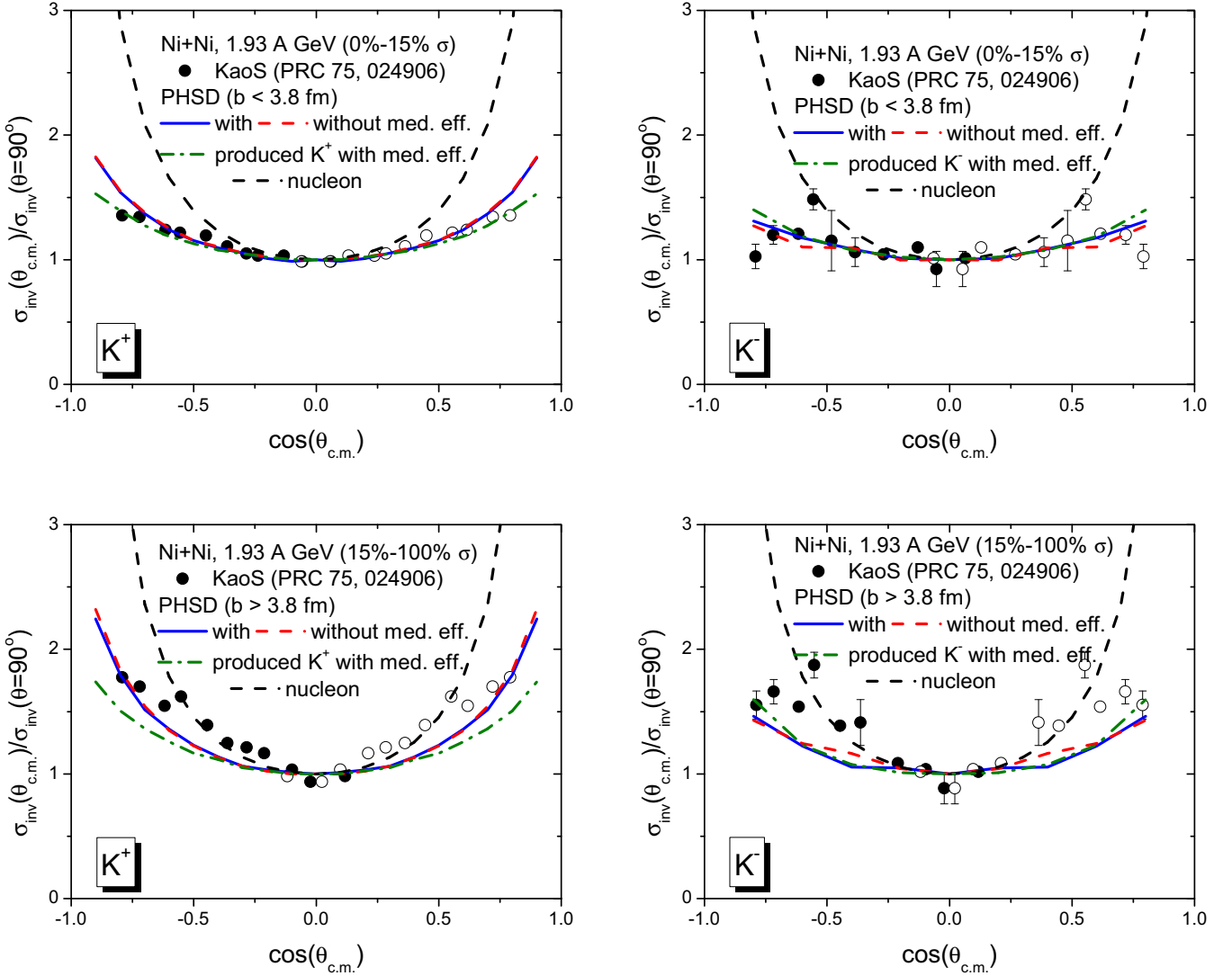
FIG. 20. The polar angle distributions of K^+ (left) and K^- (right) mesons in central (upper) and noncentral (lower) Ni+Ni collisions at 1.93A GeV compared to the experimental data from the KaoS Collaboration [85]. The line description is the same as in Fig. 19.

invariant particle production cross section measured at a polar angle $\theta_{c.m.}$.

As seen from Fig. 19, the polar distribution of K^+ mesons in noncentral collisions is strongly peaked in the beam direction, while the distribution in central collisions is rather flat. This results from a strong correlation of K^+ mesons with nucleons through the production of K^+ from nucleon+nucleon or nucleon+pion scattering and the interactions of K^+ mesons with nucleons. One can see that the polar distribution of K^+ follows that of nucleons which is shown by black dashed lines both in central and noncentral Au+Au collisions.

The dot-dashed green lines display the polar distributions of produced K^+. We note that the distribution of produced K^+ is only slightly affected when including the kaon potential. For central collisions the angular distribution of kaons is also rather flat, while for noncentral it grows towards beam direction. The differences between the dot-dashed green line and the dashed red line are caused by scattering and those between the dashed red line and the blue solid line are the effect of the

kaon potential. Since the kaon potential is repulsive, it pushes the polar distributions of K^+ mesons towards forward and backward directions. One can see that the effects of scattering on the polar distribution of K^+ mesons are stronger than those of the kaon potential.

The right two panels of Fig. 19 show the polar distributions of K^- mesons in central and noncentral Au+Au collisions, respectively. Though the statistics is limited in noncentral collisions, one can see that the scattering pushes K^- mesons backward and forward as in the case of K^+. However, the effects of the antikaon potential are opposite such that it pulls K^- mesons into the middle of the fireball, since the antikaon feels attraction.

In Fig. 20 we show the same polar distributions for Ni+Ni collisions at 1.93A GeV. One can see a rather similar behavior of K^+ and K^- polar distributions as for Au+Au at 1.5A GeV, although the effects of scattering and the potential are slightly weaker than in Au+Au collisions since the size and density of the produced fireball is smaller.

The minor influence of the in-medium effects on the polar distribution for Ni+Ni and Au+Au collisions might seem to be in conflict with the enhancement of the K^+ rapidity distribution shown in Fig. 10. However, both results are consistent due to the following reasons: one has to keep in mind that the polar distribution is normalized to $\sigma_{\text{inv}}(\theta = 90°)$, i.e., at $\cos\theta_{\text{c.m.}} = 0$. For kaons with a moderate transverse momentum in the range of $0.2 < p_T < 0.8$ GeV (to which most kaons belong), the rapidity $y = 0.5$ corresponds to $0.8 < \cos\theta_{\text{c.m.}} < 0.9$. Therefore, a wide range of $\cos\theta_{\text{c.m.}}$ in Fig. 20 corresponds to a narrow range close to midrapidity in Fig. 10. If dN/dy with and without medium effects would be rescaled (i.e., assuming the same number of kaon production with and without medium effects), the shapes of the y distributions near midrapidity ($-0.5 < y < 0.5$) would be similar to each other. That is why the polar distributions with and without medium effects are similar to each other in Figs. 19 and 20, too.

D. Azimuthal distributions

The azimuthal distribution of particles is parametrized in a Fourier series as

$$\frac{dN(p_T, y)}{d\phi} = C[1 + 2v_1(p_T, y)\cos\phi$$
$$+ 2v_2(p_T, y)\cos(2\phi) + \cdots], \qquad (49)$$

where the coefficients v_1 and v_2 are, respectively, denoted as the directed and elliptic flows obtained by

$$v_1(p_T, y) = \frac{\int d\phi \frac{dN(p_T, y)}{d\phi}\cos\phi}{\int d\phi \frac{dN(p_T, y)}{d\phi}}, \qquad (50)$$

$$v_2(p_T, y) = \frac{\int d\phi \frac{dN(p_T, y)}{d\phi}\cos(2\phi)}{\int d\phi \frac{dN(p_T, y)}{d\phi}}. \qquad (51)$$

Since the collective flow of kaons is related to the flow of nucleons involved in the production and interactions of kaons, we first show in Fig. 21 (upper plot) the directed flows of protons and Λ's (which are the associated partner for the kaon production) as a function of the normalized rapidity in central Ni+Ni collisions at $1.93A$ GeV. In our initialization of $A + A$ collisions, the projectile nucleus moving in the z direction is located at $x = b/2$ and the target nucleus at $x = -b/2$, where b is the impact parameter. One can see that the average p_x of the protons and Λ's is antisymmetric with respect to $y = 0$ and shows a linear increase with rapidity in line with the FOPI data.

The middle panel of Fig. 21 shows the directed flow v_1 of K^+ mesons as a function of p_T in central Ni+Ni collisions at the same energy. Considering $y_{\text{lab}}/y_{\text{c.m.}} - 1 = (y/y_{\text{beam}})_{\text{c.m.}}$, where $y_{\text{c.m.}}$ is the c.m. rapidity of two colliding heavy ions, the directed flow of nucleons within $-1.2 < (y/y_{\text{beam}})_{\text{c.m.}} < -0.65$ is negative as seen from the upper panel of Fig. 21. In fact, the directed flow v_1 of the produced K^+ mesons—which is shown by the dotted line—is negative, since they are produced by the scattering of nucleons. The dashed line represents the v_1 of K^+ mesons after freeze-out ("survived") without kaon potential. The v_1 of K^+ mesons is only slightly changed due to the interaction with nucleons which have a
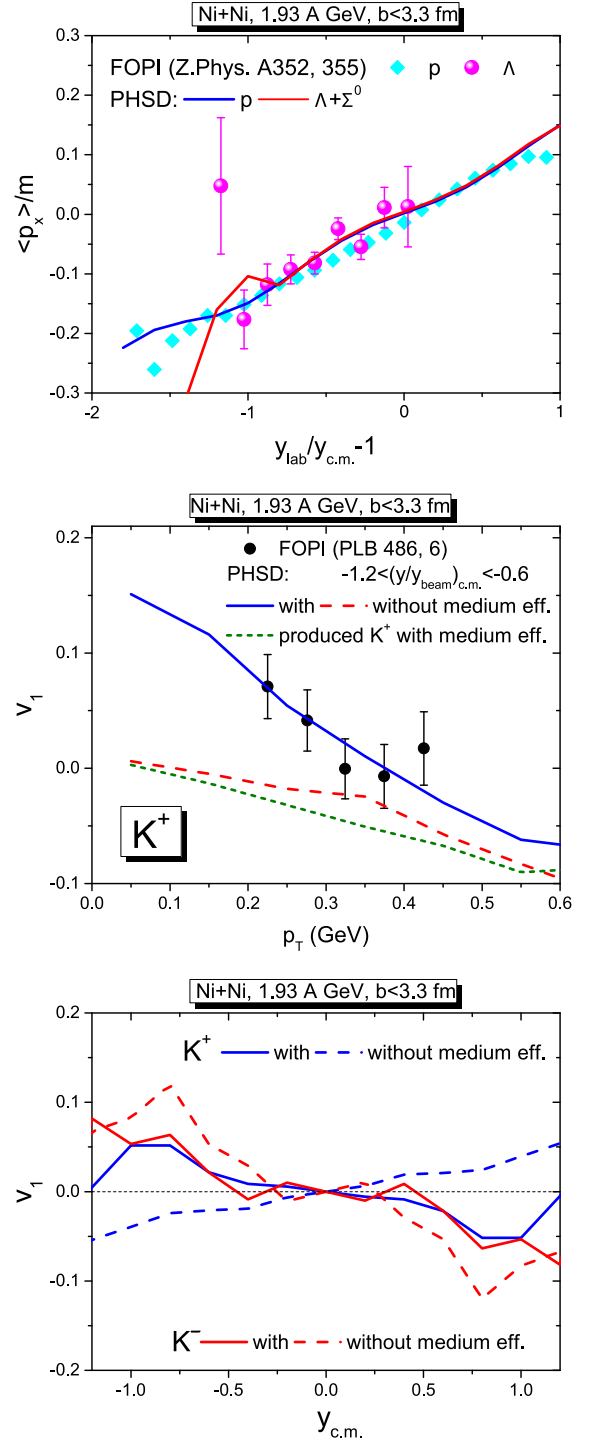

FIG. 21. Upper: The $\langle p_x \rangle/m$ of Λ (red solid line) and proton (blue solid line) as a function of normalized rapidity and (middle) the v_1 of K^+ mesons as a function of p_T in central Ni+Ni collisions at $1.93A$ GeV in comparison to the experimental data from the FOPI Collaboration [88,89]. Lower: The v_1 of K^+ and K^- with and without medium effects as a function of rapidity in the same collisions. The blue solid line in the lower plot shows the PHSD results for the v_1 of final K^+ mesons with medium effects, the green dotted line indicates the v_1 of kaons at the production point for the in-medium scenario, while the red dashed line shows the v_1 of kaons without medium effects.

FIG. 23. The integrated v_2 of K^+ (blue lines) and K^- (red lines) as a function of time with (solid lines) and without (dashed lines) medium effects in the same collisions as in Fig. 22. The green dot-dashed line corresponds to the v_2 of nucleons.
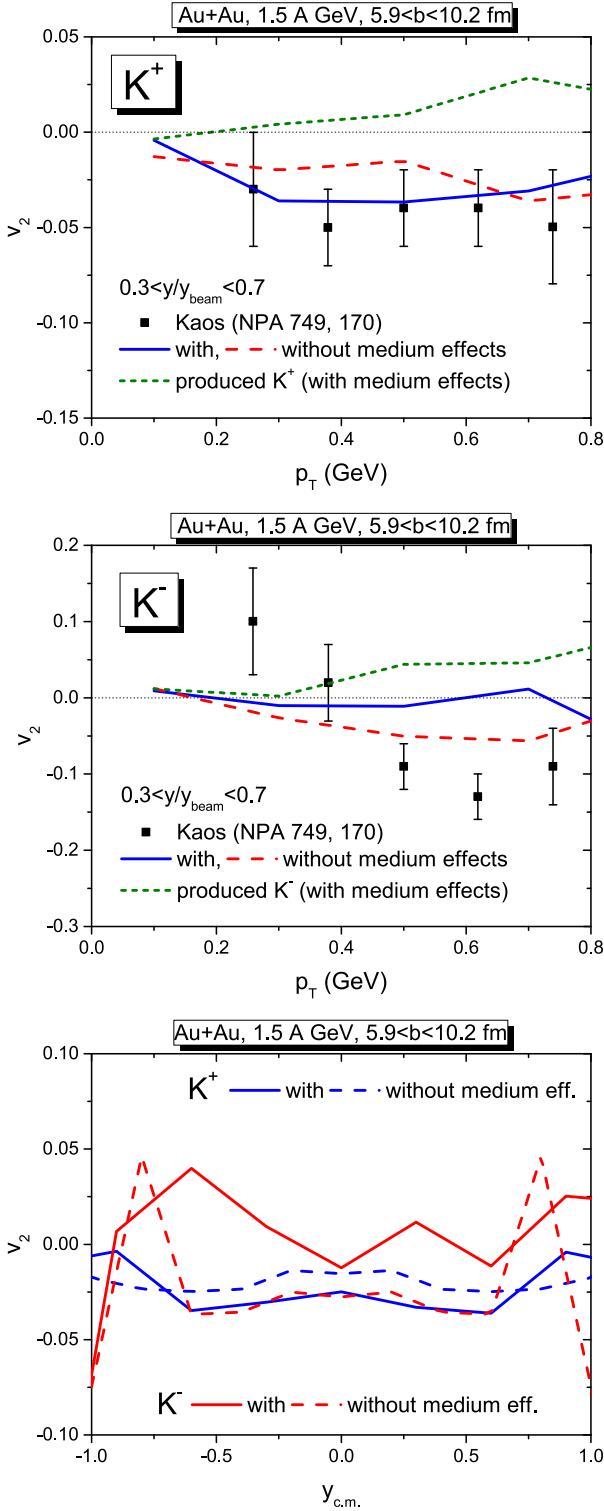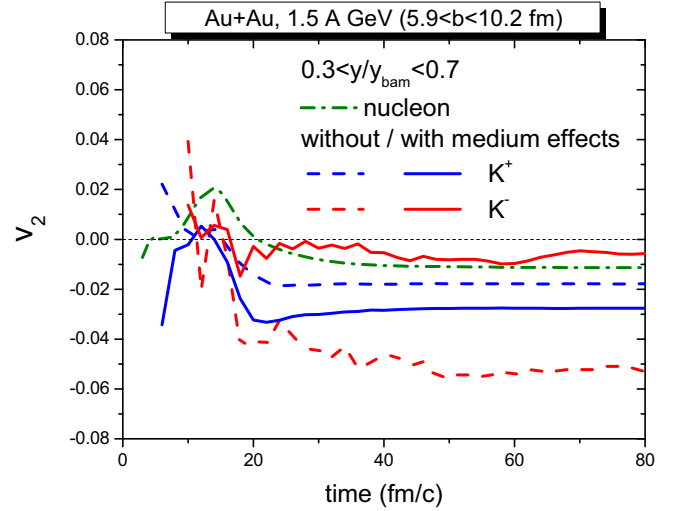

FIG. 22. Upper and middle plots: The flow coefficient v_2 of K^+ (upper) and K^- (middle) mesons as a function of p_T in semicentral Au+Au collisions at 1.5A GeV in comparison to the experimental data from the KaoS Collaboration [90]. The solid blue and dashed red solid lines show the v_2 with and without medium effects, respectively, while the green dotted lines represent v_2 at the production point for the in-medium scenario. Lower plot: The v_2 of K^+ and K^- with and without medium effects as a function of rapidity in the same collisions.

negative v_1. Including the kaon potential, however, the v_1 of K^+ drastically changes and becomes positive. This happens because the nucleons from the target nucleus, which are dominantly located in the $-x$ direction, push the K^+ in $+x$ direction. Similar phenomena occur at forward rapidity, where the nucleons from the projectile nucleus push the K^+ in $-x$ direction. The effects of the kaon potential are stronger for K^+ mesons with small transverse momentum and weaker for those with large transverse momentum, since it is harder to change the direction of K^+ mesons which have large momentum. One can see that the experimental data are well explained if one includes the kaon-nuclear potential in the calculations. The lower panel shows the v_1 of K^+ and K^- as a function of rapidity. It demonstrates more clearly the effect of the (anti)kaon potential on the directed flow. As explained above the repulsive kaon potential pushes the directed flow of K^+ away from that of nucleons while the attractive antikaon potential pulls the directed flow of K^- closer.

Figure 22 shows the elliptic flow v_2 of K^+ (upper plot) and K^- (middle plot) mesons as a function of p_T and v_2 of K^+ and K^- as a function of rapidity y (lower plot) in semicentral Au+Au collisions at 1.5A GeV in comparison to the experimental data from the KaoS Collaboration [90]. Since $0.3 < y/y_{beam} < 0.7$ is equivalent to $-0.2 < (y/y_{beam})_{c.m.} < 0.2$, the shown (in the upper and middle plots) v_2 corresponds to midrapidity. For a better understanding of the results we display in Fig. 23 the integrated v_2 of K^+, K^- mesons and also nucleons as a function of time in the same rapidity range as well as the same collision system. The dotted lines in the upper and middle panels are, respectively, the v_2 of produced K^+ and K^- mesons. Since (anti)kaons are produced through the scattering of nucleons with other nucleons or mesons, their v_2 is closely related to the v_2 of nucleons. Considering that the baryon density is peaked around $t = 10$ fm/c for this centrality/energy and that most of the K^+ and K^- mesons are produced before $t = 15$ fm/c, one can find that the v_2

of nucleons at the production time of (anti)kaons is positive. This explains the positive v_2 of the produced K^+ and K^- mesons. After that the v_2 of nucleons decreases and changes sign due to the attractive nuclear potential. Since the produced K^+ and K^- interact with the nucleons, their v_2 follows the v_2 of nucleons as shown by the blue and red dashed lines in the lower panel, which, respectively, indicate the v_2 of K^+ and of K^- mesons with scattering turned on, but (anti)kaon-nuclear potential turned off. As a result, the final v_2 of K^+ and of K^- without the potential turn out negative as seen from the upper and middle panels of Fig. 22. This is also clearly seen in the lower panel of Fig. 22, which shows that v_2 of K^+ and K^- without medium effects is negative. An inclusion of the repulsive kaon potential leads to a further reduction of the K^+ elliptic flow, while the in-medium effects for K^- lead to an enhancement of v_2, which fluctuates around zero with the presently achieved numerical statistics.

The difference between the dashed line and solid line shows the effects of the (anti)kaon-nuclear potential on the v_2 of K^+ and K^- mesons. One can see that the kaon potential—which is repulsive—shifts the v_2 of K^+ mesons to a more negative value, while the antikaon potential—which is attractive—moves the v_2 of K^- mesons towards less negative values. We note that the kaon-nuclear potential is necessary to reproduce the experimental data from the KaoS Collaboration, but antikaon medium effects do not help to explain the KaoS experimental data for the v_2 of K^- mesons.

Finally we show in Fig. 24 the azimuthal angular distribution of K^+ in semicentral Au+Au collisions at 1.5A GeV (upper plot) and in semicentral Ni+Ni collisions at 1.93A GeV (lower plot). Since the rapidity range is the same as in Fig. 22, the contributions from v_1 are small and the distributions are dominated by v_2. One can see that the v_2 of K^+ mesons is negative both in Au+Au and Ni+Ni collisions and turning on the kaon-nuclear potential enhances the negative flow, which is consistent with the results for v_2 in Fig. 22. We note that an increase of the kaon-nuclear potential [Eq. (40)] from +25 MeV at ρ_0 to a large value (e.g., +35 MeV) leads to some small increase of the anisotropy in the azimuthal angular distribution. However, the transverse momentum spectra of K^+ mesons become harder which is not supported by the experimental data. Though the v_2 of K^+ mesons—with the default kaon-nuclear potential of +25 MeV at ρ_0—is smaller than with larger repulsive potential, our results qualitatively agree with the experimental data from the KaoS Collaboration [91]. However, as seen from Fig. 24, the azimuthal angular distribution depends only very modestly on the inclusion of the medium effects for (anti)kaons.

E. Multiplicity dependence on A_{part} and on the EoS

The threshold kaon production in heavy-ion collisions is one of the sensitive probes for the nuclear equation-of-state [10,22,24]. In the present study we use a static Skyrme potential [92] parametrized by

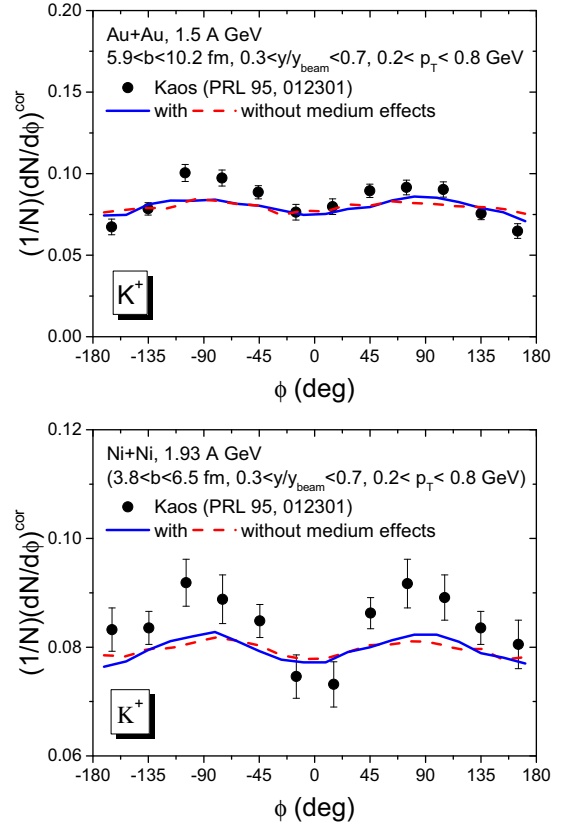$$U(\rho) = a\left(\frac{\rho}{\rho_0}\right) + b\left(\frac{\rho}{\rho_0}\right)^\gamma, \qquad (52)$$

FIG. 24. The azimuthal angular distributions of K^+ in semi-central Au+Au collisions at 1.5A GeV (upper) and in semi-central Ni+Ni collisions at 1.93A GeV (lower) in comparison to the experimental data from the KaoS Collaboration [91]. The solid lines show the calculations with medium effects, while the dashed lines display results without medium effects.

where $a = -153$ MeV, $b = 98.8$ MeV, $\gamma = 1.63$. The parameters a,b,γ are chosen to assure that the energy per nucleon has a minimum of $\frac{E}{A}(\rho_0) = -16$ MeV at ρ_0. The third condition to fix the parameters is the choice of the nuclear compressibility $\chi = \frac{1}{V}\frac{dV}{dP}$, where P is the pressure and V is the volume of the system. Usually its inverse quantity—the compression modulus K—is quoted [93], and is defined as

$$K = -V\frac{dP}{dV} = 9\rho^2 \frac{\partial^2 (E/A)}{\partial \rho^2}\bigg|_{\rho_0}. \qquad (53)$$

A large compression modulus K reflects that the nuclear matter can be hardly compressed, thus the equation-of-state is called a "hard" EoS. Oppositely, a small K stands for a "soft" EoS. The soft EoS enhances the production of kaons in heavy-ion collisions for two reasons: (i) it allows for the formation of dense nuclear matter where nucleons have more chances to collide and produce kaons; (ii) the nucleons loose less compression energy and the "saved" energy can be used for the production of kaons. Our set of parameters gives a compression modulus $K \simeq 300$ MeV at saturation density, which is in between the soft and hard equations of state, i.e., a "middle-soft" EoS. This "middle-soft" EoS provides an optimal description of the different observables at SIS

energies and, thus is used as "default" value in the PHSD for low energy heavy-ion collisions. In order to investigate the sensitivity of the K^+, K^- production on the EoS, we have changed the EoS in PHSD to a softer one with $K = 210$ MeV and to a harder one with $K = 380$ MeV. We found that the softening of the EoS leads to an increase of the K^+ and K^- yields by $\approx 13\%$ and $\approx 24\%$, respectively, in central Ni+Ni collisions at 1.93 GeV, while a harder EoS decreases them, respectively, by $\approx 14\%$ and $\approx 19\%$. We mention that also momentum-dependent Skyrme interactions have been successfully employed to study the in medium properties of kaon [21,24].

The stiffness of the nuclear equation of state affects also the dependence of kaon production on the centrality of heavy-ion collisions. The softer the equation-of-state is, the more kaons are produced in central collisions compared to semicentral and peripheral collisions [24]. The centrality dependence might be converted to the dependence on A_{part} being the number of participants. The multiplicity of (anti)kaons in heavy-ion collisions is proportional to $M \sim (A_{part})^\alpha$, where α is a fitting parameter. The deviation from a scaling with A_{part} ($\alpha = 1$) points towards "collective production effects": e.g., a formation of K^+ by scattering of resonances such as $\Delta N \rightarrow N \Lambda K^+$ collisions. The probability that a Δ interacts with nucleons and produces a kaon (before it disintegrates to a pion and nucleon) increases with baryon density, which is larger for the most central collisions. For pion production the deviation from the linear A_{part} dependence is not expected since, in spite of multiple Δ decay and regeneration by pion-nucleon scattering, the number of final pions is not much affected. Indeed, as found by the KaoS Collaboration [85], in the case of pion production, the experimental value α_π is compatible with unity $[\alpha_\pi(\text{Au}) = 0.96 \pm 0.05, \alpha_\pi(\text{Ni}) = 1.0 \pm 0.05]$, while for kaons $\alpha_K(\text{Au}) = 1.34 \pm 0.16$, i.e., the kaon multiplicity rises stronger than linear with A_{part}. A similar behavior has been observed for antikaons $[\alpha_{\bar{K}}(\text{Au}) = 1.22 \pm 0.27]$ despite the different production thresholds. This leads to constant ratio of K^-/K^+ versus centrality. We note that the PHSD reproduces the KaoS results on the pion value of α_π rather well.

Figure 25 shows the PHSD results (including the medium effects) for the multiplicities per mean number of participants A_{part} of K^+ (upper), K^- (middle), and $\Lambda + \Sigma^0$ (lower) in Au+Au collisions at 1.5A GeV in comparison to the KaoS data for K^+ taken from Ref. [85]. The solid red lines represent the PHSD results with the default EoS, the blue dashed line and green dotted show the results with a hard and soft EoS, respectively. One can see a strong sensitivity of the multiplicity of kaons and $\Lambda + \Sigma^0$ on the compression modulus of the EoS: the hard EoS leads to a strong reduction of the multiplicity in central collisions while the soft EoS to an enhancement of kaons and $\Lambda + \Sigma^0$. We note that we obtain the best description of the experimental data with the default "middle-soft" EoS in the PHSD.

The grey dot-dashed lines indicate a fit of the PHSD results (with default EoS) for the multiplicities as $M \sim (A_{part})^\alpha$: we find for kaons $\alpha_K^{\text{PHSD}}(\text{Au}) \simeq 1.34$, in agreement with the KaoS data. Moreover, for $\Lambda + \Sigma^0$ we find $\alpha_{\Lambda+\Sigma^0}^{\text{PHSD}}(\text{Au}) \simeq 1.32$, which is almost the same as for kaons. For the antikaons
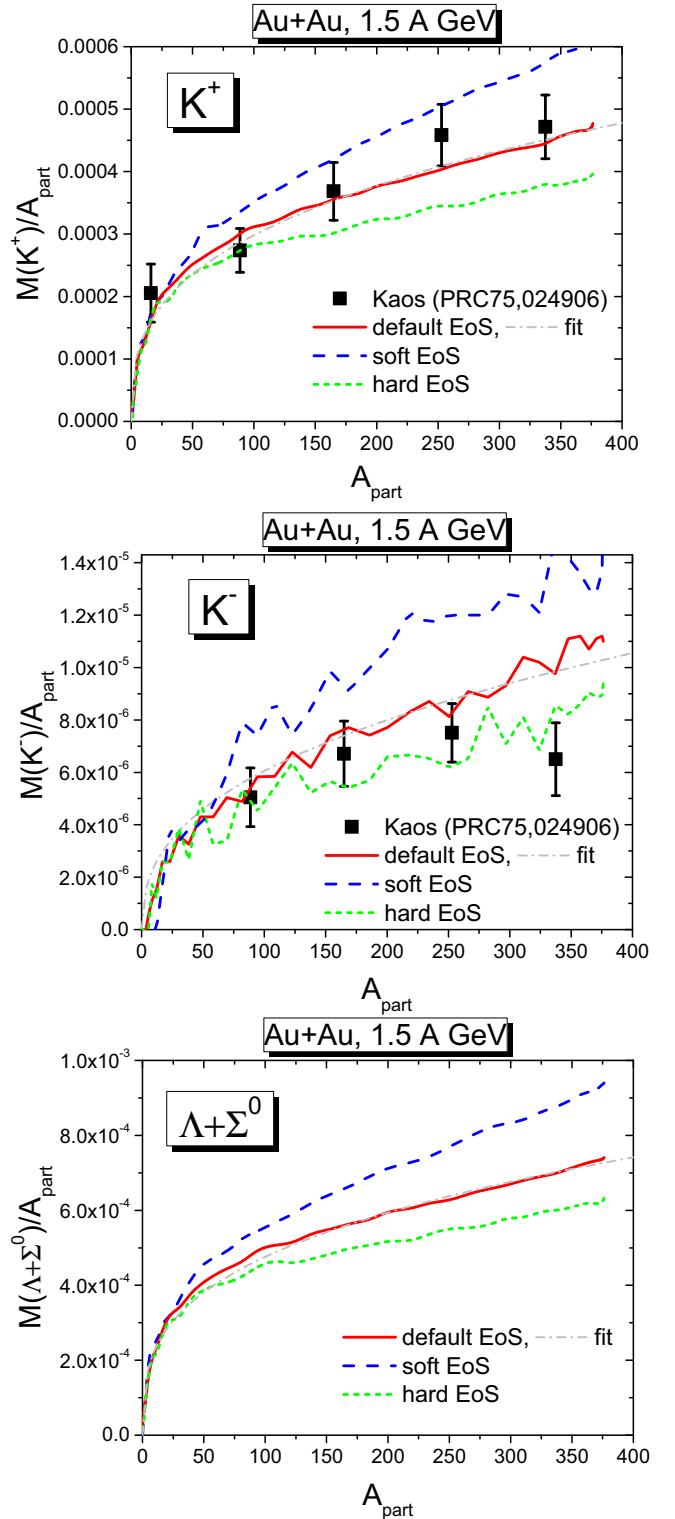

FIG. 25. Multiplicities per mean number of participants A_{part} of K^+ (upper), K^- (middle) and $\Lambda + \Sigma^0$ (lower) in Au+Au collisions at 1.5A GeV. The solid red lines correspond to the PHSD results (including in-medium effects) with default EoS, the blue dashed line and green dotted show the results with a hard and soft EoS, respectively. The grey dot-dashed lines indicate the fit of the PHSD results with the default EoS (see text). The solid squares show the KaoS data for K^+ taken from Ref. [85].
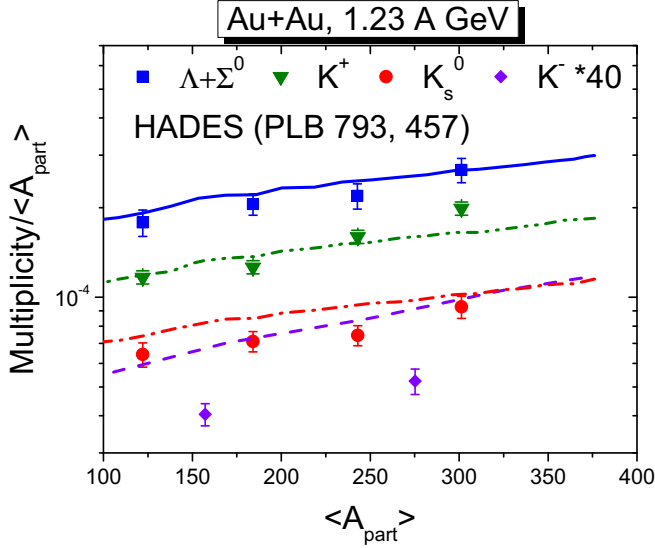
FIG. 26. The PHSD results for the A_{part} dependence of the multiplicity over averaged A_{part} of $\Lambda + \Sigma^0$ (blue solid line), K^+ (green dot-dot-dashed line), $K_s^0 = (K^0 + \bar{K}^0)/2$ (red dot-dashed line), and K^- (violet dashed line, multiplied by 40) in comparison to the experimental data from the HADES Collaboration [9].

$\alpha_K^{PHSD}(Au) \simeq 1.4$, which is a bit larger than for kaons, but still in the range of experimental error bars [85].

We stress that the change of the equation of state leads to a modification of the whole dynamics of the heavy-ion collisions at low energies, which is seen in the "bulk" observables such as proton and pion rapidity and p_T spectra, angular distributions, flow harmonics v_1, v_2, etc. The strange hadrons are reflecting these changes since their production mechanisms are tightly linked to the dynamics of nonstrange baryons and pions, especially at subthreshold energies considered in this study. Thus, in order to pin down a robust information on the nuclear EoS from low energy experimental data, one has to analyze of all observables—for strange and for nonstrange hadrons—simultaneously.

As follows from Fig. 25 the PHSD reproduces well the A_{part} dependence K^+ for Au+Au at 1.5A GeV. Now we step down in energy and come to subthreshold K^+ production in Au+Au collisions at 1.23A GeV. In Fig. 26 we show the PHSD results for the A_{part} dependence of the multiplicity over averaged A_{part} of $\Lambda + \Sigma^0$ (blue solid line), K^+ (green dot-dot-dashed line), $K_s^0 = (K^0 + \bar{K}^0)/2$ (red dot-dashed line), and K^- (violet dashed line, multiplied by 40) in comparison to the experimental data from the HADES Collaboration [9]. One can see that the $\Lambda + \Sigma^0$ and K^+ data are reasonable well described by PHSD. However, as expected, we see the same tension of the PHSD results for the K_s^0 and K^- with the HADES data as in Figs. 10 and 14: the K_S^0 data are overestimated by 20% and K^- data are overestimated by a factor of 2.

By fitting the experimental data with $M \simeq \langle A_{part} \rangle^\alpha$ the HADES Collaboration extracted $\alpha_{HADES} = 1.45 \pm 0.06$ for $K+$, K^-, K_s^0, and $\Lambda + \Sigma^0$ [9]. On the other hand in Ref. [9] the comparison of the HADES results to the model predic-

TABLE III. Comparison of the inclusive ratios of K^+ and K^0 mesons for Ru+Ru to Zr+Zr collisions at the kinetic energy 1.528A GeV in the PHSD versus the FOPI data [96].

Ratio	PHSD	FOPI
K_{Ru}^+/K_{Zr}^+	1.09	$1.06 \pm 0.07(stat.) \pm 0.09(syst.)$
K_{Ru}^0/K_{Zr}^0	0.96	$0.94 \pm 0.12(stat.) \pm 0.06(syst.)$
$\frac{(K^+/K^0)_{Ru}}{(K^+/K^0)_{Zr}}$	1.14	$1.13 \pm 0.16(stat.) \pm 0.12(syst.)$

tions [by HSD, IQMD (with and without medium effects), as well as by UrQMD] has been shown. A similar tension in multiplicity of K_s^0 between all three models and experimental data has been reported. We note that in Ref. [9] the comparison wasn done using the HSD model with G matrix from Ref. [19]. There the HSD results for K_s^0 and $\Lambda + \Sigma^0$ were fitted with $\alpha = 1.35 \pm 0.02$ (cf. Table II in Ref. [9]). Our new results for K_s^0 and $\Lambda + \Sigma^0$ are consistent with this finding, too. Moreover, the K^+ and K^- yields can be fitted with the same α, which is in agreement with KaoS results within error bars.

F. Isospin ratios of K^+ over K^0

Finally we check the isospin dependence of the K^+ to K^0 production. As advocated in Refs. [94,95] the inclusive K^+/K^0 ratio at subthreshold energies for kaon production is sensitive to the symmetry energy of the nucleon-nucleon potential and thus can be used to obtain experimental information on this issue. On the other hand, the isospin decomposition of strangeness production is defined to a large extend by hadronic inelastic and charge exchange reactions with baryons and mesons. Their cross sections are not well known experimentally and thus the transport calculations have to rely on phenomenological models. In this respect the experimental data on the K^+ to K^0 production in collisions of nuclei of different sizes provide an opportunity to access the production channels, too.

Experimentally the isospin dependence of K^+ and K^0 production at near subthreshold energies was investigated by the FOPI Collaboration in Ref. [96], which measured the ratios of K^+ to K^0 mesons for Ru+Ru to Zr+Zr collisions at the kinetic energy 1.528A GeV (i.e., at $\sqrt{s} = 2.527$ GeV, while the threshold for kaon production in pp collisions is $\sqrt{s_0} = 2.546$ GeV).

In Table III we show the comparison of the inclusive ratios of K^+ and K^0 mesons for Ru+Ru to Zr+Zr collisions, K_{Ru}^+/K_{Zr}^+, K_{Ru}^0/K_{Zr}^0, and $\frac{(K^+/K^0)_{Ru}}{(K^+/K^0)_{Zr}}$, at the kinetic energy 1.528A GeV from the PHSD versus the FOPI data [96]. One can see that the PHSD results are in a good agreement with the measured ratios as well as the model calculations from Ref. [94]. We note, however, that the symmetry energy is not implemented in the potential used in the PHSD version for this study. Thus, we attribute this agreement to the consequence of the isospin dependence of strangeness production and rescattering.

VIII. SUMMARY

In this study we have investigated strangeness production in heavy ion collisions at(sub)threshold energies between

1.0A and 2.0A GeV within the microscopic parton-hadron-string dynamics (PHSD 4.5) transport approach, extended for the incorporation of the in-medium effects for strangeness production in terms of the state-of-the-art coupled-channel G-matrix approach for the modification of antikaon properties in a dense and hot medium.

The PHSD is an off-shell transport approach based on the first-order gradient expansion (in phase-space representation) of the Kadanoff-Baym equations which allow for a propagation of particles with dynamical spectral functions, i.e., for a microscopic description of the strongly interacting system. It includes also the possibility to implement detailed balance on the level of $m \leftrightarrow n$ reactions (although its technical implementation is restricted to selected channels of interest due to the limitation in computational resources). For the present study we have incorporated the detailed balance on $2 \leftrightarrow 3$ level for the dominant channels for strangeness production/absorbtion by baryons ($B = N, \Delta$) and pions: $B + B \leftrightarrow N + Y + K$ and $B + \pi \leftrightarrow N + N + \bar{K}$, as well as the non-resonant reactions $N + N \leftrightarrow N + N + \pi$ and $\pi + N \leftrightarrow N + \pi + \pi$ to have a better control on pion dynamics.

The modification of the strangeness properties in the hot and dense medium, which is created in the heavy-ion collisions, has been incorporated in the PHSD in the following way:

The medium effects for antikaons are determined by a self-consistent coupled-channel G-matrix approach [56], based on a chiral Lagrangian, which provides the spectral function of antikaons as well as the scattering amplitudes (i.e., in-medium cross sections) as a function of baryon density, temperature, and the three-momentum of the antikaon with respect to the matter at rest. This novel G-matrix approach [56] incorporates the full self-consistency in s and p waves in the $\bar{K}N$ interaction at finite density and temperature based on a SU(3) chiral Lagrangian. It differs therefore from the previous work of Ref. [19], where a self-consistent unitary approach based on the Jülich meson-exchange model [38,39] was used.

We point out that the novel G-matrix approach provides a more shallow dependence of the real part of the complex antikaon self-energy Re Σ (and, respectively, $\bar{K}N$ potential) on baryon density than that from Refs. [38,39], which has been used in the past in the off-shell HSD [19] for antikaon dynamics at SIS energies.

Nuclear medium effects on the production and interactions of kaons are implemented by a repulsive kaon potential of $V_K = +25$ MeV (ρ/ρ_0).

We have studied the effects of the (anti)kaon medium modifications on different observables in heavy-ion collisions at SIS energies measured by the KaoS, FOPI, and HADES Collaborations. Our study confirms the sensitivity of antikaon observables to the details of the in-medium models: the in-medium effects on observables obtained with the novel G matrix are slightly less pronounced as compared to the previous G-matrix calculations, which provided a much stronger attraction of antikaons in nuclear matter.

Our findings can be summarized as follows:

(i) The kaon-nuclear potential increases the threshold energy for the kaon production in BB and mB reactions in a hot and dense medium. Consequently, the K^+, K^0 production in $A + A$ collisions is suppressed when accounting for the potential compared to the case without potential. We note that in $A + A$ collisions at (sub)threshold energies the kaons are dominantly produced by the reactions with Δ's (as $N + \Delta \rightarrow Y + K + N$) and mesons (as $\pi + N \rightarrow Y + K$). That enhances kaon production substantially relative to the production by $N + N$ reactions only. Moreover, production of kaons below the $N + N$ threshold is possible only in $A + A$ collisions due to the Fermi motion of nucleons and by secondary nucleon reactions with pions.

(ii) The self-consistent coupled-channel unitarized scheme based on a SU(3) chiral Lagrangian leads to a broadening of the $\bar{K}$ spectral function without drastic changes of the pole mass. Moreover, the strength of the attractive $\bar{K}N$ potential decreases with increasing three-momentum of $\bar{K}$ mesons in nuclear matter. The $\bar{K}$ production in $A + A$ collisions is enhanced by the broad spectral width (which increases with density) which leads to a reduction of the production threshold. The antikaons are dominantly produced by the secondary hyperon-meson reactions $Y + m \rightarrow B + \bar{K}$, which are delayed in time. Consequently, the baryon density at the antikaon production point is lower compared to that at the kaon production point, that reduces the in-medium effects.

(iii) The kaon-nuclear potential hardens the p_T spectra of K^+, K^0 mesons while the in-medium effects in terms of self-energies within the G-matrix approach soften the K^- spectra. These effects are stronger in larger systems such as Au+Au collisions, where a higher density is reached and therefore the density gradient (which is proportional to the force) is larger as compared to smaller systems like C+C collisions.

(iv) For kaons, both collisions with baryons and mesons as well as the repulsive interaction with the nuclear medium lead to an increase of the effective temperature T_{eff} of the p_T spectrum compared to that at the kaon production. For antikaons the hardening of the p_T spectra due to collisions and the softening due to the in-medium effects counterbalance partially.

(v) The repulsive kaon potential widens the rapidity distribution of K^+ mesons, while an attractive antikaon interaction shrinks that of K^- mesons. It is also visible in the enhancement of the polar angular distribution of K^+ mesons in forward and backward directions, although the effect of K^+ rescattering in the medium plays an even larger role than the KN potential, especially for heavy systems such as Au+Au. The polar angular distribution of K^- mesons stays rather flat due to the competition of two effects: the scattering pushes K^- mesons backward and forward similar to K^+; however, the antikaon potential attracts them to the middle zone of the colliding system; this push is stronger for

central collisions and heavy systems due to the larger density.

(vi) The collective flow coefficients for K^+ and K^- are strongly affected by the flow of nucleons, since (anti)kaons are produced by nucleon scattering and secondary interactions with nucleons. Considering only scattering and neglecting the kaon-nuclear potential, the directed flow v_1 of K^+ mesons follows that of nucleons such that the v_1 of K^+ mesons is positive at forward rapidity and negative at backward rapidity. However, the repulsive kaon potential pushes the K^+ mesons in the opposite direction to the nucleons and, as a result, the v_1 of K^+ mesons for low transverse momenta increases strongly and becomes positive, while the v_1 of K^+ mesons with large transverse momenta stays negative and finally changes only slightly.

The elliptic flow v_2 of K^+ and K^- mesons are also affected by the flow of nucleons. In noncentral heavy-ion collisions, the nucleons gain a negative elliptic flow due to the geometric shape of the medium and attractive Skyrme potential. The v_2 of the produced K^+ mesons is initially positive, following that of nucleons, and becomes negative due to the scattering and repulsive interactions with nucleons. This is also seen in the azimuthal angular distribution of kaons. On the other hand, the antikaon-nuclear potential acts in the opposite direction: while the v_2 of the initially produced antikaons is also positive (as for K^+) and becomes also negative due to the rescattering in the matter, the attractive antikaon potential pushes the v_2 towards less negative values such that the final v_2 of antikaons is close to zero in the present PHSD calculations.

(vii) Moreover, we have investigated the sensitivity of strangeness production to the nuclear equation of state. In line with the previous findings [10,22,24] we have observed an enhancement of (anti)kaon production by a softening of the EoS. However, we stress that solid conclusions on the EoS can be obtained only by considering a variety of observables (including the nonstrange hadrons) since the dynamics of strangeness is tightly bound to the dynamics of the "bulk" matter in heavy-ion collisions and the density of pions.

(viii) Finally, our study with the improved description for the modifications of the (anti)kaon properties in the hot and dense medium (within the novel *G*-matrix approach) as well as an improved general dynamics of the medium itself (within the PHSD) confirms the previous findings by different groups (summarized in the review [24]) on the observation of the visible medium effects in heavy-ion collisions at SIS energies.

ACKNOWLEDGMENTS

APPENDIX A: CROSS SECTIONS FOR (ANTI)KAON PRODUCTION

In this Appendix we collect the parametrizations of the cross sections for $K, \bar{K}$ production by *BB*, *mB*, and *mm* reactions in the vacuum used in the PHSD. The theoretical origin of these parametrizations as well as the comparison to the available experimental data have been discussed in the original publications (and the references therein) [16–19,23–25] and are not repeated here. The in-medium modifications of (anti)kaon production cross sections are explained in Sec. V.

1. $N + N \rightarrow N + Y + K$

The reaction cross sections for the channels $N + N \rightarrow N + Y + K$ can be approximated by [97],

$$\sigma_{pp \rightarrow p\Lambda K^+} = 0.732 \left(1 - \frac{s_{01}}{s}\right)^{1.8} \left(\frac{s_{01}}{s}\right)^{1.5} \text{[mb]},$$

$$\sigma_{pp \rightarrow p\Sigma^+ K^0} = 0.339 \left(1 - \frac{s_{02}}{s}\right)^{2.25} \left(\frac{s_{02}}{s}\right)^{1.35} \text{[mb]},$$

$$\sigma_{pp \rightarrow p\Sigma^0 K^+} = 0.275 \left(1 - \frac{s_{02}}{s}\right)^{1.98} \left(\frac{s_{02}}{s}\right) \text{[mb]}, \quad \text{(A1)}$$

where $\sqrt{s_{01}} = m_\Lambda + m_p + m_K$ and $\sqrt{s_{02}} = m_\Sigma + m_p + m_K$. For simplicity, an isospin-averaged cross section is introduced by multiplying with a factor of 1.5 the cross sections of Eq. (A1):

$$\sigma_{NN \rightarrow N\Lambda K} = \tfrac{3}{2}\sigma_{pp \rightarrow p\Lambda K^+},$$

$$\sigma_{NN \rightarrow N\Sigma K} = \tfrac{3}{2}(\sigma_{pp \rightarrow p\Sigma^+ K^0} + \sigma_{pp \rightarrow p\Sigma^0 K^+}). \quad \text{(A2)}$$

The different isospin channels are then evenly weighted, for example,

$$\sigma_{pn\to n\Lambda K^+} = \sigma_{pn\to p\Lambda K^0} = \frac{1}{2}\sigma_{NN\to N\Lambda K},$$

$$\sigma_{pn\to n\Sigma^0 K^+} = \sigma_{pn\to n\Sigma^+ K^0} = \sigma_{pn\to p\Sigma^- K^+}$$

$$= \sigma_{pn\to p\Sigma^0 K^0} = \frac{1}{4}\sigma_{NN\to N\Sigma K}. \quad (A3)$$

The Δ baryon is assumed to have the same cross section for strangeness production as a nucleon:

$$\sigma_{N\Delta\to N\Lambda K} = \sigma_{\Delta\Delta\to N\Lambda K} = \sigma_{NN\to N\Lambda K}, \quad (A4)$$

where the production thresholds are modified accordingly depending on Δ mass.

2. $N + N \to N + N + K + \bar{K}$

As the center-of-mass energy $\sqrt{s}$ increases, a strange meson pair can be produced in the channel $N + N \to N + N + K + \bar{K}$ with a cross section given by [98]

$$\sigma_{NN\to NNK\bar{K}} = 1.5\left(1 - \frac{s_0}{s}\right)^{3.17}\left(\frac{s_0}{s}\right)^{1.96} \text{ [mb]}, \quad (A5)$$

where $\sqrt{s_0} = 2m_N + m_K + m_{\bar{K}}$. We assume the same form of the cross section if the initial nucleon is replaced by a Δ baryons, while baryons in the final state are always n or p.

3. $m + N \to K + Y, K + \bar{K} + N$

The cross section for Λ production ($\pi N \to K\Lambda$) is given by [99]

$$\sigma_{\pi^- p\to\Lambda K^0} = \frac{0.007665(\sqrt{s} - \sqrt{s_o})^{0.1341}}{(\sqrt{s} - 1.72)^2 + 0.007826} \text{ [mb]}, \quad (A6)$$

where $\sqrt{s_0}$ is the threshold energy. Using isospin relations [99] we find

$$\sigma_{\pi^0 p\to\Lambda K^+} = \sigma_{\pi^0 n\to\Lambda K^0} = \frac{1}{2}\sigma_{\pi^- p\to\Lambda K^0}, \quad (A7)$$

$$\sigma_{\pi^+ n\to\Lambda K^+} = \sigma_{\pi^- p\to\Lambda K^0}. \quad (A8)$$

In heavy-ion collisions many baryons are in resonance states. The contribution of resonances to the Λ production through $\pi + \Delta$ scattering is included by substituting p by a Δ^+ and n by a Δ^0 and assuming

$$\sigma_{\pi^-\Delta^{++}\to\Lambda K^+} = \sigma_{\pi^+\Delta^-\to\Lambda K^0} = \sigma_{\pi^- p\to\Lambda K^0}. \quad (A9)$$

The cross sections for Σ baryon production ($\pi N \to K\Sigma$) are given by [100,101]

$$\sigma_{\pi^+ p\to\Sigma^+ K^+} = \frac{0.03591(\sqrt{s} - \sqrt{s_o})^{0.9541}}{(\sqrt{s} - 1.89)^2 + 0.01548}$$
$$+ \frac{0.1594(\sqrt{s} - \sqrt{s_o})^{0.01056}}{(\sqrt{s} - 3.0)^2 + 0.9412} \text{ [mb]}, \quad (A10)$$

$$\sigma_{\pi^- p\to\Sigma^- K^+} = \frac{0.009803(\sqrt{s} - \sqrt{s_o})^{0.6021}}{(\sqrt{s} - 1.742)^2 + 0.006583}$$
$$+ \frac{0.006521(\sqrt{s} - \sqrt{s_o})^{1.4728}}{(\sqrt{s} - 1.94)^2 + 0.006248} \text{ [mb]}, \quad (A11)$$

$$\sigma_{\pi^+ n\to\Sigma^0 K^+} = \frac{0.05014(\sqrt{s} - \sqrt{s_o})^{1.2878}}{(\sqrt{s} - 1.73)^2 + 0.006455} \text{ [mb]}, \quad (A12)$$

$$\sigma_{\pi^0 n\to\Sigma^- K^+} = \sigma_{\pi^+ n\to\Sigma^0 K^+}, \quad (A13)$$

$$\sigma_{\pi^0 p\to\Sigma^0 K^+} = \frac{0.003978(\sqrt{s} - \sqrt{s_o})^{0.5848}}{(\sqrt{s} - 1.74)^2 + 0.00667}$$
$$+ \frac{0.04709(\sqrt{s} - \sqrt{s_o})^{2.165}}{(\sqrt{s} - 1.905)^2 + 0.006358} \text{ [mb]}, \quad (A14)$$

and isospin symmetry is assumed. Consequently we find

$$\sigma_{\pi^- n\to\Sigma^0 K^0} = \sigma_{\pi^+ p\to\Sigma^+ K^+},$$

$$\sigma_{\pi^+ n\to\Sigma^+ K^0} = \sigma_{\pi^- p\to\Sigma^- K^+},$$

$$\sigma_{\pi^- p\to\Sigma^0 K^0} = \sigma_{\pi^0 p\to\Sigma^+ K^0} = \sigma_{\pi^+ n\to\Sigma^0 K^+},$$

$$\sigma_{\pi^0 n\to\Sigma^0 K^0} = \sigma_{\pi^0 p\to\Sigma^0 K^+}, \quad (A15)$$

As for the Λ production, an initial p can be substituted by a Δ^+ and an initial n by a Δ^0. Δ^{++} and Δ^- are excluded for Σ production.

If the collision energy $\sqrt{s}$ exceeds 1.7 GeV, the cross section for $\Sigma + K$ production in Eqs. (A10) to (A15) is modified to

$$\sigma_{\pi N\to\Sigma K}(\sqrt{s}) = A\sqrt{s} - \sigma_0 - \sigma_{\pi N\to\Lambda K} - \sigma_{\pi N\to NK\bar{K}} \text{ [mb]}, \quad (A16)$$

where $A = 1.0$ (mb/GeV) and

$$\sigma_0 = 1.7 \text{ mb} - \sigma_{\pi N\to\Sigma K}$$
$$- \sigma_{\pi N\to\Lambda K} - \sigma_{\pi N\to NK\bar{K}}|_{\sqrt{s}=1.7 \text{ GeV}}. \quad (A17)$$

This means that the total cross section for strangeness production in baryon+meson scattering is a linear function of $\sqrt{s}$ above 1.7 GeV and smoothly connected at $\sqrt{s} = 1.7$ GeV.

The cross section $\sigma_{\pi N\to NK\bar{K}}$ in Eq. (A16) is given by [98]

$$\sigma_{\pi^- p\to pK^0 K^-} = 1.121\left(1 - \frac{s_0}{s}\right)^{1.86}\left(\frac{s_{01}}{s}\right)^2 \text{ [mb]}, \quad (A18)$$

where $\sqrt{s_0} = m_N + m_K + m_{\bar{K}}$, and the other channels with various isospin combinations are related to σ_0 of Eq. (A18) as follows [98]:

$$2\sigma(\pi^- p \to pK^0 K^-) = 2\sigma(\pi^- n \to nK^0 K^-)$$
$$= 2\sigma(\pi^+ p \to pK^+\bar{K}^0) = 2\sigma(\pi^+ n \to nK^+\bar{K}^0)$$
$$= \sigma(\pi^+ n \to pK^+ K^-) = \sigma(\pi^+ n \to pK^0\bar{K}^0)$$
$$= \sigma(\pi^0 p \to nK^+\bar{K}^0) = 4\sigma(\pi^0 p \to pK^+ K^-)$$
$$= 4\sigma(\pi^0 p \to pK^0\bar{K}^0) = \sigma(\pi^0 n \to pK^0 K^-)$$
$$= 4\sigma(\pi^0 n \to nK^+ K^-) = 4\sigma(\pi^0 n \to pK^0\bar{K}^0)$$
$$= \sigma(\pi^- p \to nK^+ K^-) = \sigma(\pi^- p \to pK^0\bar{K}^0). \quad (A19)$$

Again an initial p can substituted by a Δ^+ and an initial n by a Δ^0 assuming the same form of the cross section, while in the final state only p or n are admitted.

The inverse reaction $K + Y \to \pi + N$ is realized by detailed balance and $N + K + \bar{K} \to N + \pi$ by using an equation similar to Eq. (B12), including a Δ baryon in the final

state. For example,

$$\sigma_{\Lambda K^+ \to \pi^+ \Delta^0} = 2\sigma_{\Lambda K^+ \to \pi^0 \Delta^+} = \sigma_{\Lambda K^+ \to \pi^- \Delta^{++}}$$

$$= \left(\frac{p_\Delta}{p_\Lambda}\right)^2 \sigma_{\pi^+ \Delta^0 \to \Lambda K^+} = \left(\frac{p_N}{p_\Lambda}\right)^2 \sigma_{\pi^+ n \to \Lambda K^+},$$
$$(A20)$$

where p_i is the three-momentum of particle i in the c.m. frame.

4. $\bar{K} + B \to \pi + Y$

The reactions $\bar{K} + N \to \pi + Y$ are modeled (also in the vacuum) according to the G matrix as indicated by Eqs. (6) and (7). However, the present coupled channels of G matrix do not incorporate reactions with baryonic resonances which are abundant at SIS energies. For such reactions [with $B = \Delta, N(1440), N(1535)$] we use the parametrizations presented below.

The cross section for $\bar{K}$ absorption by baryons is equal to the total cross section of $\bar{K}B$ scattering subtracted by the $\bar{K}N$ elastic scattering cross section[102]. The total cross section of $\bar{K}B$ scattering [102] is

$$\sigma_{\bar{K}+B \to \pi+Y}^{\text{tot}}$$
$$= 22.6 p_K^{-1.14} \text{ [mb]}, \quad p_K < 0.7 \text{ GeV}/c,$$
$$= 47.54 p_K^{-0.94} \text{ [mb]}, \quad 0.7 \text{ GeV}/c \leqslant p_K < 1.1 \text{ GeV}/c,$$
$$= 69.87 p_K^{-3.1} \text{ [mb]}, \quad 1.1 \text{ GeV}/c \leqslant p_K < 1.3 \text{ GeV}/c,$$
$$= 32.4 p_K^{-0.17} \text{ [mb]}, \quad 1.3 \text{ GeV}/c \leqslant p_K < 10 \text{ GeV}/c,$$
$$= 22 \text{ [mb]}, \quad 10 \text{ GeV}/c \leqslant p_K, \quad (A21)$$

while the $\bar{K}N$ elastic scattering cross section is

$$\sigma_{\bar{K}+B \to \pi+Y}^{\text{elast}}$$
$$= 10.58 p_K^{-0.98} \text{ [mb]}, \quad 0.03 \text{ GeV}/c \leqslant p_K < 0.7 \text{ GeV}/c,$$
$$= 23 p_K^{1.2} \text{ [mb]}, \quad 0.7 \text{ GeV}/c \leqslant p_K < 1 \text{ GeV}/c,$$
$$= 23 p_K^{-2.6} \text{ [mb]}, \quad 1 \text{ GeV}/c \leqslant p_K < 1.5 \text{ GeV}/c,$$
$$= 9.56 p_K^{-0.44} \text{ [mb]}, \quad 1.5 \text{ GeV}/c \leqslant p_K < 20 \text{ GeV}/c,$$
$$= 2.56 \text{ [mb]}, \quad 20 \text{ GeV}/c \leqslant p_K, \quad (A22)$$

where p_K is the momentum of the $\bar{K}$ in the B rest frame. The $\bar{K}$ absorption cross section is weighted by 0.3 for $Y = \Lambda$ and by 0.2 for $Y = \Sigma$.

5. Elastic and isospin-exchange scattering of kaons

Finally $K + N$ elastic cross section and the cross section for isospin exchange are parametrized in the units of mb as

$$\sigma_{\text{elastic}}^{K^+ p} = \sigma_{\text{elastic}}^{K^0 n}$$
$$= 12.3 + 1.88 p_K - 2.32 p_K^2 \quad (p_K < 2.3 \text{ GeV}/c),$$
$$= 5 \text{ [mb]} \quad (p_K > 2.3 \text{ GeV}/c). \quad (A23)$$

Here p_K is the three-momentum of a kaon (GeV/c) in center-of-mass frame,

$$\sigma_{\text{elastic}}^{K^+ n} = \sigma_{\text{elastic}}^{K^0 p}$$
$$= 10.51 p_K^{0.82} \quad (p_K < 0.6 \text{ GeV}/c),$$
$$= -18.93 + 76.68 p_K - 66.65 p_K^2 + 17.74 p_K^3$$
$$(0.6 < p_K < 1.5 \text{ GeV}/c),$$
$$= 6 \text{ [mb]} \quad (1.5 \text{ GeV}/c < p_K), \quad (A24)$$

and

$$\sigma^{K^+ n \leftrightarrow K^0 p} = 5.63 + 4.996 p_K - 4.519 p_K^2 (p_K < 1.5 \text{ GeV}/c),$$
$$= 6.502/p_K^{1.932} \quad (1.5 \text{ GeV}/c < p_K). \quad (A25)$$

The above cross sections are important for the generation of collective flows and isospin diffusion of K^+ and K^0 in heavy-ion collisions.

APPENDIX B: 3-TO-2 INTERACTIONS

The scattering cross section for 2-to-3 processes can be expressed as

$$\sigma_{2 \to 3} = \frac{1}{4 E_1 E_2 v_{\text{rel}}} \int \frac{d^3 p_1'}{(2\pi)^3 2 E_1'} \int \frac{d^3 p_2'}{(2\pi)^3 2 E_2'} \int \frac{d^3 p_3'}{(2\pi)^3 2 E_3'}$$
$$\times \overline{|M|}^2 (2\pi)^4 \delta^{(4)}(p_1 + p_2 - p_1' - p_2' - p_3'), \quad (B1)$$

where v_{rel} is the relative velocity of the incident particles and $\overline{|M|}^2$ is the transition amplitude squared averaged over initial states:

$$\overline{|M|}^2 = \frac{|M|^2}{D_1 D_2} \quad (B2)$$

with D_1, D_2 denoting the spin-flavor degeneracy of the initial two particle states. Assuming that the transition amplitude does not depend on scattering angle but only on the collision energy $\sqrt{s}$, the cross section can be rewritten as

$$\sigma_{2 \to 3} = \frac{1}{4 E_1 E_2 v_{\text{rel}}} \frac{|M|^2}{D_1 D_2} (PS)_3 = \frac{1}{4 p_1^{\text{c.m.}} \sqrt{s}} \frac{|M|^2}{D_1 D_2} (PS)_3,$$
$$(B3)$$

where $p_1^{\text{c.m.}} = |\vec{p}_1|$ in the c.m. frame and

$$(PS)_3 = \int \frac{d^3 p_1'}{(2\pi)^3 2 E_1'} \int \frac{d^3 p_2'}{(2\pi)^3 2 E_2'} \int \frac{d^3 p_3'}{(2\pi)^3 2 E_3'}$$
$$\times (2\pi)^4 \delta^{(4)}(p_1 + p_2 - p_1' - p_2' - p_3'). \quad (B4)$$

The three-body phase-space integral $(PS)_3$ is simplified in the c.m. frame of $p_2' + p_3'$ as follows:

$$(PS)_3 = \int \frac{d^3 p_1'}{(2\pi)^3 2 E_1'} \int \frac{d^3 p_2'}{(2\pi)^2 4 E_2' E_3'}$$
$$\times \delta(E_1 + E_2 - E_1' - E_2' - E_3')$$
$$= \frac{1}{16\pi^3 \sqrt{s}} \int_{m_2'+m_3'}^{\sqrt{s}-m_1'} dM_{23} p_1'^{\text{c.m.}} p_2^*, \quad (B5)$$

where $M_{23} = \sqrt{(p_2 + p_3)^2}$ and $p_1'^{c.m.} = |p_1'|$ in the c.m. frame of $p_1 + p_2$ and $p_2^* = |p_2'|$ in the c.m. frame of $p_2' + p_3'$, i.e.,

$$p_1'^{c.m.} = \frac{\sqrt{\{s - (m_1' + M_{23})^2\}\{s - (m_1' - M_{23})^2\}}}{2\sqrt{s}},$$

$$p_2^* = \frac{\sqrt{\{M_{23}^2 - (m_2' + m_3')^2\}\{M_{23}^2 - (m_2' - m_3')^2\}}}{2M_{23}}. \quad (B6)$$

A cross section for 3-to-2 processes cannot be defined but a Lorentz invariant interaction rate for 3-to-2 processes is given by [72,103,104]

$$\frac{\Delta N^{3\to 2}}{\Delta t \, \Delta V} = \frac{1}{D_1' D_2' D_3'} \int \frac{d^3 p_1}{(2\pi)^3 2E_1}$$

$$\times \int \frac{d^3 p_2}{(2\pi)^3 2E_2} \int \frac{d^3 p_1'}{(2\pi)^3 2E_1'} f_1(p_1')$$

$$\times \int \frac{d^3 p_2'}{(2\pi)^3 2E_2'} f_2(p_2') \int \frac{d^3 p_3'}{(2\pi)^3 2E_3'} f_3(p_3')$$

$$\times |M|^2 (2\pi)^4 \delta^{(4)}(p_1 + p_2 - p_1' - p_2' - p_3'), \quad (B7)$$

where $f_i(p_i')$ is a particle distribution function including its degeneracy factor D_i'. Keeping in mind that $|M|^2$ does not depend on the scattering angle in the c.m. frame of $p_1 + p_2$, the rate may be written as

$$\frac{\Delta N^{3\to 2}}{\Delta t \, \Delta V} = \frac{1}{D_1' D_2' D_3'} \frac{p_1^{c.m.}}{4\pi\sqrt{s}} |M|^2 \int \frac{d^3 p_1'}{(2\pi)^3 2E_1'} f_1(p_1')$$

$$\times \int \frac{d^3 p_2'}{(2\pi)^3 2E_2'} f_2(p_2') \int \frac{d^3 p_3'}{(2\pi)^3 2E_3'} f_3(p_3'). \quad (B8)$$

Expressing the distribution functions by [103]

$$f_i = (2\pi)^3 \frac{\Delta N_i}{\Delta p_i^3 \Delta V}, \quad (B9)$$

the interaction rate turns to

$$\frac{\Delta N^{3\to 2}}{\Delta t \, \Delta V} = \frac{1}{D_1' D_2' D_3'} \frac{p_1^{c.m.}}{4\pi\sqrt{s}} |M|^2 \frac{\Delta N_1' \Delta N_2' \Delta N_3'}{8E_1' E_2' E_3' (\Delta V)^3}. \quad (B10)$$

Now substituting $|M|^2$ from Eq. (B3) one obtains

$$\frac{\Delta N^{3\to 2}}{\Delta t} = \frac{D_1 D_2}{D_1' D_2' D_3'} \frac{(p_1^{c.m.})^2}{\pi (PS)_3} \sigma_{2\to 3} \frac{\Delta N_1' \Delta N_2' \Delta N_3'}{8E_1' E_2' E_3' (\Delta V)^2}, \quad (B11)$$

where Δt, ΔV, and ΔN correspond to the simulation time interval, volume of the grid cell, and particle number in the grid cell, respectively. We note that Eq. (B11) is equivalent to the expression in Ref. [73].

The transition probability for the transition $NYK \to N'N''$ in the volume ΔV during the time interval Δt is given by

$$P_{NYK \to N'N''} = \frac{D_{N'} D_{N''}}{D_N D_Y D_K} \frac{(p_{N''}^{c.m.})^2}{\pi (PS)_3} \sigma_{N'N'' \to NYK}$$

$$\times \frac{\Delta N_N \Delta N_Y \Delta N_K}{8E_N E_Y E_K (\Delta V)^2} \Delta t, \quad (B12)$$

with the three-body phase-space integral

$$(PS)_3 = \int \frac{d^3 p_N}{(2\pi)^3 2E_N} \int \frac{d^3 p_Y}{(2\pi)^3 2E_Y} \int \frac{d^3 p_K}{(2\pi)^3 2E_K}$$

$$\times (2\pi)^4 \delta^{(4)}(p_{N'} + p_{N''} - p_N - p_Y - p_K). \quad (B13)$$

The degeneracy factors need additional specification: for example, $(\Sigma^0 K^+ n)$, $(\Sigma^+ K^0 n)$, $(\Sigma^0 K^0 p)$, or $(\Sigma^- K^+ p)$ can produce $(p\, n)$, $(p\, \Delta^0)$, $(n\, \Delta^+)$, $(\Delta^+\, \Delta^-)$, or $(\Delta^{++}\, \Delta^-)$, and the ratio of the degeneracy factors in Eq. (B12) is 1/4, 1/2, and 1/2 for the final states of (NN), $(N\Delta)$, and $(\Delta\Delta)$, respectively, which are distinguished by $p_{N''}^{c.m.}$. As another example, $(\Lambda K^+ p)$ to $(p\, p)$ has an additional degeneracy factor of 1/2 because two protons in the final state are indistinguishable. The mass of the Δ baryon is randomly sampled from its spectral function, and if the total mass of the final states is above $\sqrt{s}$, the transition does not take place. This Monte Carlo sampling is effectively equivalent to the integral of the Δ spectral function over invariant mass.

APPENDIX C: CROSS SECTION FOR $\bar{K}$ PRODUCTION IN THE MEDIUM

The phase space for the scattering of on-shell particles is given by

$$\int \frac{d^3 p_3}{(2\pi)^3 2E_3} \frac{d^3 p_4}{(2\pi)^3 2E_4} (2\pi)^4 \delta^{(4)}(p_1 + p_2 - p_3 - p_4). \quad (C1)$$

The phase space for p_3 can be changed into a more explicitly covariant form,

$$\int \frac{d^3 p_3}{(2\pi)^3 2E_3} \to \int \frac{d^4 p_3}{(2\pi)^4} 2\pi \delta^+(p_3^2 - m_3^3), \quad (C2)$$

where $\delta^+(x - x_0)$ is nonzero only for positive x_0. Comparing the normalization condition of Eq. (28) and Eq. (C2), one can find that the spectral function $A(\omega, \mathbf{p}_3)$ corresponds to $2\pi\delta^+(p_3^2 - m_3^2)$ with the same normalization condition,

$$2 \int_0^\infty \frac{d\omega}{2\pi} \omega 2\pi \delta^+(p_3^2 - m_3^2) = \int_0^\infty d\omega 2\omega \delta^+(\omega^2 - E_3^2)$$

$$= \int_0^\infty d\omega \frac{\omega}{E_3} \delta(\omega - E_3) = 1, \quad (C3)$$

where $E = \sqrt{m_3^2 + p_3^2}$. Therefore, the covariant form of Eq. (C2) can be modified for off-shell particles into

$$\int \frac{d^3 p_3}{(2\pi)^3 2E_3} \to \int \frac{d^4 p_3}{(2\pi)^4} A(p_3^0, \mathbf{p}_3)$$

$$= \int \frac{dp_3^0}{2\pi} A(p_3^0, \mathbf{p}_3) \int \frac{d^3 p_3}{(2\pi)^3}$$

$$= \int_0^{(\sqrt{s}-m_4)^2} \frac{dm_3^2}{2\pi} A(m_3^2) \int \frac{d^3 p_3}{(2\pi)^3 2p_3^0}, \quad (C4)$$

where $m_3^2 = (p_3^0)^2 - \mathbf{p}_3^2$ and m_4 is the mass of the particle other than particle 3 in the final state. The cross section

turns into

$$\sigma(\sqrt{s}; M_3) \rightarrow \int_0^{(\sqrt{s}-m_4)^2} \frac{dm_3^2}{2\pi} A(m_3^2)\, \sigma(\sqrt{s}; m_3), \quad \text{(C5)}$$

where M_3 and m_3 are on-shell and off-shell masses, respectively. Applying the same assumption of Eq. (43) to Eq. (C5), the cross section for off-shell particle production reads

$$\int_0^{(\sqrt{s}-m_4)^2} \frac{dm_3^2}{2\pi} A(m_3^2)\, \sigma(\sqrt{s} - m_3 + M_3). \quad \text{(C6)}$$

The same spectral function can be applied to the decay of a ϕ or K^* meson. Assuming that the transition amplitude does not depend on the mass of the daughter particles, the decay width is calculated as

$$\Gamma \sim \frac{1}{M} \int_0^{(M-m_2)^2} \frac{dm_1^2}{2\pi} A(m_1^2) \int \frac{d^3 p_1}{(2\pi)^3 2E_1}$$

$$\times \int \frac{d^3 p_2}{(2\pi)^3 2E_2} (2\pi)^4 \delta^{(4)}(p - p_1 - p_2)$$

$$= \frac{1}{4\pi M^2} \int_0^{(M-m_2)^2} \frac{dm_1^2}{2\pi} A(m_1^2) p_1^{\text{c.m.}}(m_1^2), \quad \text{(C7)}$$

where M is the mass of the mother particle and $p_1^{\text{c.m.}}$ is the three-momentum of the off-shell particle in the c.m. frame. Therefore m_1—produced through the decay—has the mass differential distribution

$$\frac{dP(m_1^2)}{dm_1^2} = \frac{A(m_1^2) p_1^{\text{c.m.}}(m_1^2)}{8\pi^2 M^2 \Gamma} = A(m_1^2)$$

$$\times \frac{\sqrt{\{M^2 - (m_1 + m_2)^2\}\{M^2 - (m_1 - m_2)^3\}}}{(4\pi)^2 M^3 \Gamma}. \quad \text{(C8)}$$

The probability is proportional to $p_1^{\text{c.m.}}$ because the phase space increases with $p_1^{\text{c.m.}}$.

APPENDIX D: TIME-EVOLUTION OF THE OFF-SHELL PARTICLE MASS

As shown in Eq. (37) the energy of the off-shell particle is updated as

$$\frac{dE}{dt} = \frac{1}{2E}\left[\partial_t \operatorname{Re}\Sigma + \frac{M^2 - M_0^2}{\operatorname{Im}\Sigma}\partial_t \operatorname{Im}\Sigma\right], \quad \text{(D1)}$$

where C is neglected for simplicity. Since the partial derivatives are expressed in terms of the total derivatives as

$$\frac{\partial \operatorname{Re}\Sigma}{\partial t} = \frac{d\operatorname{Re}\Sigma}{dt} - \mathbf{v}\cdot\nabla\operatorname{Re}\Sigma, \quad \text{(D2)}$$

$$\frac{\partial \operatorname{Im}\Sigma}{\partial t} = \frac{d\Gamma}{dt} - \mathbf{v}\cdot\nabla\operatorname{Im}\Sigma, \quad \text{(D3)}$$

Equation (D1) turns into

$$\frac{dE}{dt} = \frac{1}{2E}\left\{\frac{d\operatorname{Re}\Sigma}{dt} + \frac{M^2 - M_0^2}{\operatorname{Im}\Sigma}\frac{d\operatorname{Im}\Sigma}{dt}\right\}$$

$$- \frac{\mathbf{v}}{2E}\cdot\left\{\nabla\operatorname{Re}\Sigma + \frac{M^2 - M_0^2}{\operatorname{Im}\Sigma}\nabla\operatorname{Im}\Sigma\right\}$$

$$= \frac{1}{2E}\left\{\frac{d\operatorname{Re}\Sigma}{dt} + \frac{M^2 - M_0^2}{\operatorname{Im}\Sigma}\frac{d\operatorname{Im}\Sigma}{dt}\right\} + \mathbf{v}\cdot\frac{d\mathbf{p}}{dt}, \quad \text{(D4)}$$

where Eq. (36) has been substituted in the second equation. Multiplying by $2E$ on both sides,

$$2E\frac{dE}{dt} - 2\mathbf{p}\cdot\frac{d\mathbf{p}}{dt} - \frac{d\operatorname{Re}\Sigma}{dt} = \frac{M^2 - M_0^2}{\operatorname{Im}\Sigma}\frac{d\operatorname{Im}\Sigma}{dt}, \quad \text{(D5)}$$

and using

$$2E\frac{dE}{dt} = \frac{dE^2}{dt}, \quad 2\mathbf{p}\cdot\frac{d\mathbf{p}}{dt} = \frac{d\mathbf{p}^2}{dt}, \quad \text{(D6)}$$

the left-hand side of Eq. (D5) is simplified to

$$\frac{d(E^2 - \mathbf{p}^2 - \operatorname{Re}\Sigma)}{dt} \equiv \frac{dM^2}{dt} = \frac{M^2 - M_0^2}{\operatorname{Im}\Sigma}\frac{d\operatorname{Im}\Sigma}{dt}, \quad \text{(D7)}$$

where $M^2 = E^2 - \mathbf{p}^2 - \operatorname{Re}\Sigma$, which is equivalent to Eq. (39).

[1] D. B. Kaplan and A. E. Nelson, Phys. Lett. B **175**, 57 (1986); **192**, 193 (1987).

[2] D. Best *et al.* (FOPI Collaboration), Nucl. Phys. A **625**, 307 (1997).

[3] F. Laue *et al.* (KaoS Collaboration), Phys. Rev. Lett. **82**, 1640 (1999).

[4] M. Menzel *et al.* (KaoS Collaboration), Phys. Lett. B **495**, 26 (2000).

[5] C. Sturm *et al.* (KaoS Collaboration), Phys. Rev. Lett. **86**, 39 (2001).

[6] A. Förster *et al.* (KaoS Collaboration), J. Phys. G **28**, 2011 (2002).

[7] V. Zinyuk *et al.* (FOPI Collaboration), Phys. Rev. C **90**, 025210 (2014).

[8] G. Agakishiev *et al.* (HADES Collaboration), Eur. Phys. J. A **47**, 21 (2011).

[9] J. Adamczewski-Musch *et al.* (HADES Collaboration), Phys. Lett. B **793**, 457 (2019).

[10] J. Aichelin and C. M. Ko, Phys. Rev. Lett. **55**, 2661 (1985).

[11] X. S. Fang, C. M. Ko, G. Q. Li, and Y. M. Zheng, Phys. Rev. C **49**, R608 (1994); G. Q. Li, C. M. Ko, and X. S. Fang, Phys. Lett. B **329**, 149 (1994).

[12] C. M. Ko and G. Q. Li, J. Phys. G **22**, 1673 (1996); C. M. Ko, V. Koch, and G. Q. Li, Annu. Rev. Nucl. Part. Sci. **47**, 505 (1997).

[13] G. Q. Li, C.-H. Lee, and G. E. Brown, Nucl. Phys. A **625**, 372 (1997).

[14] C. M. Ko, J. Phys. G **27**, 327 (2001).

[15] S. Pal, C. M. Ko, and Z.-W. Lin, Phys. Rev. C **64**, 042201(R) (2001).

[16] W. Cassing, E. L. Bratkovskaya, U. Mosel, S. Teis, and A. Sibirtsev, Nucl. Phys. A **614**, 415 (1997).

[17] E. L. Bratkovskaya, W. Cassing, and U. Mosel, Nucl. Phys. A **622**, 593 (1997).

[18] W. Cassing and E. L. Bratkovskaya, Phys. Rep. **308**, 65 (1999).

[19] W. Cassing, L. Tolós, E. L. Bratkovskaya, and A. Ramos, Nucl. Phys. A **727**, 59 (2003).

[20] J. Schaffner-Bielich, V. Koch, and M. Effenberger, Nucl. Phys. A **669**, 153 (2000).

[21] C. Hartnack, H. Oeschler, and J. Aichelin, Phys. Rev. Lett. **90**, 102302 (2003); C. Hartnack and J. Aichelin, J. Phys. G **28**, 1649 (2002).

[22] C. Fuchs, Amand Faessler, E. Zabrodin, and Y.-M. Zheng, Phys. Rev. Lett. **86**, 1974 (2001); C. Fuchs, Prog. Part. Nucl. Phys. **56**, 1 (2006).

[23] A. Mishra, E. L. Bratkovskaya, J. Schaffner-Bielich, S. Schramm, and H. Stöcker, Phys. Rev. C **70**, 044904 (2004).

[24] C. Hartnack, H. Oeschler, Y. Leifels, E. L. Bratkovskaya, and J. Aichelin, Phys. Rep. **510**, 119 (2012).

[25] E. E. Kolomeitsev, C. Hartnack, H. W. Barz, M. Bleicher, E. Bratkovskaya, W. Cassing, L. W. Chen, P. Danielewicz, C. Fuch, T. Gaitanos, C. M. Ko, A. Larionov, M. Reiter, G. Wolf, and J. Aichelin, J. Phys. G **31**, S741 (2005).

[26] G. Q. Li, C. M. Ko, and B. A. Li, Phys. Rev. Lett. **74**, 235 (1995); Nucl. Phys. A **594**, 460 (1995); G. Q. Li and C. M. Ko, Phys. Rev. C **54**, 1897 (1996); G. Q. Li, C. M. Ko, and G. E. Brown, Phys. Lett. B **381**, 17 (1996).

[27] G. E. Brown and M. Rho, Phys. Rev. Lett. **66**, 2720 (1991).

[28] E. Friedman, A. Gal, and C. J. Batty, Nucl. Phys. A **579**, 518 (1994).

[29] A. Gal, Nucl. Phys. A **691**, 268 (2001).

[30] E. Friedman and A. Gal, Phys. Rep. **452**, 89 (2007).

[31] M. Lutz, Phys. Lett. B **426**, 12 (1998).

[32] T. Waas, N. Kaiser, and W. Weise, Phys. Lett. B **365**, 12 (1996).

[33] T. Waas, N. Kaiser, and W. Weise, Phys. Lett. B **379**, 34 (1996).

[34] M. Lutz and E. E. Kolomeitsev, Nucl. Phys. A **700**, 193 (2002).

[35] M. Lutz and C. L. Korpa, Nucl. Phys. A **700**, 309 (2002).

[36] A. Ramos and E. Oset, Nucl. Phys. A **671**, 481 (2000).

[37] A. Mishra, K. Balazs, D. Zschiesche, S. Schramm, H. Stöcker, and W. Greiner, Phys. Rev. C **69**, 024903 (2004).

[38] L. Tolos, A. Ramos, A. Polls, and T. T. S. Kuo, Nucl. Phys. A **690**, 547 (2001).

[39] L. Tolos, A. Ramos, and A. Polls, Phys. Rev. C **65**, 054907 (2002).

[40] V. Koch, Phys. Lett. B **337**, 7 (1994).

[41] L. Tolos and L. Fabbietti, Prog. Part. Nucl. Phys. **112**, 103770 (2020).

[42] W. Cassing and S. Juchem, Nucl. Phys. A **672**, 417 (2000).

[43] W. Cassing and S. Juchem, Nucl. Phys. A **665**, 377 (2000).

[44] W. Cassing, Eur. Phys. J. Spec. Top. **168**, 3 (2009).

[45] W. Ehehalt and W. Cassing, Nucl. Phys. A **602**, 449 (1996).

[46] W. Cassing and E. L. Bratkovskaya, Phys. Rev. C **78**, 034919 (2008).

[47] W. Cassing and E. L. Bratkovskaya, Nucl. Phys. A **831**, 215 (2009)

[48] E. L. Bratkovskaya, W. Cassing, V. P. Konchakovski, and O. Linnyk, Nucl. Phys. A **856**, 162 (2011)

[49] O. Linnyk, E. L. Bratkovskaya, and W. Cassing, Prog. Part. Nucl. Phys. **87**, 50 (2016)

[50] P. Moreau, O. Soloveva, L. Oliva, T. Song, W. Cassing, and E. Bratkovskaya, Phys. Rev. C **100**, 014911 (2019).

[51] A. Peshier and W. Cassing, Phys. Rev. Lett. **94**, 172301 (2005).

[52] W. Cassing, Nucl. Phys. A **795**, 70 (2007).

[53] W. Cassing, Nucl. Phys. A **791**, 365 (2007).

[54] L. Tolos, A. Ramos, and E. Oset, Phys. Rev. C **74**, 015203 (2006).

[55] L. Tolos, D. Cabrera, and A. Ramos, Phys. Rev. C **78**, 045205 (2008).

[56] D. Cabrera, L. Tolos, J. Aichelin, and E. Bratkovskaya, Phys. Rev. C **90**, 055207 (2014).

[57] S. A. Bass, M. Belkacem, M. Bleicher et al., Prog. Part. Nucl. Phys. **41**, 255 (1998).

[58] V. Steinberg, J. Staudenmaier, D. Oliinychenko, F. Li, Ö. Erkiner and H. Elfner, Phys. Rev. C **99**, 064908 (2019).

[59] E. Oset and A. Ramos, Nucl. Phys. A **635**, 99 (1998).

[60] E. Oset and A. Ramos, Nucl. Phys. A **679**, 616 (2001).

[61] D. Jido, E. Oset, and A. Ramos, Phys. Rev. C **66**, 055203 (2002).

[62] J. A. Oller and U. G. Meissner, Phys. Lett. B **500**, 263 (2001).

[63] *Total Cross-Sections for Reactions of High Energy Particles: (Including Elastic, Topological, Inclusive and Exclusive Reactions)*, edited by H. Schopper, Landolt-Börnstein, New Series, Vol. I/12 (Springer-Verlag, Berlin, 1988).

[64] B. Nilsson-Almqvist and E. Stenlund, Comput. Phys. Commun. **43**, 387 (1987); B. Andersson, G. Gustafson, and H. Pi, Z. Phys. C **57**, 485 (1993).

[65] T. Sjostrand, S. Mrenna, and P. Z. Skands, J. High Energy Phys. 05 (2006) 026.

[66] V. Kireyeu, I. Grishmanovskii, V. Kolesnikov, V. Voronyuk, and E. Bratkovskaya, Eur. Phys. J. A **56**, 223 (2020).

[67] W. Cassing, A. Palmese, P. Moreau, and E. L. Bratkovskaya, Phys. Rev. C **93**, 014902 (2016).

[68] A. Palmese, W. Cassing, E. Seifert, T. Steinert, P. Moreau, and E. L. Bratkovskaya, Phys. Rev. C **94**, 044912 (2016).

[69] J. S. Schwinger, Phys. Rev. **82**, 664 (1951).

[70] S. Borsanyi et al., Phys. Lett B **730**, 99 (2014); Phys. Rev. D **92**, 014505 (2015).

[71] V. Ozvenchuk, O. Linnyk, M. I. Gorenstein, E. L. Bratkovskaya, and W. Cassing, Phys. Rev. C **87**, 024901 (2013).

[72] W. Cassing, Nucl. Phys. A **700**, 618 (2002).

[73] E. Seifert and W. Cassing, Phys. Rev. C **97**, 024913 (2018).

[74] E. L. Bratkovskaya and W. Cassing, Nucl. Phys. A **807**, 214 (2008).

[75] A. Ilner, D. Cabrera, C. Markert, and E. Bratkovskaya, Phys. Rev. C **95**, 014903 (2017); A. Ilner, J. Blair, D. Cabrera, C. Markert, and E. Bratkovskaya, *ibid.* **99**, 024914 (2019).

[76] H. W. Barz and H. Iwe, Phys. Lett. B **153**, 217 (1985).

[77] S. Protopopescu, M. Alston-Garnjost, A. Barbaro-Galtieri, S. M. Flatte, J. Friedman, T. Lasinski, G. Lynch, M. Rabin, and F. Solmitz, Phys. Rev. D **7**, 1279 (1973).

[78] M. Tanabashi et al. (Particle Data Group), Phys. Rev. D **98**, 030001 (2018).

[79] E. L. Bratkovskaya, W. Cassing, C. Greiner, M. Effenberger, U. Mosel, and A. Sibirtsev, Nucl. Phys. A **675**, 661 (2000).

[80] J. Cleymans and H. Satz, Z. Phys. C **57**, 135 (1993).

[81] N. Bastid et al. (FOPI Colllaboration), Phys. Rev. C **76**, 024906 (2007).

[82] J. Adamczewski-Musch et al. (HADES Collaboration), Phys. Lett. B **778**, 403 (2018).

[83] G. Agakishiev et al. (HADES Collaboration), Phys. Rev. C **80**, 025209 (2009).

[84] G. Agakishiev, A. Balanda, B. Bannier, R. Bassini, D. Belver, A. V. Belyaev, A. Blanco, M. Bohmer, J. L. Boyard, P. Cabanelas *et al.*, Phys. Rev. C **82**, 044907 (2010).

[85] A. Forster *et al.* (KaoS Collaboration), Phys. Rev. C **75**, 024906 (2007).

[86] H. Joos, Phys. Lett. B **24**, 103 (1967).

[87] A. Feijoo, V. Magas, and A. Ramos, Phys. Rev. C **99**, 035211 (2019).

[88] J. L. Ritman *et al.* (FOPI Collaboration), Z. Phys. A **352**, 355 (1995).

[89] P. Crochet *et al.* (FOPI Collaboration), Phys. Lett. B **486**, 6 (2000).

[90] M. Ploskon (KaoS Collaboration), Nucl. Phys. A **749**, 170 (2005).

[91] F. Uhlig *et al.* (KaoS Collaboration), Phys. Rev. Lett. **95**, 012301 (2005).

[92] T. H. R. Skyrme, Nucl. Phys. **9**, 615 (1958–1959).

[93] T. Song and C. M. Ko, Phys. Rev. C **91**, 014901 (2015).

[94] G. Ferini, T. Gaitanos, M. Colonna, M. Di Toro, and H. H. Wolter, Phys. Rev. Lett. **97**, 202301 (2006); M. Di Toro *et al.*, Nucl. Phys. A **782**, 267 (2007).

[95] B. A. Li, L. W. Chen, and C. M. Ko, Phys. Rep. **464**, 113 (2008).

[96] X. Lopez *et al.* (FOPI Collaboration), Phys. Rev. C **75**, 011901 (2007).

[97] A. Sibirtsev, Phys. Lett. B **359**, 29 (1995).

[98] A. Sibirtsev, W. Cassing, and C. Ko, Z. Phys. A **358**, 101 (1997).

[99] S. Huang, K. Tsushima, A. Faessler, E. Lehmann and R. K. Puri, arXiv:nucl-th/9412011.

[100] K. Tsushima, S. Huang, and A. Faessler, Phys. Lett. B **337**, 245 (1994).

[101] K. Tsushima, S. Huang, and A. Faessler, J. Phys. G **21**, 33 (1995).

[102] S. V. Efremov and E. Y. Paryev, Z. Phys. A **348**, 217 (1994).

[103] Z. Xu and C. Greiner, Phys. Rev. C **71**, 064901 (2005).

[104] T. Song, K. C. Han, and C. M. Ko, Phys. Rev. C **85**, 054905 (2012).